Multi-Modality Correspondence to Enhance Arrhythmogenic Atrial Substrate Identification

Guiding Persistent Atrial Fibrillation Ablation Therapy

Zur Erlangung des akademischen Grades eines

DOKTORS DER INGENIEURWISSENSCHAFTEN (Dr.-Ing.)

von der KIT-Fakultät für

Elektrotechnik und Informationstechnik

des Karlsruher Instituts für Technologie (KIT)

genehmigte

DISSERTATION

von

Deborah Nairn, M.Sc.

geb. in Irvine, Schottland

Tag der mündlichen Prüfung:	14.04.2022
Referent:	Prof. Dr. rer. nat. Olaf Dössel
Korreferent:	PD. Dr.-Ing. Axel Loewe
Korreferent:	PD. Dr. med. Amir Jadidi

This document - excluding the cover, pictures, tables and graphs - is licensed under the Creative Commons Attribution-NonCommercial-NoDerivs 4.0 International License (CC BY-NC-ND 4.0): https://creativecommons.org/licenses/by-nc-nd/4.0/

Abstract

Atrial fibrillation (AF) is one of the leading health challenges posing a significant burden not only to patients but also to the health care systems. While pulmonary vein isolation (PVI) is an effective therapy for paroxysmal AF patients, the success rate drops for patients with persistent AF. This is thought to be due to patients exhibiting atrial cardiomyopathy (ACM), specifically structural remodelling in the atria occurring during the progression of AF. Therefore, persistent AF patients exhibit additional pathological substrate in the atria, which maintains the arrhythmia. Unfortunately, the current approaches performing PVI plus additionally targeting the pathological substrate are still sub-optimal, with only 50-70% of patients having long-term freedom from AF after catheter ablation. Hence, the optimal ablation strategy remains an open question demanding further research to identify promising ablation targets.

Two approaches that have gained attention over the recent years are electro-anatomical mapping specifically targeting low voltage areas and areas showing contrast in late gadolinium-enhanced magnetic resonance imaging (LGE-MRI). However, both are hindered by the lack of consensus regarding a precise method to identify the pathological substrate. Identification via low voltage mapping is limited due to a lack of understanding of the impact of catheter characteristics that influence the voltage aside from the pathological substrate. Additionally, voltage mapping can be performed during sinus rhythm (SR) or AF. Mapping in the latter case is beneficial as it reduces the need for potentially multiple cardioversions. However, there is no precise statistical evaluation for the cut-off values applied to determine low voltage areas. The advantage of using LGE-MRI instead is that it is a less invasive diagnostic method. However, the spatial resolution of LGE-MRI is limited. Moreover, the degree of accordance between MRI and voltage mapping to detect fibrosis remains disputed.

The overall goal of this thesis is to compare mapping modalities to address the fore-mentioned limitations. Therefore, providing more robust and accurate methods to identify pathological substrate areas known for the maintenance of atrial fibrillation.

In the first project, 28 persistent AF patients undergoing electro-anatomical mapping were studied. Statistical analysis was then applied, comparing each patient's bipolar and unipolar voltage maps. Specifically, the extent of agreement between methods was identified, finding the optimal unipolar thresholds to locate pathological substrate as determined by the bipolar voltage map. Additionally, the impact of the inter-electrode distances and regional discrepancies on the comparability was explored. For the second part of the project, simulations modelling electrodes of different sizes on a 2D patch and a lasso catheter in a 3D left atrial geometry were performed. This work identified that while the catheter characteristics influence the bipolar voltage values, they do not play a significant role in altering the location of the low voltage areas. The identified unipolar thresholds, which relate the bipolar and unipolar map, can help determine the extent of pathological substrate in an area. Additionally, it was found that larger electrodes deliver smaller voltages, providing techniques to compare results across studies and centres.

In the second project, a patient cohort where patients underwent electro-anatomical mapping while in SR and AF was used. The two rhythms could then be compared in each patient, and AF global and regional thresholds relating the rhythms could be identified. Additionally, the effects of inducing AF in patients could be explored and the benefits of different voltage calculation methods analysed. Low voltage thresholds that can better relate mapping in AF with SR were proposed. It was identified that using the regional thresholds proposed in this work could help prevent a false representation of the extent of pathological substrate within an area. Furthermore, using the maximum voltage value in a signal will lead to higher concordance between methods and using a variability measure (sample entropy) can help identify complex propagation patterns distorting the signals in AF.

Finally, the last project studied 36 patients who underwent both LGE-MRI and electro-anatomical mapping. Using this cohort, the concordance between different LGE-MRI mapping modalities and voltage and conduction velocity mapping could be investigated. Additionally, a new LGE-MRI analysis method could be developed to improve the agreement between the modalities. Spatial histograms showing typical low voltage and slow conduction regions were created in this work to help clinicians identify important regions to map during a procedure. Moreover, important discrepancies were found between methods, specifically on the posterior wall, which needs further investigation. Lastly, a new LGE-MRI thresholding method was developed, which could be used to identify patients with ACM. Therefore, providing a non-invasive approach which can help to determine whether additional mapping is needed in patients besides performing PVI.

The work presented in this thesis provides the clinical community with a deeper understanding of how the different methods to identify pathological substrate compare. Additionally, providing techniques to relate the methods, account for variability between centres and potentially reduce procedure times. Moreover, it was identified that perhaps one-size-fits-all ablation strategies is limited. Thus, this thesis supports the implementation of more personalised ablation approaches.

Zusammenfassung

Vorhofflimmern ist eines der häufigsten Gesundheitsprobleme und stellt nicht nur für Patienten, sondern auch für die Gesundheitssysteme eine erhebliche Belastung dar. Während die Pulmonalvenenisolation eine wirksame Therapie für paroxysmale Patienten mit Vorhofflimmern darstellt, sinkt die Erfolgsquote bei Patienten mit persistierendem Vorhofflimmern. Man nimmt an, dass dies auf strukturelle Veränderungen in den Vorhöfen zurückzuführen ist, die während des Fortschreitens des Vorhofflimmerns auftreten. Daher weisen Patienten mit persistierendem Vorhofflimmern ein zusätzliches pathologisches Substrat in den Vorhöfen auf, das die Arrhythmie aufrechterhält. Leider sind die derzeitigen Ansätze, bei denen Pulmonalvenenisolation und zusätzlich das pathologische Substrat angegangen werden, immer noch suboptimal, denn nur 50-70% der Patienten sind nach der Katheterablation dauerhaft frei von Vorhofflimmern. Daher bleibt die optimale Ablationsstrategie eine offene Frage, die weitere Forschung erfordert, um vielversprechende Ablationsziele zu identifizieren.

Zwei Ansätze, die in den letzten Jahren an Aufmerksamkeit gewonnen haben, sind die elektroanatomische Kartierung, die speziell auf Bereiche mit niedriger Spannung abzielt, und die Gadolinium-verstärkte Magnetresonanztomographie (LGE-MRI). Beide werden jedoch dadurch behindert, dass es keinen Konsens über eine präzise Methode zur Identifizierung des pathologischen Substrats gibt. Die eindeutige Identifizierung mittels Low Voltage Mapping wird erschwert, da die Auswirkungen von Kathetereigenschaften, die die Spannung neben dem pathologischen Substrat beeinflussen, nicht bekannt sind. Außerdem kann das Spannungsmapping während des Sinusrhythmus oder des Vorhofflimmerns durchgeführt werden. Im letzteren Fall ist das Mapping von Vorteil, da es den Bedarf an potenziell mehrfachen Kardioversionen reduziert. Es gibt jedoch keine genaue statistische Auswertung der Grenzwerte, die zur Bestimmung von Bereichen mit niedriger Spannung angewendet werden sollten. Der Vorteil der LGE-MRI ist, dass es sich um eine weniger invasive Diagnosemethode handelt. Allerdings ist die räumliche Auflösung der LGE-MRI begrenzt. Darüber hinaus ist der Grad der Übereinstimmung zwischen MRI und Spannungsmapping zum Nachweis von Fibrose umstritten.

Diese Arbeit ist in drei Projekte unterteilt, deren übergeordnetes Ziel es ist, die Kartierungsmodalitäten zu vergleichen, um die oben genannten Einschränkungen zu beseitigen. Dadurch sollen robustere und genauere Methoden zur Identifizierung pathologischer Substratbereiche bereitgestellt werden, die für die Aufrechterhaltung von Vorhofflimmern bekannt sind.

Im ersten Projekt wurden 28 Patienten mit persistierendem Vorhofflimmern untersucht, die sich einer elektro-anatomischen Kartierung unterzogen. Anschließend wurden die

bipolaren und unipolaren Spannungskarten der einzelnen Patienten statistisch verglichen. Insbesondere wurde das Ausmaß der Übereinstimmung zwischen den Methoden ermittelt, um die optimalen unipolaren Schwellenwerte für die Lokalisierung des pathologischen Substrats zu finden, wie sie durch die bipolare Spannungskarte bestimmt wurden. Darüber hinaus wurde untersucht, wie sich die Abstände zwischen den Elektroden und anatomisch regionale Unterschiede auf die Vergleichbarkeit auswirken. Im zweiten Teil des Projekts wurden Simulationen durchgeführt, bei denen Elektroden unterschiedlicher Größe auf einem 2D-Patch und ein Lasso-Katheter in einer 3D-Geometrie des linken Vorhofs modelliert wurden. Dabei stellte sich heraus, dass die Kathetereigenschaften zwar die bipolaren Spannungswerte beeinflussen, aber keine wesentliche Rolle bei der Veränderung der Lage der "Low Voltage"-Bereiche spielen. Anhand der ermittelten unipolaren Schwellenwerte, die die bipolare und unipolare Karte miteinander in Beziehung setzen, lässt sich das Ausmaß des pathologischen Substrats in einem Bereich bestimmen. Darüber hinaus wurde festgestellt, dass größere Elektroden geringere Spannungen liefern, was den Vergleich der Ergebnisse verschiedener Studien und Zentren ermöglicht.

Im zweiten Projekt wurde eine Patientenkohorte verwendet, bei der Patienten mit SR und Vorhofflimmern elektro-anatomisch kartiert wurden. Die beiden Rhythmen konnten dann bei jedem Patienten verglichen werden, und es konnten globale und regionale Schwellenwerte für die Spannung in Bezug auf die Rhythmen ermittelt werden. Darüber hinaus konnten die Auswirkungen der Induktion von Vorhofflimmern bei Patienten untersucht und die Vorteile verschiedener Methoden zur Spannungsberechnung analysiert werden. Es wurden Schwellenwerte für die Spannung vorgeschlagen, die das Mapping bei Vorhofflimmern mit SR besser in Beziehung setzen können. Es wurde festgestellt, dass die Verwendung der in dieser Arbeit vorgeschlagenen regionalen Schwellenwerte dazu beitragen könnte, eine falsche Darstellung des Ausmaßes des pathologischen Substrats in einem Gebiet zu vermeiden. Darüber hinaus führt die Verwendung des maximalen Spannungswerts in einem Signal zu einer höheren Konkordanz zwischen den Methoden, und die Verwendung eines Variabilitätsmaßes (Entropie) kann helfen, komplexe Ausbreitungsmuster zu erkennen, die die Signale bei Vorhofflimmern verzerren.

Das letzte Projekt schließlich untersuchte 36 Patienten, bei denen sowohl LGE-MRI als auch elektro-anatomisches Mapping durchgeführt wurde. Anhand dieser Kohorte konnte die Übereinstimmung zwischen verschiedenen LGE-MRI-Kartierungsmodalitäten und der Spannungs- und Leitungsgeschwindigkeitskartierung untersucht werden. Darüber hinaus konnte eine neue LGE-MRI-Methode zur Verbesserung der Übereinstimmung zwischen den Modalitäten entwickelt werden. In dieser Arbeit wurden räumliche Histogramme erstellt, die typische Regionen mit niedriger Spannung und langsamer Leitung zeigen, um Klinikärzten zu helfen, wichtige Regionen zu identifizieren, die während eines Eingriffs erfasst und abgebildet werden müssen. Darüber hinaus wurden erhebliche Diskrepanzen zwischen den Methoden festgestellt, insbesondere an der Hinterwand, was weitere Untersuchungen erfordert. Schließlich wurde eine neue LGE-MRI-Schwellenwertmethode entwickelt, die zur Identifizierung von Patienten mit atrialer Kardiomyopathie eingesetzt werden könnte.

Damit kann auf nicht-invasive Weise festgestellt werden, ob bei Patienten neben der PVI ein zusätzliches Mapping erforderlich ist.

Die in dieser Arbeit vorgestellten Ergebnisse vermittelten der klinischen Gemeinschaft ein tieferes Verständnis dafür, wie die verschiedenen Methoden zur Identifizierung von pathologischem Substrat miteinander verglichen werden können. Darüber hinaus werden Techniken zur Verfügung gestellt, um die Methoden miteinander in Beziehung zu setzen, die Variabilität zwischen den Kliniken zu berücksichtigen und die Verfahrensdauer potenziell zu verkürzen. Die Übereinstimmung zwischen den Kartierungsmodalitäten war von Patient zu Patient unterschiedlich, was darauf hindeutet, dass es nicht nur eine einzige Ablationsstrategie für alle gibt. Daher unterstützt diese Arbeit die Umsetzung von stärker personalisierten Ablationsansätzen.

Acknowledgments

I am so grateful for the chance to work over the last years in the Institute of Biomedical Engineering (IBT) at the Karlsruhe Institute of Technology (KIT). The whole team has made this time so special for me with such an open and collaborative environment.

Firstly, I would like to thank Prof. Olaf Dössel for the opportunity to work here. You set up the workplace to be such a friendly, open environment filled with discussion and enthusiasm for the field and for that, I am truly grateful. Additionally, I would like to thank Dr.-Ing. Axel Loewe for spending a lot of his time discussing my work, encouraging me, and keeping me on the right path. Additionally, I am very grateful to all the collaboration partners at Bad Krozingen. I especially have to thank Dr. med. Amir Jadidi, for spending countless hours with me discussing and working on all the projects and for your ideas and suggestions. I additionally wish to thank the German Research Foundation (DFG) for the financial support.

All my colleagues also deserve a big thank you for the collaboration, fun and laughs over the last years. Specifically, thanks to my office mate Yilun Su for the countless hours of fun, discussion and ranting to help each other get through the Ph.D. To Claudia Nagel, Dr. Jorge Sánchez, Tobias Gerach and Dr. Laura Unger, I always knew where I could go if I had questions, I am forever grateful for your help. To Dr. Ekaterina Kovacheva, Dr. Luca Azzolin, Cristian Barrios and Patricia Martinez for always being there for a chat, a break, or a bit of fun. To Carmen Martinez, Dr. Tiago Paggi de Almeida and Dr. Giorgio Luongo, for the countless times you have been there for me over the last years.

To all my friends in Scotland (Claire, Jemma, Hannah, Katie, Niamh, Catriona and Eilidh) who have supported me from a distance and made every visit back home special. Finally, to my family (Mum, Dad, Catherine, Keith, Fiona, Duncan, Andrew and Caroline) for the unconditional support and love throughout my life.

Contents

Abbreviations

Ca^+	calcium
K^+	potassium
Na^+	sodium
2D	two dimensional
3D	three dimensional
ACM	atrial cardiomyopathy
AF	atrial fibrillation
AP	action potential
AUC	area under the curve
CS	coronary sinus
CV	conduction velocity
EAM	electro-anatomical mapping
ECG	electrocardiogram
EGM	electrogram
FMM	fast marching method
FN	false negatives
FP	false positives
ICP	iterative closest point
LA	left atrium
LAA	left atrial appendage
LAT	local activation time
LGE-MRI	late gadolinium-enhanced magnetic resonance imaging
LIPV	left inferior pulmonary vein
LSPV	left superior pulmonary vein
LV	left ventricle
LVS	low voltage substrate
MV	mitral valve
NLEO	non-linear energy operator
p2p	peak-to-peak
PCA	Principal Component Analysis
PV	pulmonary vein
PVI	pulmonary vein isolation
RA	right atrium

RIPV	right inferior pulmonary vein
ROC	receiver operating characteristic
RSPV	right superior pulmonary vein
RV	right ventricle
SN	sinus node
SR	sinus rhythm
TN	true negatives
TP	true positives
WCT	Wilson’s central terminal

Chapter 1

Introduction

1.1 Motivation

Atrial fibrillation (AF) is the most common human arrhythmia affecting over 43.6 million people worldwide [1, 2] with a lifetime risk of development of 25% in people over the age of 40 [3]. In 2019, it was estimated that over 11 million people in Europe have AF and the annual healthcare costs of AF is 660 million euros in Germany [4, 5]. AF is associated with increased risk of ischemic stroke (2.4-fold), heart failure (5.0-fold) and cardiovascular mortality (2.0-fold) [6]. Development of AF in humans is related to advanced age, preexisting cardiovascular risk factors (eg. hypertension, overweight, sleep apnea syndrome) and preexisting cardiovascular diseases (eg. arteriosclerotic disease, heart failure, valvular or structural heart disease) [7].

One treatment option to terminate the arrhythmia is to perform pulmonary vein isolation (PVI) [8]. In patients with paroxysmal AF, PVI yields satisfactory success rates (75-90%) [9, 10]. However, in persistent AF patients, this success rate can drop to 30-50% [11, 12]. This is likely due to the patients exhibiting atrial cardiomyopathy (ACM) with additional pathological substrate in the body of the atria, which has been identified as the likely cause for AF [12–16].

Additionally targeting these pathological substrate areas can increase the success rate to 50-70% [17–19]. The root causes for this disappointing performance could be a lack of robust and accurate methods to localise the fibrotic substrate and thus the ablation targets. Overcoming these limits will enable an accurate differentiation between healthy and arrhythmogenic atrial substrate both prior to and during the catheter ablation procedure for AF.

Pathological AF sources with rapid, continuous or repeated rotational activity are frequently localised within fibrotic atrial regions displaying low bipolar electrical voltages $<0.5\,\mathrm{mV}$ during sinus rhythm (SR) [17, 20–22]. However, various characteristics of the catheter, for example, the angle of the catheter to the wavefront or the distance between electrodes and the electrode size, can affect the bipolar voltage values [23–25]. Therefore, it is important to identify to what extent the catheter characteristics play a role in bipolar voltage mapping and potentially reduce the method's success rate due to false interpretation of the signals. Further studies confirmed that the pathological substrate could also be identified when performing bipolar voltage mapping during AF [18, 19]. However, the identification of atrial regions with increased fibrosis has revealed significant differences in localisation of low voltage substrate (LVS) and their extent if patients are mapped during normal SR vs. AF [26].

A further modality for detecting atrial fibrosis is the localisation of late Gadolinium-enhanced (LGE) areas in magnetic resonance imaging (MRI). The technique has the advantage of being less invasive than electro-anatomical mapping and can improve the planning of the AF ablation procedure [27] by indicating regions of interest for the physician and providing information to decide on the optimal procedure option [28]. However, recent findings revealed a poor correlation between areas with high LGE-MRI intensities that were acquired during ongoing persistent AF and low voltage areas during AF [29, 30]. Ongoing clinical studies suggest that acquisition of LGE-MRI should be performed during regular SR in order to improve the spatial accuracy of atrial imaging by MRI [31, 32]. Fibrotic tissue can additionally affect the conduction velocity, as seen by recent computational studies [33]. Atrial fibrosis detection using LGE-MRI in SR may be a valuable tool that needs to be further validated with invasive voltage mapping. In particular, a multimodal substrate assessment combining LGE-MRI and electro-anatomical mapping could prove beneficial to pinpoint the arrhythmogenic tissue.

1.2 Objectives of the Thesis

The aim of this thesis is to compare and improve techniques that can accurately and robustly identify pathological substrate areas involved in the maintenance of atrial fibrillation, as well as allow for a more multi-center agreement of the location of fibrotic regions. To achieve this goal, the work was split into three projects.

The aims of the first project are to:

- Evaluate the impact of the catheters characteristic's on identifying low voltage substrate.
- Present optimal thresholds to relate unipolar and bipolar voltage mapping.
- Propose methods to compensate for different commercially available catheter characteristics.

The second project aims at:

- Assessing the relationship between bipolar voltage mapping during SR and AF.
- Provide corresponding voltage threshold for mapping in both rhythms.
- Investigating the impact of inducing atrial fibrillation on signals in AF.
- Present a technique to robustly calculate the voltage when mapping is performed during AF.

Finally, the last project will cover the following aspects:

- ○ Investigate the correspondence between the substrate mapping modalities: LGE-MRI vs. electro-anatomical voltage and conduction velocity mapping.
- ○ Establish a statistical atlas of the spatial distribution of low voltage and slow conduction areas in AF patients to compare with LGE-MRI on a population level.
- ○ Develop an new LGE-MRI method to identify patients with ACM .

By achieving these objectives, the clinical community will be provided with a clear, comparable, and unequivocal method to identify pathological substrate and patients with ACM. This will foster comparability between studies and centres, leveraging the full potential of low voltage guided ablation.

1.3 Structure of the Thesis

This thesis is structured as a combination of published and submitted papers in various high-impact peer-reviewed journals and conferences, along with additional sections of student theses that complement the work. Therefore, this work presents relevant and vital contributions to the scientific community aiding the detection of pathological substrate that maintains AF.

Chapters two and three present the medical and mathematical fundamentals required for this work.

- ○ **Chapter two:** a brief introduction about the human heart, its anatomy, physiology, and electrophysiology is given. Atrial fibrillation will then be introduced and state-of-the-art methods to treat the arrhythmia will be discussed.
- ○ **Chapter three:** provides an insight into state-of-the-art techniques for computational modelling of cardiac electrophysiology. This will be followed by an overview of signal processing methods, machine learning techniques and statistical measures used in this thesis.

Chapters 4, 5 and 6 present the three main projects of this work. Each chapter is structured similarly, first providing the motivation, a brief overview of the work and how different manuscripts or sections are related. Then any related articles or additional sections are included.

- ○ **Chapter four:** encompasses all projects (one published journal paper, an extract from a student thesis and a conference paper) related to investigating the influence of catheter characteristics on bipolar and unipolar voltage mapping.
- ○ **Chapter five:** comprises of studies (one submitted journal manuscript/ pre-print paper, a conference paper and an extract from a student thesis) that analyse the differences in the localisation of low voltage areas when mapping in different rhythms (SR vs. AF).

- **Chapter six:** contains one submitted journal manuscript/ pre-print paper exploring multiple modalities in their detection of pathological substrate and patients with ACM.

Chapter seven: summarises the main finding from all projects presented in this thesis, relating them to the objective set. Additionally, an overview of how this work impacts the clinical community is given.

Chapter eight: gives details of follow-up projects that could be performed in the future to further advance our understanding of AF and how to prevent recurrence of the arrhythmia.

Appendix: contains the supplementary material from each paper.

During the P.hD., I have published one journal paper, seven conference contributions as first author and two additional journal manuscript are under review. As a co-author, four journal papers and two conference contributions were published and two additional journal manuscript are under review. Furthermore, I won the Clinical Needs Translation Award for my conference contribution at the Computing in Cardiology (CinC) conference, a joint award provided by the European Society of Cardiology (ESC) and CinC. I supervised four student projects that formed parts of the work presented in this thesis. A list of publications and supervised theses can be found in the final section of this thesis.

Chapter 2

Medical Fundamentals

This chapter describes the medical fundamentals that are important for this thesis. First, there is a brief introduction to the anatomy and physiology of the heart. Then the electrophysiology will be summarised. Finally, the cardiac arrhythmia atrial fibrillation will be introduced along with the current clinical applications to treat the arrhythmia.

2.1 Anatomy and Physiology of the Heart

The human heart is a hollow muscular organ, approximately the size of a closed fist and located slightly left of the sternum. It is a vital organ for sustaining life as it pumps oxygen and nutrient-rich blood around the body. It is estimated that the heart beats 100,000 times per day, pumping 6-7.5 thousand litres of blood through the body every day [34].

The heart is divided into two halves, the left and right, each comprised of an atrium and a ventricle, as shown in figure 2.1. The two halves are separated by an inner wall (the septum), which prevents blood from mixing between the two sides. The oxygen-depleted blood flows into the right atrium (RA) from the body through two large veins (the inferior and superior vena cavae). The atrium then contracts and the blood flows into the right ventricle (RV) through the tricuspid valve. The valve opens to allow the blood to travel through to the next chamber and once the ventricle is full, it closes to stop the backflow of blood. The ventricles will then contract and the blood travels to the lungs through the pulmonary valve and pulmonary artery. The blood will then be oxygenated in the lungs before it is carried through the pulmonary veins (PVs) and returned to the left atrium (LA). As the LA contracts the blood flows to the left ventricle (LV) through the mitral valve (MV). The ventricles then contract, pushing the oxygen-enriched blood through the aortic valve into the aorta for distribution throughout the body [35].

The heart wall is divided into: the epicardium, the myocardium and the endocardium. The epicardium is the outer layer and the endocardium is the inner layer of the heart. The myocardium is the thickest layer containing cardiac muscle fibres, which allow the heart to contract. Since the ventricles need more power to force the blood out of the heart chambers, the ventricular myocardium is thicker than the atrial myocardium [36].

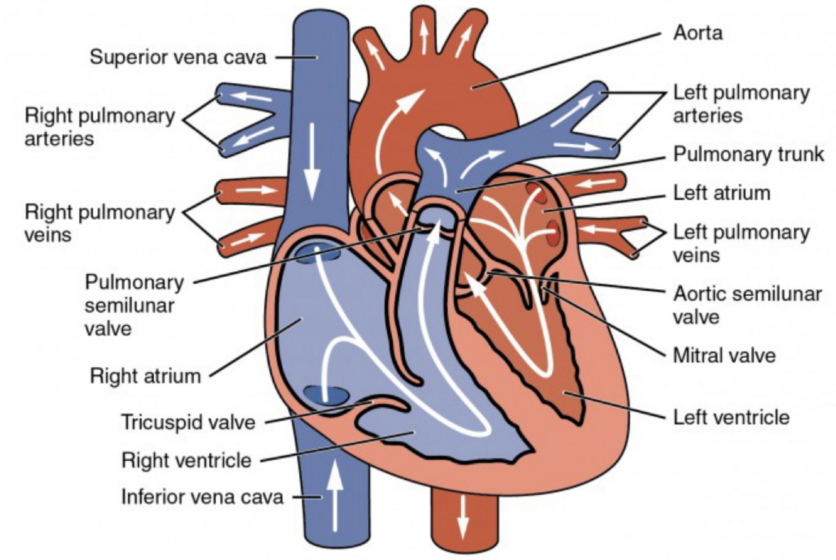

Figure 2.1: Anatomy of the human heart. The blue sections indicate the de-oxygenated blood and red the oxygenated blood. The white lines show the direction of the blood flow. Adapted from [34] and licensed under Creative Commons Attribution-Share Alike 3.0 Unported.

2.1.1 Atrial Anatomy

The RA is larger and thinner than the left, with a cylindrical shape. It can be divided into two parts: the smooth part situated between the inferior and superior vena cava and the body, consisting of the septum and the right atrial appendage and the rough part consisting of the posterior wall [37]. On the posterior wall is a collection of smaller veins that merge into the coronary sinus (CS). The CS is very important in electrophysiological studies as a catheter is often placed there to provide a stable reference.

The LA can be classified into 11 anatomical regions, as seen in figure 2.2 [38]. There are four PV which carry the oxygenated blood from both lungs into the LA. The veins are as follows: the right superior (RSPV) and right inferior (RIPV), the left superior (LSPV) and the left inferior (LIPV). In addition, there is the MV which is a valve with two flaps, lying between the LA and LV, allowing blood to pass between the two chambers. The six additional regions relate to the left atrial wall: the roof, septum, anterior wall, posterior wall, lateral wall, and inferior wall (otherwise known as the floor). Additionally, in the muscle wall, there is a small, ear-shaped sac at the top left chamber of the heart called the left atrial appendage (LAA).

The internal aspect of the LA's wall is smooth, but the thickness of the muscle is not uniform. The average thickness across the wall is around $2.10 \pm 0.60 mm$. The posterior wall $(1.86 \pm 0.4 mm)$ and septum $(1.92 \pm 0.3 mm)$ are thinner than the anterior wall $(2.34 \pm 0.72 mm)$, roof $(2.17 \pm 0.59 mm)$ and lateral wall $(2.08 \pm 0.43 mm)$ [35].

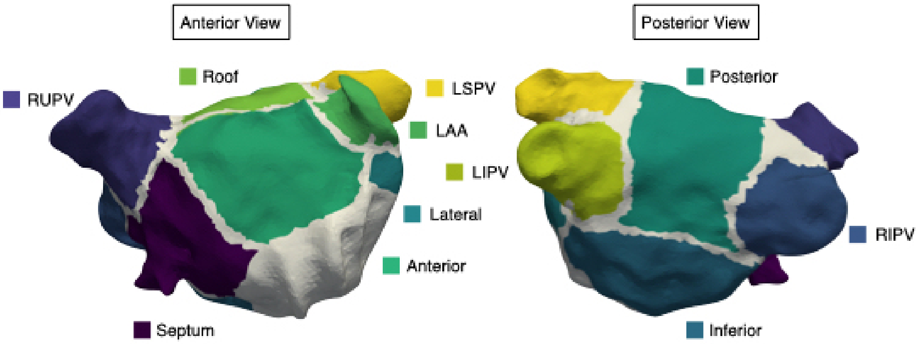

Figure 2.2: Anatomical regions of the left atria.

2.2 Electrophysiology of the Heart

The heart consists of specialised muscle cells called cardiac myocytes. Electrical impulses known as action potentials (APs) initiate the contraction of these cells. A small group of myocytes, otherwise known as pacemaker cells, cause electrical impulses to start. The primary pacemaker of the heart is the sinus node (SN). The SN cells fire around 80 APs per minute, causing APs to spread throughout the myocytes of the atria. Since gap junctions connect the myocytes, the neighboring cells have electrical coupling. Figure 2.3 shows the stages of the AP for the contractile myocardium. When the cardiomyocytes are not being electrically stimulated, they have a resting potential of -90 mV (label 4 in figure 2.3). This means that the cell's interior is negatively charged relative to the outside. When a neighbouring cell is depolarised, lots of sodium (Na^+) and calcium (Ca^+) ions leak through the gap junctions, causing the membrane voltage of the cell to increase. Once the threshold of -70 mV is exceeded, fast sodium channels open, causing Na^+ ions to flow into the cell and the voltage to quickly rise. This is the depolarising phase (labelled as 0 in figure 2.3). The Na^+ channels begin to gradually close after -40 mV. However, there is an overshoot of 20 mV. The potassium (K^+) channels open and cause K^+ ions to flow out of the cell leading to a slight repolarisation of the cell membrane (label 1 in figure 2.3). The potential then remains around 0 mV, known as the plateau phase, for around 200 ms during which time Ca^+ channels open and Ca^+ ions flow inwards (label 2 in figure 2.3). The length of this phase can differ depending on the heart rate and the location of the cell. As the Ca^+ channels slowly close, the K^+ outflux predominates and the membrane voltage returns to its resting value of -90 mV, this is the repolarisation phase (label 3 in figure 2.3). The Na^+/K^+ pump then restores the ionic balance across the membrane. During the repolarisation phase, a small stimulation can lead to depolarisation. In contrast, during the depolarisation and plateau phase, the cell is in the absolute refractory period, meaning that no additional stimulus can trigger a new activation regardless of the intensity [34].

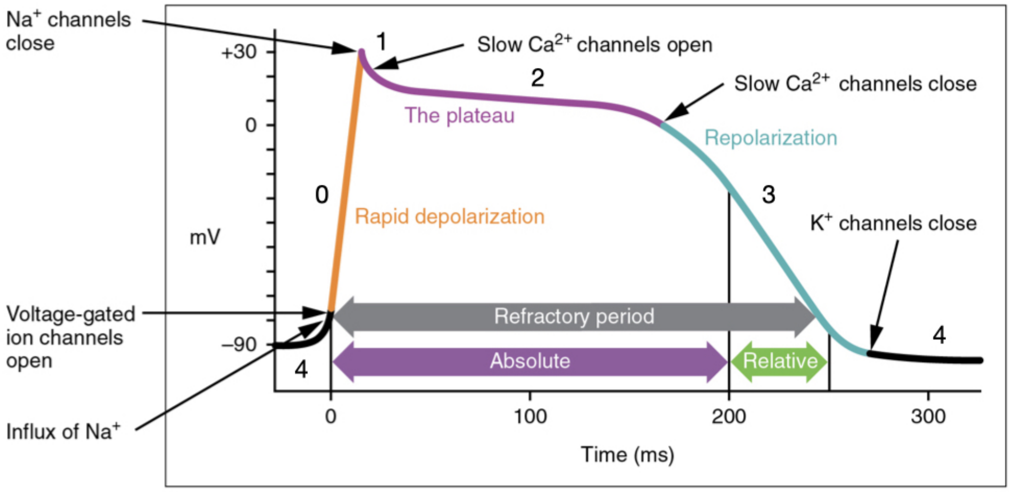

Figure 2.3: Cardiac action potential. Adapted from [34], and licensed under the Creative Commons Attribution-Share 4.0 International License.

2.2.1 Electrocardiograms

The electrocardiogram (ECG) is an efficient and non-invasive tool that measures the electrical conduction system of the heart. The electrical activity going through the heart is measured via external electrodes placed on the skin. Typically, a 12-lead ECG is used, which includes ten electrodes, with V1-V6 located at the chest and the other four placed on the limbs. Therefore, the overall picture of the heart's electrical potential is measured from different angles over a period of time, providing different perspectives of the events occurring in the heart [34].

The electrodes can detect the heart's pattern of depolarizing and repolarizing during each heartbeat. This can be viewed on an ECG as a sequence of waves, as seen in Figure 2.4. During each heartbeat, an electrical stimulus originating from the sinus node (SN), located in the RA, spreads across both atria. The SN generates an electrical stimulus regularly, typically 60 to 100 times per minute in rest, depending on a person's age, health and fitness. This electrical pulse, represented by the P-wave, causes the atria to contract. The electrical signal then passes from the atria to the ventricles via the atrioventricular node (AV). The signal slows down as it passes the node, allowing the ventricles to fill with blood. This can be seen on the ECG as the area after the P-wave and before the Q-wave. The impulse then travels down into the Bundle of His and the Purkinje fibers, spreading throughout the ventricles and causing them to contract (the QRS-complex). Atrial repolarization also occurs during this time but is not seen due to the large ventricular depolarization. The ventricles recover to their normal electrical state following the ST segment, which is shown by the T-wave.

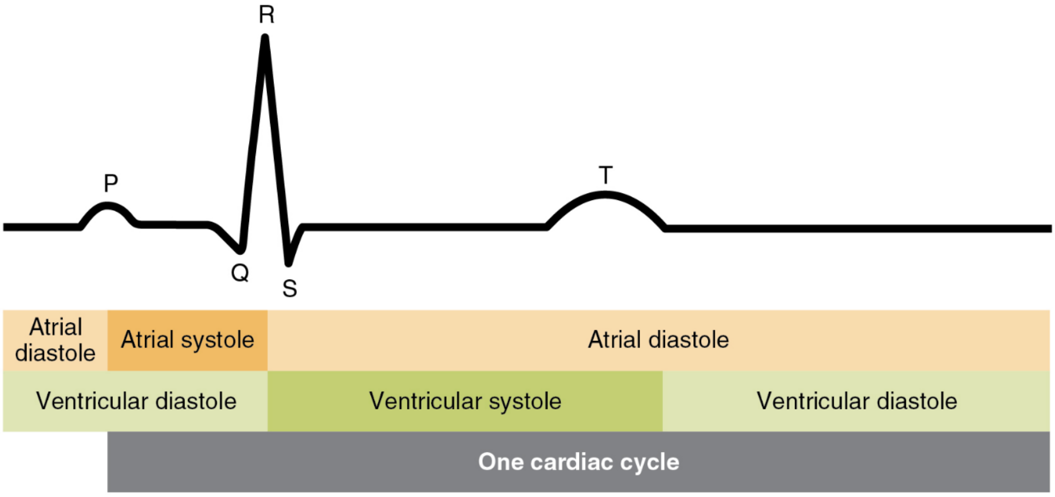

Figure 2.4: One heart beat shown on an electrocardiogram and its relationship to the cardiac cycle. Adapted from [34] and licensed under the Creative Commons Attribution-Share 3.0 International License.

2.3 Atrial Fibrillation

Atrial fibrillation (AF) is an irregular, often fast heart rhythm. During AF, the atria beat chaotically and out of sync with the ventricles, leading to symptoms such as shortness of breath or weakness and a fast pounding heartbeat. However, some people may not have any symptoms.

AF is a progressive disease that typically starts with short silent episodes evolving into longer symptomatic episodes. It can be clinically categorised into four stages based on the episode's duration, which can help guide the treatment options. Patients with paroxysmal AF have an episode of AF that will terminate spontaneously within a maximum of 7 days. Persistent AF, however, will last longer than seven days and will not terminate without pharmaceutical or electrical cardioversion. If the AF lasts longer than one year, it is then categorised as long-lasting persistent AF. If all attempts to restore SR fail, the patient is classed as having permanent AF [39].

2.3.1 AF mechanisms

A variety of complex mechanisms contribute to the development and maintenance of the arrhythmia, mechanisms that are still today not entirely understood. Current research has identified that pathophysiological remodelling of the atria contributes to the creation of an arrhythmogenic substrate that produces electrical phenomena such as rapidly firing foci (often located in the myocardial sleeves of the PVs), multiple re-entrant circuits and rotors, as shown in figure 2.5. The remodelling changes can be categorised into three groups:

(i) electrical remodelling; (ii) structural remodelling, which includes changes in tissues properties and size; and (iii) autonomic remodelling [40].

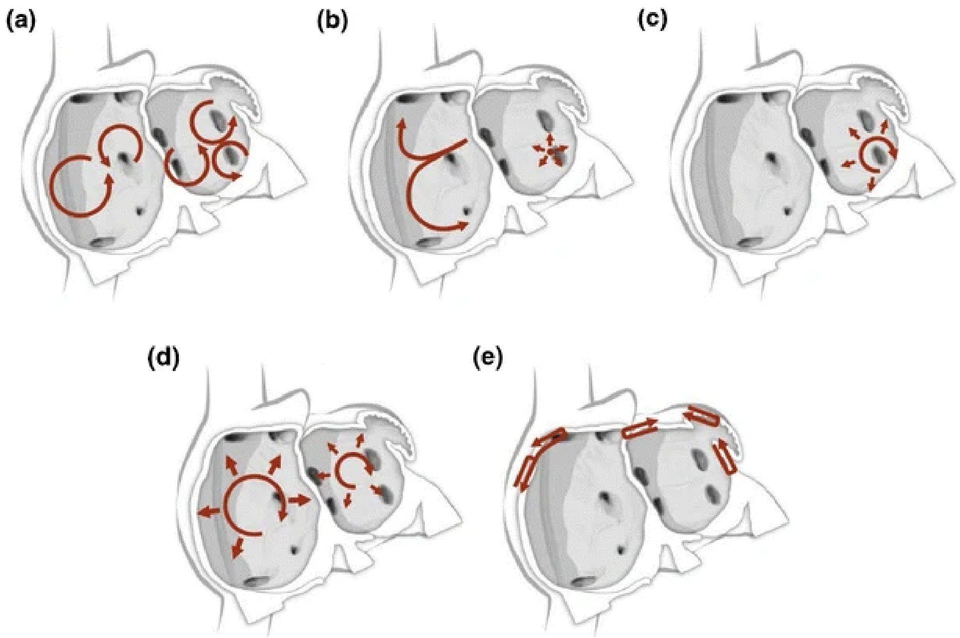

Figure 2.5: Mechanisms of AF. A: multiple wavelets, B: Automatic foci, C: Single re-entrant circuit, D: Functional reentry resulting from rotors or spiral waves, E: AF maintenance resulting from dissociation between epicardial and endocardial layers. Adapted from [41] and licensed under the Creative Commons Attribution-Share 4.0 International License.

Structural remodelling is often associated with fibrosis, with studies showing a strong link between the levels of fibrosis and the progression of AF [42]. Fibrosis can be classified into different categories based on the compactness, pattern and extent [43]. These different types of fibrosis can cause multiple wavelets and other types of reentry due to disordered activation [44], with the density and arrangements affecting the dynamics of the reentry [45]. Patchy fibrosis can cause slowing of the conduction velocity, creating blocks and resulting in local reentrant arrhythmia sources, a known source for AF maintenance [33].

2.3.2 Treatment Options

The first approach to treat AF is to use medicines to control the heart rate and reduce the risk of stroke. These medicines are called anti-arrhythmics and can help restore the heart rhythm and rate to normal [46]. With AF there is a risk of blood clots forming in the heart, which can enter the bloodstream resulting in the patient having a stroke. Therefore, depending on the risk, additional medication may be prescribed to thin the blood and reduce the risk of stroke. Additionally, cardioversion may be recommended for some people [47]. This involves giving a controlled electric shock to the heart to return it to the normal rhythm.

However, patients who have already had AF for a few days have a higher risk of a blood clot forming. Unfortunately, after cardioversion and medicine therapy AF may persist. Often, in this case, patients will undergo catheter ablation. This procedure is used to destroy the diseased tissue in the heart and interrupt the abnormal electrical circuits (more details are provided in section 2.4.3). However, recent guidelines have also recommended using catheter ablation as the first line of therapy (depending on the patient's preference) due to a reduction in arrhythmia-related symptoms and burden compared to patients who underwent medical treatment instead [1].

2.4 Mapping and Ablation

When using catheter ablation to treat the arrhythmia, the diseased tissue maintaining the arrhythmia needs to be identified. This can be done using various mapping techniques such as electro-anatomical mapping (EAM) or image-based methods such as LGE-MRI and Electrocardiographic Imaging (ECGI) [48]. Echocardiography can also be used to detect anatomical and functional changes in the atrial wall [49]. Further details about ECGI and echocardiography will not be discussed. However, the reader is referred to the previously cited references for a more in-depth introduction.

2.4.1 Electro-anatomical Mapping

EAM can be performed by inserting a catheter via the inferior vena cava into the RA and by puncturing the septum, the LA can additionally be mapped. The catheters are dragged across the endocardial surface of the atria. They are then held at various locations in a stable position with contact to the wall while mapping information is acquired, either manually or by automatic point collection.

There are a few commonly used EAM systems such as the CARTO-3 [50], as shown in figure 2.6, EnSite Velocity [51] and Rhythmia [52]. Since CARTO-3 was the only system used in this thesis, further details on the other systems will not be given. However, the reader is referred to the citations for further information.

In the CARTO-3 system, a magnetic field emitter is placed under the operating table beneath the patient's chest. The emitter consists of three coils that generate the magnetic field. Additionally, integrated into the catheters is a miniature passive magnetic field sensor. The sensor can determine the strength of the magnetic fields produced by the coils. This allows the localisation of the catheter in respect to the coils generating the field [53]. With an additional sensor, tissue contact can be additionally confirmed [54].

2.4.1.1 The Electrogram

The mapping catheters also contain electrodes that capture the local electrical potential with respect to a distant reference. Typically the reference is either the Wilson's Central Terminal

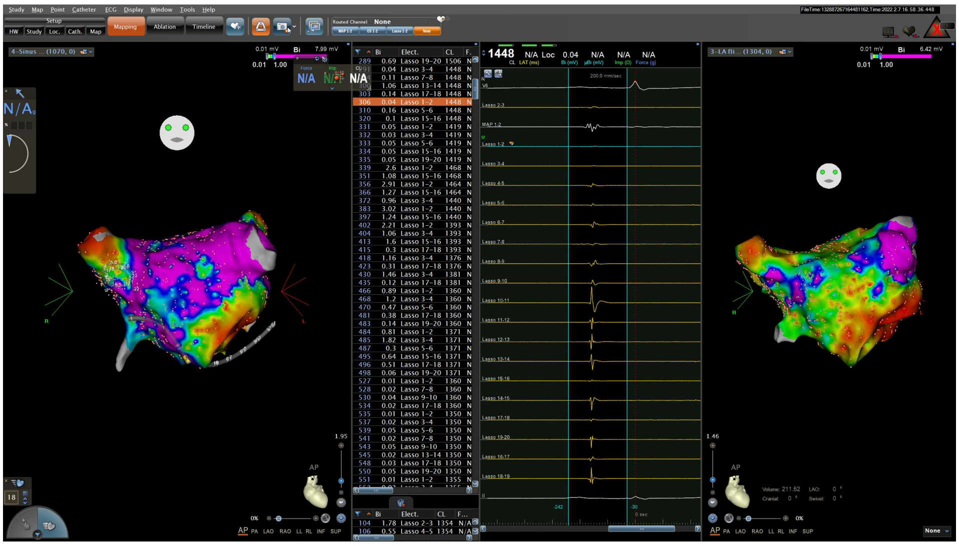

Figure 2.6: Example of a mapping catheter recording the electrical potential and calculating the bipolar voltage map in the CARTO-3 system. On the left: the voltage map has been obtained during SR and on the right: during AF.

(WCT) or a patch electrode placed on the patient's back [55]. The signals acquired in this way are referred to as unipolar electrogram (EGM). These signals can provide local information about the activity surrounding the electrode. However, noise artifacts and ventricular far-field often affect the unipolar signals. In addition, the unipolar signals from two neighbouring electrodes can be subtracted to give a bipolar EGM [56]. This has the advantage of reducing the noise and far-field effects on the signal but poses alternative challenges due to the catheter orientation and the distance between electrodes influencing the signals [23–25].

These mapping systems allow not only the electrical information to be acquired but also provide electrogram parameters such as voltage and local activation time (LAT). The voltage is defined as the peak-to-peak (p2p) amplitude measured in the window of interest and can be calculated using either the bipolar or unipolar EGM. The LAT indicates the point in time when the depolarization wavefront passes underneath the electrode. For unipolar signals, the LAT can be identified as the time of the steepest slope in the signal's window of interest [57]. This is then compared to the activation in the reference signal (often, a catheter in the CS is used). A voltage and LAT map is then obtained by the system by performing interpolation of 5/,mm from the acquired values, providing information on every point of a 3D geometry.

2.4.1.2 Catheter Configurations

The catheters used to obtain the electrical information are composed of insulated wires and electrodes, controlled by a handle and connected to an external recording device. The catheter can be made from Dacron or synthetic materials such as polyurethane and the electrodes are coated in platinum. The catheters usually come in various sizes ranging from 3 to 8 Fr (French gauge) with electrodes 0.4 to 2 mm in length [58]. Different catheters are currently being used in the clinics, as can be seen in figure 2.7. The number of electrodes, the height of the electrodes, the distance between them, and the arrangement can all vary.

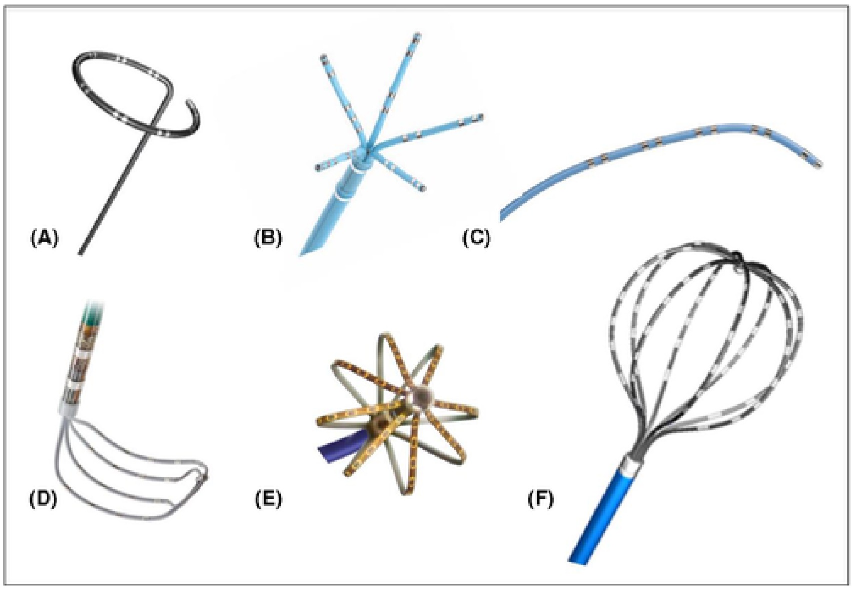

Figure 2.7: Examples of commercially available mapping catheters used in the clinics. (A) Circular loop catheter (Lasso), (B) Five-splined catheter (PentaRay), (C) Linear catheter (Decapolar), (D) Grid catheter (HD Grid), (E) Mini-basket catheter (Orion), (F) Basket catheter (Constellation). From [53] and licensed under the Creative Commons Attribution NonCommercial-NoDerivs License.

2.4.2 LGE-MRI

LGE-MRI is an imaging technique that can detect arrhythmogenic substrate located in the atria by 3D anatomical images. The MRI produces a strong magnetic field using powerful magnets, which force protons in the body to carry out a precession around the axis of the field. A radio-frequency field is then applied to the patient. This causes the protons to flip. When the radio-frequency field is turned off, the protons fall back to their original precession. The amount of time to realign can vary depending on the environment and nature of the molecules. A contrast agent containing gadolinium is often given to the patient before the procedure. This agent causes the speed of proton realignment to increase. In abnormal myocardium, such as areas of fibrotic tissue, there is a later uptake of the contrast agent than in normal healthy myocardium. Therefore, these abnormal areas will show up brighter in images that are acquired later [59].

2.4.3 Catheter Ablation

One common type of ablation procedures is to use radiofrequency ablation, the ablation electrode (typically 3-4 mm in length) delivers a high-frequency current (around 300-1000 kHz) to the underlying tissue. In the myocardium, electromagnetic energy is transformed into thermal energy. The tissue is then destroyed when the temperature exceeds a temperature limit (around 50°) [60]. Another type uses cryoablation, the catheter is used to freeze the tissue and destroy the diseased tissue with extreme cold [61].

Chapter 3

Mathematical Fundamentals

In this chapter, computational models of cardiac electrophysiology are introduced. Then, a brief summary is given of the signal processing methods used in this work, followed by a short description on machine learning aspects and statistical methods.

3.1 Cardiac Modelling

3.1.1 Electrophysiology of the cell

The first work to describe ionic membrane currents by a mathematical model was by Hodgkin and Huxley in 1952 [62]. The authors created an electrical circuit that represents the membrane of giant squid axons. The cell membrane can be represented by a capacitor, the ion channels by resistors in parallel and the Nernst voltages that are represented by voltage sources. The difference between the intracellular potential Φ_i and the extracellular potential Φ_e, is defined as the transmembrane voltage V_m. The transmembrane voltage is determined in the electrical circuit by summing all currents across the membrane. The membrane current is then the sum of the ionic currents plus the capacitive current, resulting in the equation:

$$I_m = C_m \frac{dV_m}{dt} + \sum I_x \tag{3.1}$$

dV_m/dt is the derivative of the transmembrane voltage with respect to the time, I_m is the total current across the cell membrane, C_m the cellular membrane capacitance and I_x is the ion current flow (for one ion species: Na^+,Ca^+,K^+).

In 1998, Courtemanche et al. proposed a specific model of human atrial myocytes which could better represent the atrial electrophysiological behavior [63]. This model contained 11 ion channels, one sodium-potassium pump and one sodium-calcium exchanger.

3.1.2 Bidomain Model

The Courtemanche model provided a tool to represent a single cell. A bi- or monodomain model can be applied to represent the electrical wave propagation on a tissue scale.

Tung et al. introduced the bidomain model to describe excitation propagation across the cardiac tissue divided into an intracellular and extracellular domain [64]. Poisson equations can be used to describe the potentials in each of the domains:

$$\nabla \cdot (\sigma_i \nabla \phi_i) = \beta I_m \tag{3.2}$$

$$\nabla \cdot (\sigma_e \nabla \phi_e) = -\beta I_m \tag{3.3}$$

with I_m being the current through the membrane, ϕ_i and ϕ_e being the intracellular and extracellular potentials, respectively. σ_i and σ_e are the intra- and extracellular conductivity tensors, composed of conductivities along and transversal to the fibre direction.

As previously mentioned, the transmembrane voltage is the difference between the intra- and extracellular domain V_m = ϕ_i - ϕ_e. In the case when no external stimulus is applied, the first and second bidomain equation can be formulated in terms of equation 3.4 and 3.5.

$$\nabla \cdot ((\sigma_i + \sigma_e) \nabla \phi_e) = -\nabla \cdot (\sigma_i \nabla V_m) \tag{3.4}$$

$$\nabla \cdot (\sigma_i \nabla V_m) = \nabla \cdot (\sigma_i \nabla \phi_e) + \beta I_m \tag{3.5}$$

Separating the intra- and extracellular domains is beneficial for running numerical simulations. The bidomain formulation can be reduced to a monodomain model if the assumption of equal anisotropy ratios in the intra- and extracellular domain holds. Since the monodomain model was not used in this work, the reader is directed to Coudiere et al., [65] for further details when interested.

3.1.3 Fast Marching

The Eikonal equation can be used to describe the spread of an activation wave:

$$c\sqrt{\nabla t_a^T \mathbf{G} \nabla t_a} = 1, \tag{3.6}$$

where c(i) is the speed of depolarisation of each node i, t_a(i) is the activation time and G the tensor creating anisotropy in the propagation [66].

The Fast Marching method (FMM) can be used for solving the nonlinear Eikonal equation [67]. It exploits the idea that only adjacent nodes with shorter activation times than the observed node (i) can influence its activation. Since the FMM neglects the diffusion term (in contrast to bi-/monodomain) and only considers the activation (i.e., LATs) while not caring about repolarization, it has a low computational cost compared to other methods.

A geodesic distance is typically a curve representing the shortest path between two points on a surface. For a triangular mesh, the geodesic can be obtained by using the fast marching method described above. This approach can then be very beneficial in the segmentation of the atria into several anatomical regions [68].

3.2 Signal Processing

3.2.1 Principal Component Analysis

Principal Component Analysis (PCA) is a dimension reduction method, often applied to large datasets to maintain most of the information in a smaller subset. It is applied to an $n \times p$ data matrix, where each row n represents a different observation and the columns p a feature.

$$X = \begin{bmatrix} x_{11} & \dots & x_{1p} \\ \vdots & \ddots & \\ x_{n1} & \dots & x_{np} \end{bmatrix} \tag{3.7}$$

The first step is standardisation, where all the variables are transformed to the same scale. This is done by subtracting the mean of the dataset from each observation and dividing it by the standard deviation.

Next, the covariance matrix (Z) is calculated, which is a $p \times p$ symmetric matrix. This provides information on how the input data variables vary from one another. In this way, it can be identified if two variables contain redundant information since they are highly correlated.

$$Z = X^T X. \tag{3.8}$$

To determine the principal components, the eigenvectors and eigenvalues are computed from the covariance matrix. By sorting the eigenvectors in the order of their eigenvalues from highest to lowest, the principal components are obtained in order of how much variance of the data it represents. The data can then be reoriented from the original axes to the one represented by the principal components by the following equation:

$$T = X \cdot W, \tag{3.9}$$

where T represents the resulting principal components matrix and W is the feature vector formed using the eigenvectors of the covariance matrix [69].

3.2.2 Non-Linear Energy Operator

The Non-Linear Energy Operator (NLEO) can be used to calculate the energy of a signal. Using trigonometric identities, the equations about the energy of a mass-spring system can be used for discrete time-domain signals, formulated by equation 3.10 [70].

$$E_n = x_n^2 - x_{n+1}x_{n-1}, \tag{3.10}$$

where the NLEO (E_n) is calculated for the nth time step for three consecutive samples of the signal x. The NLEO is then directly proportional to the square of the amplitude and frequency of the signal. Therefore, it is very beneficial for detecting active segments in a signal. A low-pass filter is usually applied to the NLEO signal to obtain a more robust estimation in the presence of noise.

3.2.3 Conduction Velocity Estimation

The conduction velocity (CV) describes the speed of the propagation of the activation wavefront throughout the atrium [57]. As previously discussed in section 2.4.1.1, a LAT can be calculated at every point on a 3D geometry. To provide a robust CV estimation, T(x) was modelled as a polynomial surface of order 2 and was applied to subsets of spatial coordinates (x_i, t_i), where x_i is the surface mesh vertex and t_i the activation time [71]:

$$T(x) = T(x,y,z) = ax^2 + by^2 + cz^2 + dxy + eyz + fxz + gx + hy + iz + j \tag{3.11}$$

The measured data (x_i, t_i) was then used to fit the polynomial surface by means of a standard least squares algorithm [57] and the coefficients could be computed.

The CV direction v and the magnitude of the conduction velocity $|v|$ could then be found using the following equations:

$$v = \begin{pmatrix} \frac{dx}{dT} \\ \frac{dy}{dT} \\ \frac{dz}{dT} \end{pmatrix} = \begin{pmatrix} \frac{T_x}{T_x^2+T_y^2+T_z^2} \\ \frac{T_y}{T_x^2+T_y^2+T_z^2} \\ \frac{T_z}{T_x^2+T_y^2+T_z^2} \end{pmatrix} \tag{3.12}$$

$$|v| = \frac{1}{\sqrt{T_x^2 + T_y^2 + T_z^2}} \tag{3.13}$$

The components T_x, T_y and T_z could be found by determining the partial derivatives of T(x).

$$T_x = \frac{\partial T}{\partial x} = 2ax + dy + fz + g \tag{3.14}$$

$$T_y = \frac{\partial T}{\partial y} = 2by + dx + ez + h \tag{3.15}$$

$$T_z = \frac{\partial T}{\partial z} = 2cz + ey + fx + i \tag{3.16}$$

3.3 Mean Geometry Construction

To conduct analysis between different patients and mapping modalities where each geometry is distinct, it can be beneficial to map any obtained patient-specific information to a mean geometry. To do so, all meshes need to be rigidly aligned, e.g. by the iterative closest point (ICP) algorithm. Then correspondence is established, as described below, between each individual geometry and a template geometry (chosen as one of the individual geometries).

3.3.1 Establishing Correspondence

To obtain a dense correspondence between each rigidly aligned geometries N and the template geometry, Gaussian process morphable models were used [72]. The template geometry has V_M number of vertices. Gaussian bells were applied to 100 uniformly sampled mesh points on the template. Iteratively, each Gaussian bell was then scaled so that the deformed template with V_M points matches the shape of each rigidly aligned geometry N.

A mean geometry can then be built by taking the mean of all coordinates in each vertex of the deformed template. Correspondence, as described above, was then established between the mean geometry and each aligned geometries N. Using the nearest neighbour search, the closest vertex between the geometry N and the mean geometry can be found. This additionally allows any spatial information on that point to be mapped to the new deformed geometry. Since each vertex of the geometry has an ID and it remains the same after the deformation, the information can be directly related to the mean geometry.

3.4 Machine Learning

3.4.1 Confusion Matrix

A confusion matrix is an appropriate tool for assessing the performance of a classifier. The matrix, as shown in Figure 3.1, represents the number of predicted and actual values. The true positives (TP) and true negatives (TN) indicate the number of positive and negative examples classified correctly. The false positives (TF) is the number of negative examples classified as positive and false negatives (FN) is the number of positive examples classified as negative.

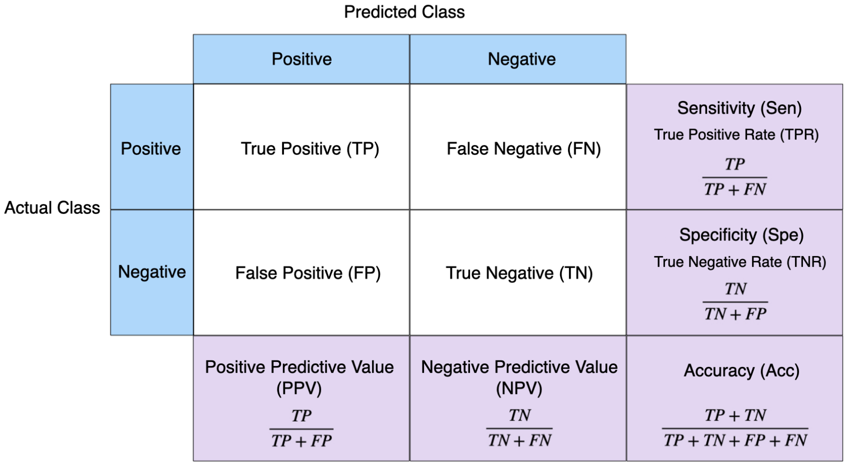

		Predicted Class		
		Positive	Negative	
Actual Class	Positive	True Positive (TP)	False Negative (FN)	Sensitivity (Sen) True Positive Rate (TPR) $\frac{TP}{TP+FN}$
	Negative	False Positive (FP)	True Negative (TN)	Specificity (Spe) True Negative Rate (TNR) $\frac{TN}{TN+FP}$
		Positive Predictive Value (PPV) $\frac{TP}{TP+FP}$	Negative Predictive Value (NPV) $\frac{TN}{TN+FN}$	Accuracy (Acc) $\frac{TP+TN}{TP+TN+FP+FN}$

Figure 3.1: Confusion Matrix.

Multiple metrics can be obtained from the confusion matrix, which can quantify how well the classification performed regarding different aspects. The formulas for the metrics used in this thesis are provided in Figure 3.1.

- Sensitivity: the ratio of true positives to all the positives in the ground truth.
- Specificity: the ratio of true negatives to all negatives in the ground truth.
- Accuracy: the number of predictions the model correctly estimates divided by the number of all samples.
- Positive Predictive Value: the ratio of true positives to all the positives in the predicted class.
- Negative Predictive Value: the ratio of true negatives to all the negatives in the predicted class.

Additional metrics can also be used to evaluate the performance of the classifier. For more information on these metrics, the reader is referred to the work by Singh et al. [73].

3.4.2 Receiver operating characteristic curve

One challenge in a diagnostic test is selecting the threshold that differentiates two classes from one another. The receiver operating characteristic (ROC) curve can be a useful tool to show the performance of the classifier as well as determine the optimal threshold. To obtain the ROC curve, the sensitivity (y-axis) is plotted against 1 - specificity (x-axis), as shown in Figure 3.2.

The optimal threshold to compromise between sensitivity and specificity can then be chosen as the top left hand corner using the following equation:

$$min(\sqrt{(1-Spe)^2+(Sen-1)^2}) \tag{3.17}$$

By calculating the area under the curve (AUC), the ability of the test to discriminate the classes can be evaluated. An AUC of 0.5 would indicate the classifier is no better than flipping a coin to differentiate between classes, whilse an AUC of 1 would indicate it can be done without errors (Figure 3.2 dotted line).

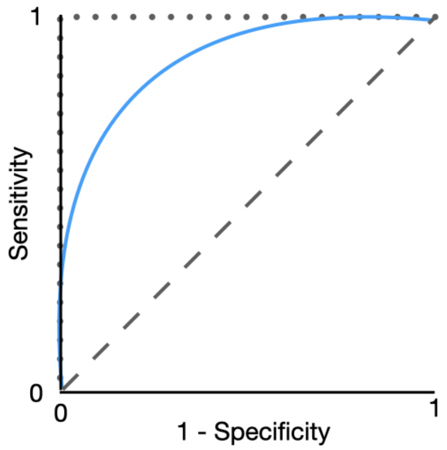

Figure 3.2: ROC curve. The blue line illustrate a common ROC curve that is obtained, with an AUC between 0.5 and 1. The dotted line indicates the best ROC curve (AUC 1) and the dashed line a random classifier (AUC 0.5)

3.4.3 Linear Regression Analysis

Regression analysis is a powerful statistical method to examine the relationship between variables. To conduct the analysis, there needs to be a dependent variable hypothesised to be influenced by other variables. When visualising the relation between the data, the dependent variable can be visualised on the y-axis and the independent variable on the x-axis. For linear regression, a line of best fit is then drawn through the data, referred to as the regression line. This then relates the two variables in terms of the equation:

$$y = mx + c \tag{3.18}$$

A statistical measure often associated with a regression model is the R^2 value.

$$R^2 = 1 - \frac{\sum(y_i - \hat{y}_i)^2}{\sum(y_i - \bar{y})^2} \tag{3.19}$$

where y_i is the actual dependent variable value at sample point i, $\hat{y}_i$ the predicted dependent variable at sample point i from the regression line and $\bar{y}$ the mean of the dependent variable values.

The measure represents the proportion of variance of the dependent variable that is explained by the independent variable. Therefore, $R^2 = 0.75$ would suggest that the independent variable can explain around three-quarters of the observed variation.

3.5 Statistical Measures

3.5.1 Statistical tests

Statistical tests can be used to determine whether observed differences are statistically significant or not. In this work, paired sample t-tests and two-sample t-tests were performed. However, other statistical tests exist which can be relevant for many analyses. A brief overview regarding other statistical tests can be found in the following literature [74]. If the data is normally distributed, the paired t-test is used for matched samples and the two-sample t-test is used for two independent groups. Similarly to other tests, there are two hypotheses: (1) the null hypothesis H_0 where the true mean difference between the paired samples is zero and (2) the alternative hypothesis H_1 where it is not zero. If the null hypothesis is rejected, there is statistical significance. This occurs if the t-value is smaller than a value determined by the tables of t-distribution [75].

The paired sample t-test is used to determine whether the mean difference between two sets of observations is zero. For this test the following equation is used:

$$t = \frac{(\tilde{x} - \mu)}{\frac{s}{\sqrt{n}}} \tag{3.20}$$

where $\tilde{x}$ is the observed mean of the sample, μ theoretical mean of the population, s standard deviation of the sample and n the sample size.

The two sample t-test on the other hand is used to determine whether the two samples are independent random samples from normal distributions with equal means and equal but unknown variances. For this test the following equation is used:

$$t = \frac{(\tilde{x} - \tilde{y})}{\sqrt{\frac{s_x^2}{n} + \frac{s_y^2}{m}}} \tag{3.21}$$

where $\tilde{x}$ and $\tilde{y}$ are the sample means, s_x and s_y are the sample standard deviations and n and m are the sample sizes.

It can be additionally valuable to set a confidence interval for the mean difference to determine the limits that the difference lies in. Usually, the confidence interval is set to 95%. However, 99% can also be used, but then it is more likely that significance would not be obtained. Additionally, the p-value can be calculated to determine the probability of the null hypothesis being true. $p > 0.1$ would indicate there is no evidence against the null hypothesis, while $p < 0.001$ would indicate very strong evidence against it.

3.5.2 Pearson correlation coefficient

Pearson's correlation coefficient is a measure of the linear correlation of two sets of data. It is the ratio between the covariance of the variables and the product of their standard deviations, as seen by equation 3.22:

$$r = \frac{\sum (x_i - \bar{x})(y_i - \bar{y})}{\sqrt{\sum (x_i - \bar{x})^2 \sum (y_i - \bar{y})^2}} \tag{3.22}$$

where r is the correlation coefficient, x_i and y_i are the x- and y-variable values in samples, $\bar{x}$ and $\bar{y}$ the mean of the x- and y-variable values. The correlation coefficient can range from -1 to 1, with 1, -1 and 0 indicating a positive, negative and no linear relationship between the variables, respectively [76].

Chapter **4**

Determinants of Bipolar Voltage Mapping

One common approach to identify atrial pathological substrate is to perform bipolar voltage mapping. However, the angle of the catheter with respect to the propagating wavefront, the distance between electrodes and the electrode size can, in addition to pathological substrate, affect the measured voltage at the surface of the tissue [23–25, 77, 78]. In silico experiments have allowed replicating detailed and control scenarios that allow the quantitative evaluation of the differences that affect the bipolar voltage mapping and its ability to discriminate healthy from fibrotic atrial substrate. It was found that with an increase of distance between two electrodes (up to a maximum distance), the bipolar voltage increases, with a change as big as 2 mV when ranging from 1.2 mm to 6 mm between electrodes [25]. Moreover, the catheter orientation greatly impacts the bipolar voltage, especially when the electrodes are parallel to the tissue, as the subtraction of the two unipolar signals may result in the bipolar voltage dropping to zero, even if the underlying tissue is healthy [23]. However, the dependence of the angle on the bipolar voltage is less pronounced when using an electrode distance greater than 3.6 mm in healthy tissue [25]. Additionally, Anter et al. showed that the total area of low voltage was smaller when using a mapping catheter with small-sized electrodes (1 mm) in comparison to mapping with the ablation catheter with a 3.5 mm-sized tip-electrode [24]. Thus, the fore-mentioned catheter characteristics can affect the determination of low voltage areas as potential ablation targets in bipolar voltage mapping. Therefore, mapping catheters could potentially guide clinicians to falsely ablate healthy tissue or not ablate key areas driving the arrhythmia. To counter these challenges, voltage mapping could be performed using unipolar signals rather than bipolar signals. However, although the fore-mentioned effects of the catheters do not influence the unipolar signals, the signals are more susceptible to noise and ventricular far-field [79].

In the first section of this chapter, we sought to investigate the extent of the catheter characteristics' impact on identifying LVS. In the study, published in Frontiers in Physiology [80], high-resolution bipolar and unipolar low voltage maps in SR and AF were compared. Analysis was performed, investigating (i) the spatial concordance of bipolar to unipolar voltage for low-voltage regions, (ii) deriving optimal low-voltage unipolar thresholds to identify pre-specified bipolar low voltage areas in SR and AF, and (iii) the effect of the bipolar electrode spacing. It was found that despite the catheter factors known to influence the bipolar voltage, a high correlation (agreement 90 ± 5 % in SR and 85 ± 5 % in AF) was found between the bipolar and unipolar voltage mapping. Additionally, the bipolar electrode distance was found to have little impact on the agreement. One hypothesis was that the wavefront is never precisely perpendicular to a bipolar pair and arrives at both electrodes simultaneously in a three-dimensional space due to the degree of curvature introduced into the wave.

In order to further understand why the correlation between unipolar and bipolar voltage mapping is so high, a simulation setup was created, where a replica of a clinical catheter was placed in a left atrium. The second section presents details of the simulation performed as part of a student thesis. It was identified that even in a three-dimensional space, the wavefront could reach two electrodes simultaneously for small inter-electrode distances, resulting in a drop of the bipolar voltage below the defined cut-off value for low voltage. However, this only occurred for 5-10 % of bipolar pairs in one catheter position in the atrium. Additionally, in between high and low voltage areas where the unipolar values are close to the unipolar threshold, the bipolar voltage may drop below or above the threshold oppositely depending on when the wavefront reaches both electrodes. Although these changes in bipolar voltage could cause low voltage areas to be slightly bigger or smaller in diameter than the area of pathological substrate, the specific region identified to be ablated remains the same between mapping modalities. However, perhaps the ablation should be performed with a slight reduction in the size of the area to prevent healthy tissue from being ablated.

In the last section, the impact of the electrode sizes on the voltage is studied. In this conference paper [81], a 2D patch simulation was created, where the electrodes' size was varied on both healthy and diseased tissue. An inverse relationship was found between the electrode size and the voltage, with more substantial differences (11 to 6 mV) occurring for electrodes of smaller sizes (0.2-0.8 mm). The impact of the electrode size on the voltage was also seen in diseased tissue. However, when the fibrosis was on the endocardium, the effect was less pronounced, with the voltages ranging from 2 to 0.5 mV when changing the electrode size from (0.2-0.8 mm). Centres using catheters with small electrodes should be careful when applying cut-off values to locate low voltage identified using larger electrode sizes. Ideally, universal electrode size should be used to allow for direct translation and applicability between centres.

The work presented in this chapter can provide confidence that bipolar voltage mapping is a robust tool for identifying low voltage areas without the catheter angle or the distance between the electrodes playing a significant role in distorting the bipolar voltage values. Additionally, using the provided optimal unipolar thresholds could help determine the correct size of the low voltage area to be ablated, potentially reducing the risk of ablating healthy tissue falsely characterised as diseased. Finally, awareness was created of the impact of the electrode size and how caution should be taken when applying cut-off values to discriminate healthy from fibrotic tissue with different mapping catheters, specifically alternative electrode sizes, at different centres.

4.1 Comparison to Unipolar Voltage Mapping

frontiers in Physiology

ORIGINAL RESEARCH
published: 26 November 2020
doi: 10.3389/fphys.2020.575846

Comparison of Unipolar and Bipolar Voltage Mapping for Localization of Left Atrial Arrhythmogenic Substrate in Patients With Atrial Fibrillation

Deborah Nairn[1*†], *Heiko Lehrmann*[2†], *Björn Müller-Edenborn*[2], *Steffen Schuler*[1], *Thomas Arentz*[2], *Olaf Dössel*[1], *Amir Jadidi*[2†] *and Axel Loewe*[1†]

[1] *Institute of Biomedical Engineering, Karlsruhe Institute of Technology (KIT), Karlsruhe, Germany,* [2] *Department of Electrophysiology, University-Heart-Center Freiburg-Bad Krozingen, Bad Krozingen, Germany*

OPEN ACCESS

Edited by:
Sanjiv M. Narayan,
Stanford University, United States

Reviewed by:
Prasanth Ganesan,
Stanford University, United States
Vijay S. Chauhan,
Peter Munk Cardiac Centre, Canada

***Correspondence:**
Deborah Nairn
publications@ibt.kit.edu

[†] *These authors have contributed equally to this work*

Specialty section:
This article was submitted to Cardiac Electrophysiology, a section of the journal Frontiers in Physiology

Received: *24 June 2020*
Accepted: *20 October 2020*
Published: *26 November 2020*

Citation:
Nairn D, Lehrmann H, Müller-Edenborn B, Schuler S, Arentz T, Dössel O, Jadidi A and Loewe A (2020) Comparison of Unipolar and Bipolar Voltage Mapping for Localization of Left Atrial Arrhythmogenic Substrate in Patients With Atrial Fibrillation. Front. Physiol. 11:575846. doi: 10.3389/fphys.2020.575846

Background: Presence of left atrial low voltage substrate in bipolar voltage mapping is associated with increased arrhythmia recurrences following pulmonary vein isolation for atrial fibrillation (AF). Besides local myocardial fibrosis, bipolar voltage amplitudes may be influenced by inter-electrode spacing and bipole-to-wavefront-angle. It is unclear to what extent these impact low voltage areas (LVA) in the clinical setting. Alternatively, unipolar electrogram voltage is not affected by these factors but requires advanced filtering.

Objectives: To assess the relationship between bipolar and unipolar voltage mapping in sinus rhythm (SR) and AF and identify if the electrogram recording mode affects the quantification and localization of LVA.

Methods: Patients (n = 28, 66±7 years, 46% male, 82% persistent AF, 32% redo-procedures) underwent high-density (>1,200 sites, 20 ± 10 sites/cm^2, using a 20-pole 2-6-2 mm-spaced Lasso) voltage mapping in SR and AF. Bipolar LVA were defined using four different thresholds described in literature: <0.5 and <1 mV in SR, <0.35 and <0.5 mV in AF. The optimal unipolar voltage threshold resulting in the highest agreement in both unipolar and bipolar mapping modes was determined. The impact of the inter-electrode distance (2 vs. 6 mm) on the correlation was assessed. Regional analysis was performed using an 11-segment left atrial model.

Results: Patients had relevant bipolar LVA (23 ± 23 cm^2 at <0.5 mV in SR and 42 ± 26 cm^2 at <0.5 mV in AF). 90 ± 5% (in SR) and 85 ± 5% (AF) of mapped sites were concordantly classified as high or low voltage in both mapping modes. Discordant mapping sites located to the border zone of LVA. Bipolar voltage mapping using 2 vs. 6 mm inter-electrode distances increased the portion of matched mapping points by 4%. The unipolar thresholds (y) which resulted in a high spatial concordance can be calculated from the bipolar threshold (x) using following linear equations: $y = 1.06x + 0.26\,mV$ ($r = 0.994$) for SR and $y = 1.22x + 0.12\,mV$ ($r = 0.998$) for AF.

Conclusion: Bipolar and unipolar voltage maps are highly correlated, in SR and AF. While bipole orientation and inter-electrode spacing are theoretical confounders, their impact is unlikely to be of clinical importance for localization of LVA, when mapping is performed at high density with a 20-polar Lasso catheter.

Keywords: atrial fibrillation, bipolar voltage mapping, unipolar voltage mapping, arrhythmogenic substrate, low voltage areas

1. INTRODUCTION

Atrial fibrillation (AF) is the most common supraventricular cardiac arrhythmia characterized by an irregular heart rhythm and associated with an increased risk of heart failure, stroke, and mortality (Wang et al., 2003; Miyasaka et al., 2005; Go et al., 2014).

Pulmonary veins have been identified as major arrhythmogenic trigger sites for AF. Therefore, their isolation has become a widely used and effective treatment for AF (Haissaguerre et al., 1998). However, additional arrhythmogenic atrial substrate is present in 30–50% of persistent AF patients and may be responsible for the maintenance of the arrhythmia, resulting in increased AF recurrences after pulmonary vein isolation (PVI) in these patients (Verma et al., 2005, 2015). Procedural identification of arrhythmogenic AF sources with rapid, continuous, or repeated rotational activity has revealed their localization within fibrotic regions displaying low bipolar voltage <0.5 mV during AF (Jadidi et al., 2016, 2020; Seitz et al., 2017). Ablation of these atrial AF sources, in addition to PVI, improves the success rate in persistent AF patients from 30 to 50% with PVI only to 70% with additional selective ablation of arrhythmogenic low voltage areas (LVA) (Rolf et al., 2014; Jadidi et al., 2016; Blandino et al., 2017; Seitz et al., 2017).

Atrial arrhythmogenic fibrosis-rich areas are currently identified using imaging or bipolar voltage mapping. However, in addition to the underlying atrial fibrosis that affects the bipolar voltage (peak-to-peak amplitude of the electrogram), the angle of the bipolar recording electrodes (wavefront-to-bipole orientation), the distance between the electrodes and the electrode size may also influence the bipolar electrogram amplitudes (Schuler et al., 2013; Anter et al., 2015; Beheshti et al., 2018; Lin et al., 2018; Gaeta et al., 2019). Therefore, using bipolar electrograms can potentially cause areas of fibrotic and non-fibrotic tissue to be misclassified. On the other hand, unipolar electrogram voltage is unaffected by the catheter orientation and electrode distances. However, the signals are more susceptible to noise and ventricular far-field requiring advanced filtering (Frisch et al., 2020).

We aim to assess the differences in the extent and distribution of atrial LVA when comparing bipolar to unipolar voltage mapping in AF and sinus rhythm (SR). In this work, we evaluate the correlation between the two mapping methods and identify the corresponding unipolar thresholds that yield the highest concordance to the bipolar LVA. Additionally, we examine the impact of (1) the electrode distance, (2) the anatomical region of the left atrium, and (3) the extent of left atrial (LA) low voltage substrate on the correlation between unipolar and bipolar LVA.

2. METHODS

2.1. Study Cohort and Electro-Anatomical Mapping

A total of 28 patients with AF underwent high-density (>1,200 mapped sites per LA and rhythm, mapping density of 17 ± 7 sites per cm^2 in SR and 22 ± 11 per cm^2 in AF) voltage mapping using a 20-pole variable (15–20 mm diameter) Lasso-Nav mapping catheter (electrode size: 1 mm; spacing: 2-6-2 mm). The voltage mapping was performed using CARTO-3 (Biosense Webster, Diamond Bar, CA, USA) and carried out in both rhythms SR and AF prior to PVI. Bipolar voltage maps were acquired using all electrode spacings (2 and 6 mm). Patients were mapped first in the rhythm that they presented in and then cardioverted into SR or induced into AF to obtain the second map. 21/28 patients presented with clinical persistent AF, the remaining had SR at presentation. Nine of the 28 (32%) patients underwent a redo AF ablation procedure after a previous PVI procedure. The remaining 19 (68%) patients came for their first AF ablation procedure.

Electrograms recorded >7 mm from the geometry surface were excluded from the analysis to avoid poor contact points. Additionally, points containing only noise or pacing artifacts were removed based on manual assessment. The unipolar signals were processed by the Carto3 software, which uses standard clinical filtering with highpass and lowpass cutoff frequencies at 2 and 240 Hz to remove high and low frequency noise from the acquired EGM. Additionally, a notch filter was applied to clear the noise from the environment power lines. For the unipolar recordings Wilson's Central Terminal (WCT) was used as the reference electrode. Additionally, bandpass filtering was performed at 16–500 Hz for the bipolar signals. A window of interest was defined prior to the QRS complex to identify atrial activity and the voltage provided by CARTO-3 was obtained by taking the peak-to-peak value (local maximum − local minimum) of a single atrial beat in a 2.5 s second recording interval. This beat was identified to be, typically, the largest or second-largest beat in the signal, where the spread in the voltage within the time window differed in a range of 0–0.2 mV. A color interpolation of voltage values between the recorded electrode positions of <7 mm was then applied to the geometry automatically by CARTO-3.

2.2. Voltage Mapping in Sinus Rhythm

The QRS complex was excluded from the window-of-interest during LA voltage mapping. LVA were defined using cut-off values for bipolar peak-to-peak voltage in SR of <0.5 or <1.0 mV (Jadidi et al., 2016; Rodríguez-Mañero et al., 2018). Areas demonstrating low voltage when mapped with the 20-pole Lasso catheter were confirmed using a contact force-sensing mapping catheter with a contact threshold of >5 g.

2.3. Voltage Mapping in Atrial Fibrillation

Patients underwent voltage mapping in AF using the sharp peak in the surface QRS as the reference. The QRS complex was then excluded from the window-of-interest during LA voltage mapping. To ensure the highest accuracy of electrogram criteria, >1,200 points were acquired per LA and rhythm. Respiratory gating was performed and the atrial geometry was acquired at high adjustment settings (geometry acquisition by Lasso catheter was set to 18 on CARTO-3) to obtain the highest accuracy of the acquired atrial geometry. Presence and accurate localization of low voltage areas was confirmed by contact force-sensing catheters (>5 g). Bipolar low voltage zones were defined as <0.35 or <0.5 mV in AF, according to the findings in recent studies (Jadidi et al., 2016, 2020; Rodríguez-Mañero et al., 2018).

The voltage was defined as the peak-to-peak amplitude of a single AF beat. In AF, the window of interest was set to 90% of the mean AF cycle length in order to consider only a single AF beat. This beat was manually selected with special emphasis on having only a single depolarization wavefront (AF beat). The current voltage mapping software of CARTO-3.7 does not support automatic voltage mapping during AF. Use of the automatic CARTO-3 software for voltage mapping in AF may result in mapped sites without any underlying electrogram (including the isolelectric intervals only) or including multiple AF beats with inadequate peak-to-peak voltage measurements. Therefore, in the current study, AF voltage maps were acquired manually.

2.4. Analysis

To identify the correlation between the unipolar and bipolar maps, the sensitivity, and specificity were calculated. The bipolar map was considered as the "true condition" and the electrogram at each point of the unipolar map was classified depending on the unipolar voltage threshold. Points labeled as low voltage in the (ground truth) bipolar map were identified as true positive (unipolar voltage < threshold) or false negative (unipolar voltage > threshold) in the unipolar map. True negative and false positive classes were similarly defined for the points with a supra-threshold voltage in the bipolar map. The unipolar threshold was then varied between 0.1 and 4 mV, and a receiver operating characteristic (ROC) curve was created to identify the unipolar threshold which provides the best match to the bipolar map for each patient and rhythm.

The relationship between unipolar and bipolar voltage was further explored by examining the percentage of points on the maps, which were classified the same in both cases (low or high voltage). This analysis was performed based on the voltage map provided by CARTO-3 (interpolated map data). The data from the electrograms at the mapping sites were used directly to analyze the effect of inter-electrode spacing.

For each patient, the best unipolar threshold corresponding to a specific bipolar threshold was identified using the ROC curve. Using one common unipolar threshold for all patients rather than an individual threshold for each patient was evaluated and analyzed by calculating the percentage of points that matched in unipolar and bipolar.

Regional differences in the voltage have been found in patients, with the anteroseptal LA wall and roof displaying the common and most extensive LVA, followed by the posterior LA wall (Marcus et al., 2007; Müller-Edenborn et al., 2019). To examine what effect the regional differences may have on the correlation between unipolar and bipolar LVA, each LA was split into 11 anatomical regions. The regions are as follows: orifices to the four pulmonary veins (LIPV, LSPV, RIPV, RSPV), the region around the mitral valve (MV), the left atrial appendage (LAA), the anterior, posterior, and lateral wall, the roof, and the septum. The percentage of points which matched between the unipolar and bipolar map were calculated for each anatomical region, using the bipolar threshold of 0.5 mV in SR and 0.35 mV in AF and the best corresponding unipolar threshold for each patient, which range between 0.62 and 1.1 mV (SR) and 0.45 and 0.99 mV (AF).

A factor that may influence the correlation between bipolar and unipolar mapping is the level of low voltage substrate in patients. Therefore, the 28 patients were split into four subgroups depending on the extent of low voltage (<0.5 mV during SR in the bipolar map). The low voltage substrate extent was then determined as the percentage of the surface area. Each patient was categorized into one of the four groups: stage I (<5%), II (≥5% to <20%), III (≥20% to <30%) and IV (≥30%) as suggested by Oakes et al. (2009) and Yamaguchi et al. (2018). The match between unipolar and bipolar classification was then calculated for each category, in both rhythms.

The distance between the bipolar electrodes is known to affect the bipolar signals (voltage increases as the distance increases) (Beheshti et al., 2018). Several studies have examined this effect concerning the influence it may have on the identification of LVA (Anter et al., 2015; Mori et al., 2018). Thus, the data provided by CARTO-3 were split into three groups: (1) containing only information from the 2 mm electrode distances, (2) only 6 mm distances, and (3) containing both. The percentage of points that matched between unipolar and bipolar was then calculated, and the paired-sample *t*-test was used to calculate if the difference between the three sets was significant.

3. RESULTS

3.1. Patient Characteristics

Twenty-eight patients (66 ± 7 years old, 46% male, 82% persistent AF, 32% redo-procedures) underwent high-density (>1,200 sites, with a mapping density of 17 ± 7 sites per cm^2 in SR and 22 ± 11 per cm^2 in AF, using a 20-polar 2-6-2 mm-spaced Lasso, CARTO-3) voltage mapping in SR and AF prior to PVI. Further details on patients' characteristics are provided

TABLE 1 | Patient clinical demographics.

Patient characteristics	Total = 28
Rhythm at presentation (AF, %)	21 (75)
Persistent AF (%)	23 (82)
Age	66 ± 7
Male, *n* (%)	13 (46)
BMI (kg/m^2)	28 ± 4
Weight (kg)	84 ± 13
LVEF (%)	54 ± 10
LA diameter (AP, mm)	46 ± 5
IVSEDD (mm)	10 ± 2
SHD (%)	12 (43)
CHA_2DS_2-VASc score	2.2 ± 1.8
Hypertension (%)	16 (57)
LV systolic dysfunction (<45%)	9 (32)
Diabetes (%)	4 (14)
Renal failure (GFR<50 ml/min, %)	8 (29)
History of stroke (%)	1 (3.6)
Coronary artery disease (%)	3 (11)
Antiarhythmic therapy except betablocker (%)	14 (50)
Beta blocker therapy (%)	21 (75)
Amiodarone (%)	6 (21)
Flecainide (%)	5 (18)
Sotalol (%)	1 (3.5)
Dronedarone (%)	2 (7)
Redo procedure for AF	9 (32)

LVEF, left ventricular ejection fraction; SHD, structural heart disease; LV, left ventricular; BMI, body mass index; GFR, glomerular filtration rate.

TABLE 2 | Mapping information of patients included in the study.

Electro-anatomical mapping	SR	AF
Low voltage surface area [cm^2 (%)] (SR and AF < 0.5 mV)	23 ± 23 (31 ± 30)	42 ± 26 (52 ± 30)
Map points (pts)	1,536 ± 608	1,978 ± 925
Map points after processing (pts)	1,200 ± 632	1,639 ± 754
Bipolar voltage (mV)	1.15 ± 0.67	0.54 ± 0.22
Unipolar voltage (mV)	1.44 ± 0.71	0.73 ± 0.23

in **Table 1**. Additionally, information on the electro-anatomical mapping across all patients is provided in **Table 2**.

3.2. Spatial Distribution of Left Atrial Low Voltage Areas in Unipolar vs. Bipolar Mapping

The three-dimensional distribution patterns of the bipolar vs. unipolar LVA were highly concordant for all analyzed voltage thresholds and in all patients. 90 ± 5 and 85 ± 5% of mapped sites in SR and AF, respectively, were concordantly classified as low or high voltage both in bipolar vs. unipolar mapping mode. Discordant mapping sites located to the border zone of LVA.

Figure 1 illustrates the three-dimensional distribution patterns of the bipolar vs. unipolar LVA for a single patient with electrogram examples. LVA were found at the same positions in the unipolar and bipolar maps using a unipolar threshold of 0.78 mV when the bipolar threshold was 0.5 mV. The classification map, in **Figure 1** lower panels, identifies mapping sites where the maps disagree with regard to LVA in unipolar vs. bipolar mode. Such areas with different classification of LVA were mostly located at border zones, where the myocardial voltage amplitudes are changing from low to high voltage. The difference between the selected threshold value to the voltage values of miss-classified electrograms was found to be 0.3 ± 0.1 mV. **Figure 2** shows similar results for bipolar vs. unipolar voltage maps acquired during AF. Additionally, the three-dimensional distribution patterns of LVA in unipolar and bipolar voltage maps are illustrated for all 28 patients in **Supplementary Figures 1**, **2**. In these figures, the Pearson correlation coefficient between the bipolar and unipolar voltage maps prior to applying a threshold is shown for each patient. For both rhythms the correlation was found to be 0.88 ± 0.05, indicating a strong positive correlation between the mapping modalities independent of a specific threshold.

3.3. Spatial Correlation Between Unipolar vs. Bipolar Voltage Mapping—Regional Analysis

The overall three-dimensional distribution patterns of LA LVA during SR and AF (**Supplementary Figures 1**, **2**) reveal a very high spatial concordance with very similar localization of LVA when comparing bipolar and the best correlated unipolar voltage thresholds. Further detailed regional quantification of the amount of concordant LVA classification between unipolar vs. bipolar voltage mapping is reported in **Figure 3**. The figure shows regional correlation results when splitting the LA into 11 anatomical regions. The mean percentage of concordantly categorized electrograms for each anatomical region divided by the number of electrograms within the same region (across all patients) is presented on an example geometry. Additionally, the mean and standard deviation values for each region can be seen in **Table 3**. For both rhythms, the LAA was one of the regions showing the highest agreement between the unipolar and bipolar voltage maps with 98% match in SR and 95% in AF. The pulmonary veins also display high agreement (93–96% SR and 94–97% AF). A slightly lower but still high regional similarity between the unipolar and bipolar maps was found within the body of the LA: LA posterior wall, anterior wall and the septum (90, 90, and 91% in SR and 87, 87, and 91% in AF). The high regional correlation between unipolar and bipolar voltage maps is well-reflected by the distribution of LVA patterns on the high-density interpolated electro-anatomical voltage maps (**Supplementary Figures 1**, **2**). Independently of the underlying rhythm, the three-dimensional localization of the arrhythmogenic LVA is highly concordant and designates the

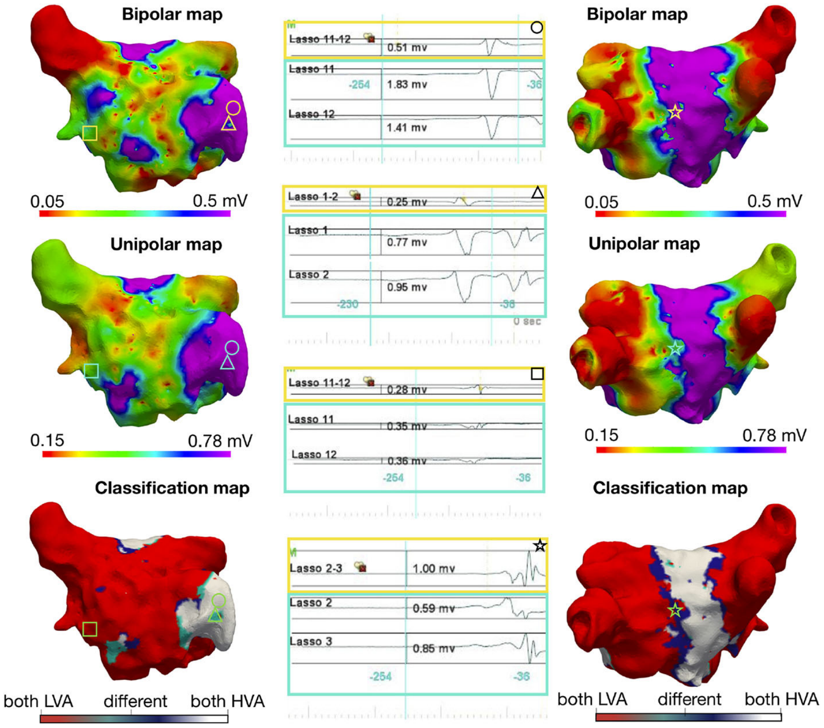

FIGURE 1 | Voltage mapping in sinus rhythm: Three-dimensional distribution of bipolar and unipolar LVA in a patient during SR with a bipolar threshold <0.5 mV. The top row indicates the bipolar map, the middle row shows the unipolar map, and the bottom row is a map of the point by point comparison between the two maps: if both points are below their indicated voltage thresholds (LVA), the point is colored red, if both are above [high voltage areas (HVA)] in white and with different classification (bipolar low voltage, unipolar high voltage) in dark-blue and (bipolar high voltage, unipolar low voltage) in turquoise. In the left column, the anterior view is shown and on the right the posterior view. Each geometric shape represents a point on the map where the corresponding signal is shown in the middle column. The upper unipolar threshold values were obtained by determining which threshold provided the best match of points between unipolar and bipolar. For visualization, the lower value was manually optimized to obtain the best visual match.

same regions as potential ablation targets in unipolar and bipolar voltage mapping mode.

3.4. The High Correlation Between Unipolar and Bipolar Voltage Maps Is Independent of the Underlying Extent of Low Voltage Substrate

The LA voltage maps of all 28 patients were categorized according to the extent of their LA low voltage substrate <0.5 mV in SR, as mentioned in section 2: seven patients in stage I, eight in stage II, five in stage III, and eight in stage IV. The low voltage surface area in SR at <0.5 mV bipolar threshold (mean ± standard deviation) in each group was: stage I: 3 ± 2%, stage II: 12 ± 5%, stage III: 27 ± 4%, stage IV: 37 ± 4%. The percentage of points that matched in the bipolar and unipolar voltage maps for patients with different levels of low voltage substrate is shown in **Supplementary Figure 3**. For all low-voltage substrate stages in both rhythms, the percentage of mapping points that matched was >85% (mean). The maximum difference between categories was 4%.

3.5. Specific Unipolar Voltage Thresholds Are Associated With High Correlation Between Unipolar vs. Bipolar Low Voltage Substrate

Figure 4 illustrates the ROC curves for the optimal unipolar voltage thresholds that result in the highest concordance of electrogram classifications to high and low voltage areas in both unipolar and bipolar maps for four previously described bipolar voltage thresholds. For each rhythm and voltage threshold, there was a high percentage of agreement (sensitivity and specificity >80% in all cases). The highest sensitivity and specificity values (93, 81%) were obtained when comparing the maps in SR using a bipolar threshold of 1 mV and a unipolar threshold of 1.31 mV. Sensitivity and specificity values were as follows for the other cases: SR with bipolar threshold of 0.5 mV (unipolar threshold 0.83 mV, 89%, 84%), AF 0.5 mV (unipolar 0.71 mV, 91%, 79%), and AF 0.35 mV (unipolar 0.54 mV, 85%, 82%).

To further examine the relationship between the bipolar and the unipolar voltage threshold, a set of SR and AF ROC curves were created for each bipolar threshold between 0.1 and

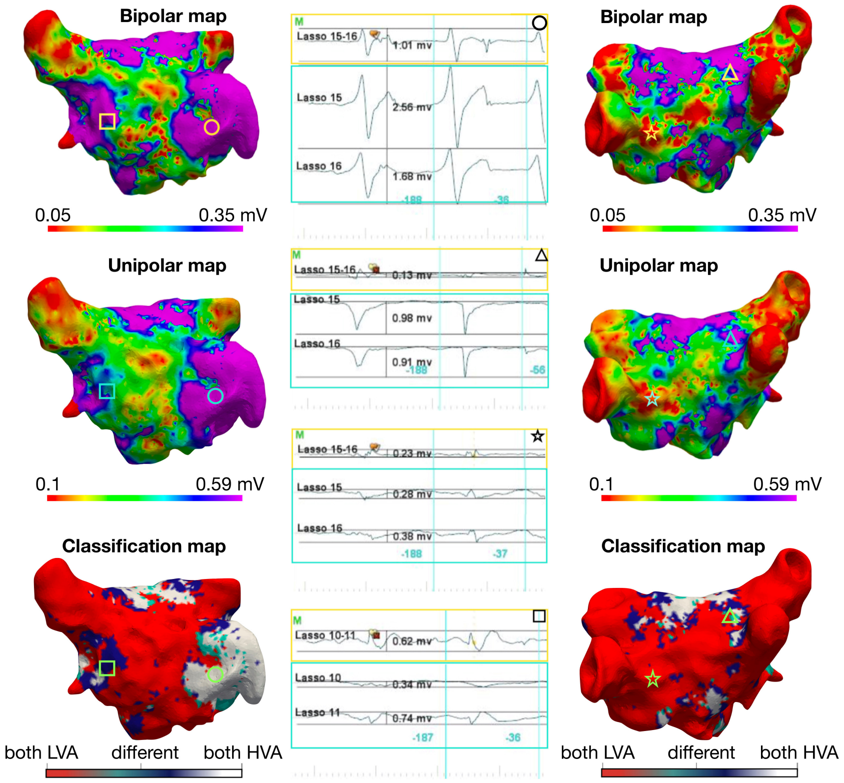

FIGURE 2 | Voltage mapping in atrial fibrillation: Three-dimensional distribution of bipolar and unipolar LVA in the same patient as **Figure 1** during AF with a bipolar threshold <0.35 mV. The top row indicates the bipolar map, the middle row shows the unipolar map, and the bottom row is a map of the point by point comparison between the two maps: if both points are below their indicated voltage thresholds (LVA), the point is colored red, if both are above [high voltage areas (HVA)] in white and with different classification (bipolar low voltage, unipolar high voltage) in dark-blue and (bipolar high voltage, unipolar low voltage) in turquoise. In the left column, the anterior view is shown and on the right the posterior view. Each geometric shape represents a point on the map where the corresponding signal is shown in the middle column. The electrogram marked with a triangle is an example of "voltage cancelation" in the bipolar recording (0.13 mV), while the voltages on both unipolar recordings are high (0.98 and 0.91 mV); this occurs because the unipolar electrograms have the same shape and same timing and their subtraction results in a near-zero bipolar voltage value.The upper unipolar threshold values was obtained by determining which threshold provided the best match of points between unipolar and bipolar. The lower value was selected manually to obtain the best visual match.

1 mV, in steps of 0.1 mV. In this way, the optimal unipolar threshold for each bipolar threshold was identified, which gave the highest classification match between the mapping modalities. The unipolar threshold values were then plotted against the bipolar threshold values, as shown in **Figure 5**. Linear regression yielded the following relations: $y = 1.06x + 0.26\,mV$ for SR and $y = 1.22x + 0.12\,mV$ for AF, where y is the unipolar threshold and x is the bipolar threshold in mV. The correlation coefficient between the two variables (bipolar and unipolar threshold) shows a strong positive correlation for both rhythms (0.994 in SR and 0.998 in AF). However, as there is spread between values for individual patients, the y-intercept cannot be as reliably determined as the slope of the relation. A simplified calculation of the corresponding unipolar threshold is provided by the addition of 0.3 vs. 0.2 mV to the bipolar voltage threshold in SR vs. AF, respectively (unipolar threshold error <0.07 mV in the bipolar threshold range between 0.1 and 1 mV).

3.6. Comparison of Unipolar and Bipolar Low Voltage Areas Using a Common vs. a Patient-Specific Unipolar Threshold

The difference between using one universal unipolar threshold for all patients (**Figure 4**), vs. patient-specific thresholds were evaluated to assess the variability in identifying low voltage areas. **Figure 6** illustrates that the increase in electrogram classification accuracy with the use of patient-specific vs. a common unipolar threshold is marginal (1–2%). For SR with a bipolar threshold 1 mV, the improvement in substrate classification changed from median of 92.7% using a common unipolar threshold to 92.9% using a patient-specific unipolar threshold. Using a Wilcoxon rank sum test, the difference between using one common threshold or individual thresholds was found to be not significant for either rhythm or bipolar threshold used. From **Figure 5** the best unipolar threshold for each patient can be seen in a

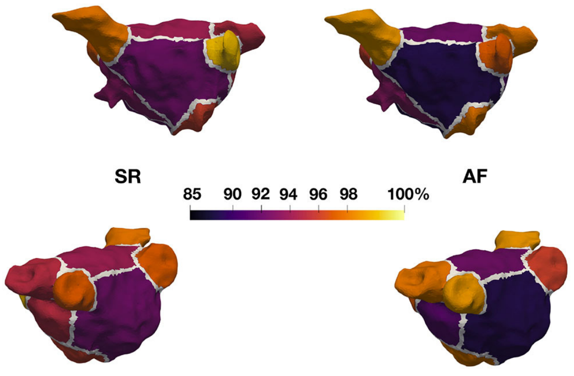

FIGURE 3 | Regional agreement of unipolar and bipolar substrate classification. Eleven anatomical regions were annotated in all 28 patient geometries and analyzed in SR and AF. Each region visualized on this example geometry is colored according to the mean percentage of concordantly categorized mapping sites (unipolar vs. bipolar voltage mapping) with regard to LVA.

TABLE 3 | Mean and standard deviation for the percentage of points that match in different anatomical regions of the LA [bipolar threshold of 0.5 mV in SR and 0.35 mV in AF and the best corresponding unipolar threshold for each patient, which range from 0.62 to 1.1 mV (SR) and 0.45 to 0.99 mV (AF)].

Anatomical region	SR (%)	AF (%)
LIPV	95 ± 6	97 ± 6
LSPV	93 ± 6	96 ± 3
RIPV	96 ± 6	97 ± 4
RSPV	95 ± 6	94 ± 7
MV	94 ± 5	96 ± 6
LAA	98 ± 3	95 ± 7
Anterior wall	90 ± 7	87 ± 8
Posterior wall	90 ± 8	87 ± 10
Lateral wall	93 ± 6	89 ± 7
Roof	92 ± 5	90 ± 7
Septum	91 ± 7	91 ± 7

range of 0.3 mV. However, the similarity between unipolar and bipolar mapping remains high regardless if a common threshold is used or a patient-specific one. This shows that within each patient, a classification margin exists of at most, ± 0.15 mV from the common threshold. Therefore, only a few data points have voltage values within this margin and are affected by changing the threshold in this range.

3.7. Impact of Bipolar Inter-electrode Distance on the Identified Low Voltage Substrate

We analyzed the impact of different inter-electrode distances on bipolar LVA distribution and its correlation to the corresponding unipolar voltage map. Therefore, LA electrograms were analyzed using each bipolar electrode distance (2, 6 mm and both) separately (see **Figure 7**). For both SR and AF, we found that when considering only the small bipoles (2 mm), 3–6% more mapping sites matched than when using the large bipoles (6 mm) or both together. Although the differences in LVA categorization remained small, they are statistically significant. Agreement of LVA categorization using the small bipoles was higher (SR 91%, AF 89% of mapping sites) than for mapping with the large or all bipoles in SR (88 and 87%) and in AF (83 and 85%) ($p < 0.001$ for all cases). The optimal common unipolar threshold for each bipole distance is given in **Table 4**. The unipolar threshold for the all bipoles is slightly higher than reported in **Figure 5** (0.87 vs. 0.83 and 0.64 vs. 0.54 mV). This discrepancy is because this analysis was performed on the electrode signals directly rather than on the interpolated voltage map data. Only a 1% discrepancy in the median percentage of points that matched was seen when using the measured electrograms directly than the interpolated map data.

The best unipolar threshold for bipolar voltage maps (SR <0.5 mV) acquired with the small 2 mm distant electrode pairs was found to be higher (1.09 mV SR and 0.76 mV AF) than when using the large 6 mm distant electrode pairs (0.72 and 0.52 mV). **Supplementary Figure 4** shows the relationship between the bipolar and unipolar threshold when only using 2 mm bipoles (**Supplementary Figure 4A**) and 6 mm (**Supplementary Figure 4B**).

4. DISCUSSION

4.1. Main Findings

The current study on bipolar vs. unipolar voltage mapping reveals three main findings:

1. There is a high correlation in the spatial distribution of uni- and bipolar low voltage areas in sinus rhythm and atrial fibrillation.
2. Over 90% of LA electrograms are concordantly classified as high or low voltage using uni- or bipolar mode independently of the selected bipolar threshold. The remaining discordant electrograms locate to low voltage border zones without change of identified LVA.
3. Bipolar electrode distance has little impact on the agreement between unipolar and bipolar voltage maps.

Previous studies have suggested that diseased tissue can be identified in SR as bipolar voltage areas below 0.5 or 1 mV and similarly for AF with voltages below 0.35 or 0.5 mV (Jadidi et al., 2016; Yang et al., 2016; Rodríguez-Mañero et al., 2018). Our results reveal that for any given bipolar voltage threshold, a universal unipolar voltage threshold can be found that results in a highly similar unipolar voltage map with a spatial distribution of LA LVA that corresponds to the bipolar LVA. For a bipolar threshold of 0.5 mV in SR, a unipolar threshold of 0.83 mV was optimal. In AF, a unipolar threshold of 0.54 mV was found for a bipolar threshold of 0.35 mV. More generally, the unipolar threshold for identifying the same low voltage regions can be obtained by applying a linear transformation to the bipolar threshold being used. This threshold is dependent on the size of the bipolar electrode spacing (**Figure 5**, **Supplementary Figures 4A,B**). The linear regression

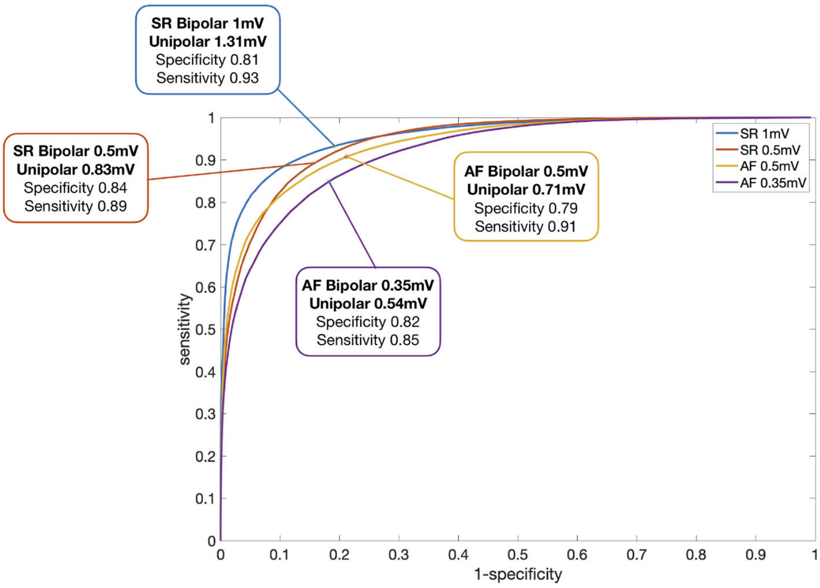

FIGURE 4 | ROC curve regarding identification of LVA for each rhythm and bipolar threshold. Each line represents the sensitivity and specificity for varying unipolar thresholds for the four different bipolar voltage thresholds that are reported in literature for SR and AF. The optimal unipolar thresholds for the corresponding bipolar thresholds were found for each patient and the median value of these patient specific thresholds is given in the figure.

lines describing the relationship differ between SR and AF, where lower unipolar thresholds were identified in AF than in SR. One possible reason for this can be that in AF, the propagation arrives at the electrodes from different directions. Therefore, the lower voltage values due to the catheter orientation are reduced in the bipolar AF map. Since there are fewer low voltage points, a lower unipolar threshold is needed to match the smaller bipolar low voltage areas.

Using patient-individual thresholds increases the agreement between unipolar and bipolar maps by up to 2%. In order to identify the optimal patient-specific unipolar threshold to a pre-selected bipolar threshold in clinical practice, the bipolar and unipolar voltage maps can be visualized side by side and the unipolar threshold can manually be adapted to a level at which the distribution of LVA show the best concordance/correlation to the bipolar voltage map. Our study revealed a very similar distribution of LVA during both mapping modes. Therefore, the utility of a unipolar voltage map beyond the bipolar map has to be assessed in future studies, eventually evaluating these correlations for other mapping catheters.

These high levels of correlation between the unipolar and bipolar map were seen in all four patient subgroups defined by the low voltage substrate extent with only little variation in accuracy of 5% between subgroups. Therefore, regardless of the low voltage substrate extent in a patient, the LVA will be identified in the same locations in both the bipolar and unipolar map.

Previous studies have shown that AF driver sites with acute AF termination frequently occur within LVA in bipolar mapping (Jadidi et al., 2016, 2020). Considering our findings, atrial sites displaying low voltage in the bipolar map will also display these regions in the unipolar map, thus indicating that an important criterion for AF source localization during high-density Lasso mapping is reduced electrogram voltage irrespective of the mapping modality (uni-/bipolar).

4.2. Impact of Electrode Spacing and Atrial Anatomical Region on Voltage Mapping

In this study, we split the voltage information into groups depending on the bipole pair that the signals were obtained from. Small bipolar inter-electrode distance (2 mm) yielded a significantly higher percentage of points being matched correctly in bipolar vs. unipolar voltage mapping, both in SR and AF. When using only the small bipoles, the signal collected from the bipolar pair is more localized, i.e., the region covered by the electrodes is smaller. The signal is less susceptible to influences of far-field, as presented by Takigawa et al. (2019). Therefore, mapping with the small distance electrode pairs improves the correlation between unipolar and bipolar mapping at 4% of mapping sites. Importantly, the optimal unipolar threshold has to be set to a higher value when bipolar mapping is done with small bipoles, resulting in larger LVA than mapping with large bipoles. In contrast, voltage maps acquired with large-spaced bipoles integrate high-voltage far-field signals from adjacent healthier myocardium and therefore, large-spaced bipolar maps under detect low voltage tissue. The unipolar voltage map, therefore, has to be set to a lower threshold to display the smaller LVA of the large-spaced bipolar map.

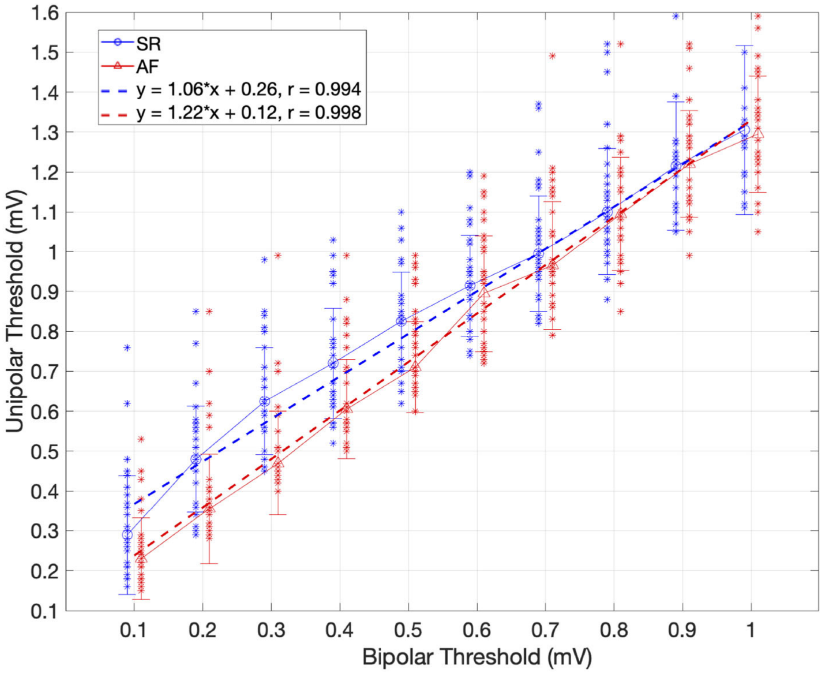

FIGURE 5 | Relationship between the bipolar and unipolar threshold in SR (blue) and AF (red). The unipolar threshold with highest concordance to the bipolar map is shown for different bipolar thresholds and each individual patient (blue and red dots for SR and AF, respectively). Standard deviation is represented by bars. The optimal unipolar threshold is identified as the optimal point on the ROC curve of each bipolar threshold using all patients. Linear regression shown as dotted lines, depending on the rhythm (SR blue, AF red). Pearson correlation coefficient (r) is provided. For every unipolar threshold, >89% of points matched in SR and >86% in AF.

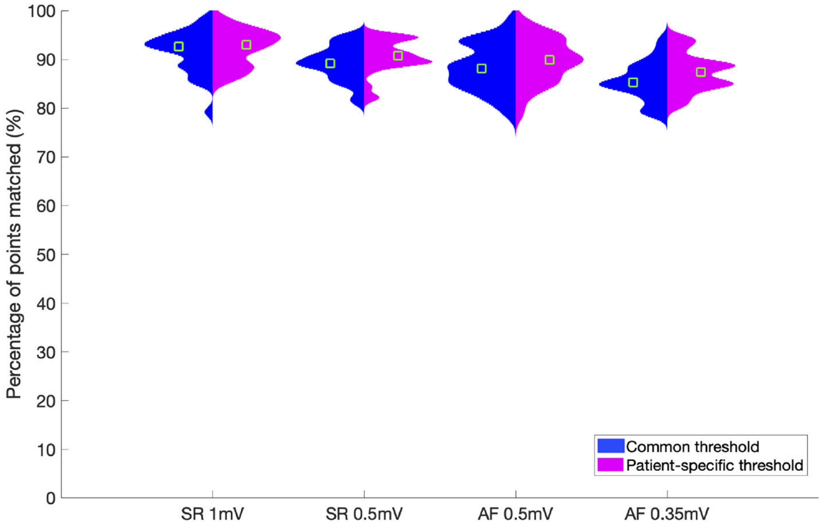

FIGURE 6 | Violin plot showing the percentage of points which match between unipolar and bipolar classification. The results are shown for each rhythm and corresponding bipolar threshold over all patients. Results for a common unipolar threshold for all patients are shown in blue. Results for patient-individual unipolar thresholds are shown in pink. The green squares indicate the median value for each set.

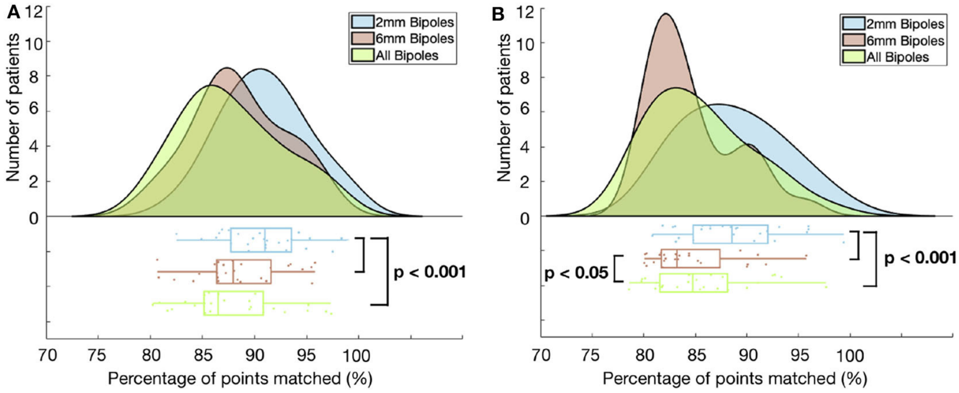

FIGURE 7 | Histogram and corresponding boxplot showing the percentage of points matched in SR **(A)** and AF **(B)** for each of the three electrode distance categories. Each category is shown in a different color: 2 mm (blue), 6 mm (red), all (green). *p*-value calculated with paired-sample *t*-test.

TABLE 4 | Rhythm-specific unipolar threshold corresponding to each bipolar threshold for each group of bipolar electrode distance.

	SR Threshold (mV)		AF Threshold (mV)	
Distance (mm)	**Bipolar**	**Unipolar**	**Bipolar**	**Unipolar**
2	0.5	1.09	0.35	0.76
6	0.5	0.72	0.35	0.52
All	0.5	0.87	0.35	0.64

Recent studies revealed a preferential anatomical distribution of LA LVA that more frequently affects the LA antero-septal area, followed by the LA roof and LA posterior wall (Corradi et al., 2005; Marcus et al., 2007; Müller-Edenborn et al., 2019). Therefore, it is more likely that LVA are present in these regions. From our analysis of assessing the different LA regions separately, we see that some of the lowest similarity between bipolar and unipolar signals exist in the posterior wall (90% SR, 87% AF match), the anterior wall (90% SR, 87% AF), and the septum (91% SR, 91% AF). This finding can be explained by the higher rate of occurrence of LVA in these regions, as this also means that more border zones are present and mismatch between unipolar and bipolar classification mainly occurred in border zones (**Figure 1**). In other areas such as the pulmonary veins, we typically have low voltage across the entire region and, therefore, fewer border zones, which leads to less mismatch in these regions.

4.3. Possible Reasons for the High Similarity Between Unipolar and Bipolar Low Voltage Distribution Patterns

Our findings show a high agreement between the bipolar and unipolar mapping when using high-density multi-electrode mapping with a 20-pole Lasso catheter. However, from simulation studies, it is known that the angle of the bipolar electrode pair in relation to the propagation direction and the size and distance between the electrodes are known to affect the bipolar voltage amplitude (Schuler et al., 2013; Beheshti et al., 2018). A recent study has shown that for 2 and 6 mm distant electrodes in simulated and clinical data, the amplitude of the bipolar electrogram goes from a maximum value at 0° to the propagation of a planar wavefront to close to 0 mV at 90° (Gaeta et al., 2019). Therefore, one can hypothesize that the bipolar voltage map would not present the same information as the unipolar voltage due to the direction dependence. Despite these factors, in our study, the majority of points (90%) were consistently categorized as either low or high voltage in both unipolar and bipolar. Small differences, which are clinically irrelevant, only exist at the border zones of the low voltage to high voltage threshold. Therefore, it is crucial to understand why the majority of points on the map have the same classification in both maps when the bipolar electrograms are influenced by various factors of the catheter. Here we discuss potential reasons why the theory-based expectations about the effects of using a bipolar catheter are hardly met by what was empirically identified in this study.

The simulation studies show that when the electrode orientation is perpendicular to the propagation, the bipolar voltage is 0 mV. This situation is shown in **Figure 2** by the electrograms marked with a triangle. However, the high overall correlation between the high-density unipolar vs. bipolar maps indicates that this situation rarely occurs in practice. One explanation may be the following: In the clinical setting of the 1–5 mm thick atrial wall with multiple layers of myocardial fibers, it may be extremely rare that the wavefront is uniformly parallel to the mapping bipole. Instead, the waves always contain some degree of curvature in the three-dimensional space, so that the electrodes do not receive the signal at the same time point, which would result in a voltage >0 mV. Thus, the effect of the bipolar orientation is likely to be less pronounced in clinical mapping settings than what is presented in idealized simulations with homogeneous tissue and (almost) perfectly planar wavefronts.

Another possible explanation for obtaining such a high correlation is due to the maps containing a high density of points. Thus, points in close proximity can be obtained from the catheter at various bipole orientations. Therefore, when interpolation of voltages is applied in the electro-anatomical maps, areas with low and high voltage points caused by the orientation of the catheter may result in an averaged value. Thus, some points which are affected by the catheter orientation may cancel out by near-by adjacent mapping points with different orientations to the wavefront. The use of interpolated vs. non-interpolated voltage maps yielded similar levels of agreement, suggesting that this effect does not notably contribute. During ongoing AF with changing wavefront directions, the direction dependency of the bipolar voltage maps should be further reduced (in comparison to regular rhythms).

Additionally, if the unipolar voltages at points in the diseased tissue are much smaller than the threshold or much larger than the threshold in healthy regions, then there is a substantial classification margin. This would result in the distortion of the bipolar voltages due to the unknown orientation of electrodes to still be within this margin and the classification to be the same for the bipolar and unipolar map. For the points in which the voltages are close to the threshold values, the classification is more susceptible to changes in the voltage due to the orientation or the distance between the electrodes. Furthermore, if the two electrodes used to calculate the bipolar voltage have slightly different distances to the endocardium, the bipolar voltage would be reduced. However, for unipolar voltages with a large amplitude, then this difference would cause the bipolar voltage to be reduced but not substantial enough to cause the value to fall below the threshold. In **Figure 1**, the bipolar voltage maps show more patchy/irregular areas than the unipolar map. This shows that the bipolar map may be affected by factors such as wavefront-to-bipole orientation in these areas. However, most regions are far enough from the threshold for the orientation of the catheter to affect the classification.

Finally, the unipolar threshold was identified to provide the best correlation between the unipolar and the bipolar map based on the standard bipolar threshold used in practice. This, however, may not lead to the best unipolar threshold for identifying true areas of fibrotic tissue. Future investigations will help to unravel which of the aforementioned potential reasons contribute most to the agreement between both mapping modalities. Nevertheless, this study has shown that with appropriate settings and the identical catheter, the same LVA can be identified when using the bipolar or unipolar map.

5. LIMITATIONS

In this study, CARTO-3 was used for electro-anatomic voltage mapping, with a Lasso catheter of 2 and 6 mm inter-electrode spacing. Since only one type of catheter was used, it may be that our results are not applicable when using other catheters or mapping systems. However, we expect similar results with high-density maps acquired using a PentaRay or OctaRay catheter, where the mapping conditions such as electrode size, inter-electrode distance, and the parallel orientation of bipoles to endocardium are similar as in the current mapping study. We aimed at having high-density maps with a sufficient number of data points across the entire atria. For some patients, more points were taken at specific areas of interest; therefore, the distribution of points was not always equal between patients. However, it was ensured that the mapping density was sufficiently high (17 and 22 mapping sites per cm^2 for SR and AF maps, respectively) to allow for regional analysis of the voltage maps. In this work, only one atrial beat was considered per mapped LA site (without averaging of multiple consecutive beats). However, due to the high density of the acquired maps, the atrial tissue was characterized by numerous mapping points that were recorded within a short distance from each other and contributed to the final voltage distribution maps in CARTO-3.

6. CONCLUSION

Bipolar and unipolar voltage maps are highly correlated both in SR and AF. Both mapping modes identify the same atrial sites as low voltage substrate. Small differences in low voltage classification may occur at the border zone of low voltage areas, without relevant impact on their spatial distribution patterns. Voltage mapping using small (2 mm) bipoles slightly improves the agreement between unipolar and bipolar low voltage areas. While bipole orientation and inter-electrode spacing are theoretical confounders, their impact is not of clinical importance, when mapping is performed at high density with a 20-polar Lasso catheter.

DATA AVAILABILITY STATEMENT

The data analyzed in this study is subject to the following licenses/restrictions: To protect the safety of the patients, the data used for this study can not be provided. However, the figures within the article and **Supplementary Material** show detailed analyses for all patients used. Requests to access these datasets should be directed to: Deborah Nairn, deborah.nairn@kit.edu.

ETHICS STATEMENT

The studies involving human participants were reviewed and approved by University Hospital of Freiburg Ethics Committee. The patients provided their written informed consent to participate in this study.

AUTHOR CONTRIBUTIONS

DN, HL, AJ, and AL designed the study and analyzed the results. HL and AJ collected the data. SS developed the automatic tool for sectioning the atria. DN carried out the data analysis and produced the initial draft of the manuscript. All authors critically revised the manuscript and approved the final submitted manuscript.

FUNDING

We gratefully acknowledge financial support by Deutsche Forschungsgemeinschaft (DFG) through DO637/22-3 and by the Ministerium für Wissenschaft, Forschung und Kunst Baden-Württemberg through the Research Seed Capital (RiSC) program. We acknowledge support by the KIT-Publication Fund of the Karlsruhe Institute of Technology.

SUPPLEMENTARY MATERIAL

The Supplementary Material for this article can be found online at: https://www.frontiersin.org/articles/10.3389/fphys.2020.575846/full#supplementary-material

REFERENCES

Anter, E., Tschabrunn, C. M., and Josephson, M. E. (2015). High-resolution mapping of scar-related atrial arrhythmias using smaller electrodes with closer interelectrode spacing. *Circ. Arrhyth. Electrophysiol.* 8, 537–545. doi: 10.1161/CIRCEP.114.002737

Beheshti, M., Magtibay, K., Massé, S., Porta-Sanchez, A., Haldar, S., Bhaskaran, A., et al. (2018). Determinants of atrial bipolar voltage: Inter electrode distance and wavefront angle. *Comput. Biol. Med.* 102, 449–457. doi: 10.1016/j.compbiomed.2018.07.011

Blandino, A., Bianchi, F., Grossi, S., Biondi-Zoccai, G., Conte, M. R., Gaido, L., et al. (2017). Left atrial substrate modification targeting low-voltage areas for catheter ablation of atrial fibrillation: a systematic review and meta-analysis. *Pacing Clin. Electrophysiol.* 40, 199–212. doi: 10.1111/pace.13015

Corradi, D., Callegari, S., Benussi, S., Maestri, R., Pastori, P., Nascimbene, S., et al. (2005). Myocyte changes and their left atrial distribution in patients with chronic atrial fibrillation related to mitral valve disease. *Hum. Pathol.* 36, 1080–1089. doi: 10.1016/j.humpath.2005.07.018

Frisch, D., Oesterlein, T. G., Unger, L. A., Lenis, G., Wakili, R., Schmitt, C., et al. (2020). Mapping and removing the ventricular far field component in unipolar atrial electrograms. *IEEE Trans. Biomed. Eng.* 67, 2905–2915. doi: 10.1109/TBME.2020.2973471

Gaeta, S., Bahnson, T. D., and Henriquez, C. (2019). Mechanism and magnitude of bipolar electrogram directional sensitivity: characterizing underlying determinants of bipolar amplitude. *Heart Rhythm* 17(5 Pt A), 777–785. doi: 10.1016/j.hrthm.2019.12.010

Go, A. S., Mozaffarian, D., Roger, V. L., Benjamin, E. J., Berry, J. D., Blaha, M. J., et al. (2014). Heart disease and stroke statistics-2014 update: a report from the American heart association. *Circulation* 129, e28–e292. doi: 10.1161/01.cir.0000441139.02102.80

Haissaguerre, M., Jaïs, P., Shah, D. C., Takahashi, A., Hocini, M., Quiniou, G., et al. (1998). Spontaneous initiation of atrial fibrillation by ectopic beats originating in the pulmonary veins. *N. Engl. J. Med.* 339, 659–666. doi: 10.1056/NEJM199809033391003

Jadidi, A., Nothstein, M., Chen, J., Lehrmann, H., Dössel, O., Allgeier, J., et al. (2020). Specific electrogram characteristics identify the extra-pulmonary vein arrhythmogenic sources of persistent atrial fibrillation-characterization of the arrhythmogenic electrogram patterns during atrial fibrillation and sinus rhythm. *Sci. Rep.* 10:9147. doi: 10.1038/s41598-020-65564-2

Jadidi, A. S., Lehrmann, H., Keyl, C., Sorrel, J., Markstein, V., Minners, J., et al. (2016). Ablation of persistent atrial fibrillation targeting low-voltage areas with selective activation characteristics. *Circ. Arrhyth. Electrophysiol.* 9:e002962. doi: 10.1161/CIRCEP.115.002962

Lin, C.-Y., Te, A. L. D., Lin, Y.-J., Chang, S.-L., Lo, L.-W., Hu, Y.-F., et al. (2018). High-resolution mapping of pulmonary vein potentials improved the successful pulmonary vein isolation using small electrodes and inter-electrode spacing catheter. *Int. J. Cardiol.* 272, 90–96. doi: 10.1016/j.ijcard.2018.06.062

Marcus, G. M., Yang, Y., Varosy, P. D., Ordovas, K., Tseng, Z. H., Badhwar, N., et al. (2007). Regional left atrial voltage in patients with atrial fibrillation. *Heart Rhythm* 4, 138–144. doi: 10.1016/j.hrthm.2006.10.017

Miyasaka, Y., Barnes, M. E., Gersh, B. J., Cha, S. S., Seward, J. B., Bailey, K. R., et al. (2005). Time trends of ischemic stroke incidence and mortality in patients diagnosed with first atrial fibrillation in 1980 to 2000: report of a community-based study. *Stroke* 36, 2362–2366. doi: 10.1161/01.STR.0000185927.63746.23

Mori, H., Kato, R., Ikeda, Y., Goto, K., Tanaka, S., Asano, S., et al. (2018). The influence of the electrodes spacing of a mapping catheter on the atrial voltage substrate map. *J. Cardiol.* 72, 434–442. doi: 10.1016/j.jjcc.2018.04.012

Müller-Edenborn, B., Chen, J., Allgeier, J., Didenko, M., Moreno-Weidmann, Z., Neumann, F.-J., et al. (2019). Amplified sinus-p-wave reveals localization and extent of left atrial low-voltage substrate: implications for arrhythmia freedom following pulmonary vein isolation. *Europace* 22, 240–249. doi: 10.1093/europace/euz297

Oakes, R. S., Badger, T. J., Kholmovski, E. G., Akoum, N., Burgon, N. S., Fish, E. N., et al. (2009). Detection and quantification of left atrial structural remodeling with delayed-enhancement magnetic resonance imaging in patients with atrial fibrillation. *Circulation* 119, 1758–1767. doi: 10.1161/CIRCULATIONAHA.108.811877

Rodríguez-Mañero, M., Valderrábano, M., Baluja, A., Kreidieh, O., Martínez-Sande, J. L., Garc-Seara, J., et al. (2018). Validating left atrial low voltage areas during atrial fibrillation and atrial flutter using multielectrode automated electroanatomic mapping. *JACC Clin. Electrophysiol.* 4, 1541–1552. doi: 10.1016/j.jacep.2018.08.015

Rolf, S., Kircher, S., Arya, A., Eitel, C., Sommer, P., Richter, S., et al. (2014). Tailored atrial substrate modification based on low-voltage areas in catheter ablation of atrial fibrillation. *Circ. Arrhythm. Electrophysiol.* 7, 825–833. doi: 10.1161/CIRCEP.113.001251

Schuler, S., Keller, M. W., Oesterlein, T., Seemann, G., and Dössel, O. (2013). "Influence of catheter orientation, tissue thickness and conduction velocity on the intracardiac electrogram," in *Biomedical Engineering/Biomedizinische Technik, Vol. 58* (Berlin: De Gruvter). Available online at: https://www.degruyter.com/view/journals/bmte/bmte-overview.xml?tab_body=editorialContent-78027

Seitz, J., Bars, C., Théodore, G., Beurtheret, S., Lellouche, N., Bremondy, M., et al. (2017). AF ablation guided by spatiotemporal electrogram dispersion without pulmonary vein isolation: a wholly patient-tailored approach. *J. Am. Coll. Cardiol.* 69, 303–321. doi: 10.1016/j.jacc.2016.10.065

Takigawa, M., Relan, J., Martin, R., Kim, S., Kitamura, T., Cheniti, G., et al. (2019). Detailed analysis of the relation between bipolar electrode spacing and far- and near-field electrograms. *JACC Clin. Electrophysiol.* 5, 66–77. doi: 10.1016/j.jacep.2018.08.022

Verma, A., Jiang, C.-Y., Betts, T. R., Chen, J., Deisenhofer, I., Mantovan, R., et al. (2015). Approaches to catheter ablation for persistent atrial fibrillation. *N. Engl. J. Med.* 372, 1812–1822. doi: 10.1056/NEJMoa1408288

Verma, A., Wazni, O. M., Marrouche, N. F., Martin, D. O., Kilicaslan, F., Minor, S., et al. (2005). Pre-existent left atrial scarring in patients undergoing pulmonary vein antrum isolation: an independent predictor of procedural failure. *J. Am. Coll. Cardiol.* 45, 285–292. doi: 10.1016/j.jacc.2004.10.035

Wang, T. J., Larson, M. G., Levy, D., Vasan, R. S., Leip, E. P., Wolf, P. A., et al. (2003). Temporal relations of atrial fibrillation and congestive heart failure and their joint influence on mortality: the Framingham heart study. *Circulation* 107, 2920–2925. doi: 10.1161/01.CIR.0000072767.89944.6E

Yamaguchi, T., Tsuchiya, T., Fukui, A., Kawano, Y., Otsubo, T., Takahashi, Y., et al. (2018). Impact of the extent of low-voltage zone on outcomes after voltage-based catheter ablation for persistent atrial fibrillation. *J. Cardiol*. 72, 427–433. doi: 10.1016/j.jjcc.2018.04.010

Yang, G., Yang, B., Wei, Y., Zhang, F., Ju, W., Chen, H., et al. (2016). Catheter ablation of nonparoxysmal atrial fibrillation using electrophysiologically guided substrate modification during sinus rhythm after pulmonary vein isolation. *Circ. Arrhythm. Electrophysiol*. 9:e003382. doi: 10.1161/CIRCEP.115.003382

Conflict of Interest: The authors declare that the research was conducted in the absence of any commercial or financial relationships that could be construed as a potential conflict of interest.

Copyright © 2020 Nairn, Lehrmann, Müller-Edenborn, Schuler, Arentz, Dössel, Jadidi and Loewe. This is an open-access article distributed under the terms of the Creative Commons Attribution License (CC BY). The use, distribution or reproduction in other forums is permitted, provided the original author(s) and the copyright owner(s) are credited and that the original publication in this journal is cited, in accordance with accepted academic practice. No use, distribution or reproduction is permitted which does not comply with these terms.

4.2 Effect of the Atrial Geometry

This section contains work carried out during a master thesis [82]. During this work, 3D models of the left atria containing a deformed catheter to represent the situation in the clinical practice were created. Simulations were then performed, and algorithms were developed to obtain the unipolar and bipolar signals. The peak-to-peak values and the local activation times were then calculated. Using these parameters, the effect of the atrial geometry on the electrogram signals could be analysed. During the masters thesis, only electrode pairs with a 2 mm distance between them were included. For this thesis, the signals from the 6 mm distance between electrode pairs were included to further understand the electrode distance's impact and better relate the results to the clinical practice.

4.2.1 Methods

A 3D left atrial geometry created from a CT scan of a patient was used in this study [83]. A realistic 7F 20-pole lasso catheter geometry (Biosense Webster, Diamond Bar, CA, USA) with electrode size: 1 mm and spacing: 2–6–2 mm was then placed within the atrium. The catheter was placed with a realistic deformation on three different locations within the atrium: the anterior wall, posterior wall and roof. Following, the atrium was surrounded by a convex hull representing the blood. The simulation setup can be seen in figure 4.1A.

Bidomain simulations were then performed using openCARP [84, 85]. An intracellular stimulus of 40 μm/cm^2 was applied to an area at either the Bachmann's bundle (BB) or the coronary sinus (CS) of the left atrium. The blood bath was modeled with a conductivity of 0.625 S/m. The myocardial intracellular and extracellular conductivity was set to 0.264 S/m and 0.40 S/m, respectively, to achieve a conduction velocity of 43.6 cm/s [86, 87]. The electrodes were then modeled as a highly conductive isopotential material with a conductivity of $1x10^6$ S/m. Figure 4.1B shows an example of the wavefront coming from the Bachmann's bundle with the catheter located in the roof.

The unipolar signals acquired were then subtracted to obtain the bipolar signals. The peak-to-peak amplitude was taken as the voltage for each signal and the maximum downslope of the unipolar signal was used to determine the local activation time.

4.2.2 Results

Table 4.1 shows that across all simulations the bipolar voltages can greatly vary from close to 0 mV up to 10 mV. If the wavefront arrives at the same time to both electrodes in one pair (difference in activation time is zero), the voltage drops to close to zero, as seen by table 4.1 and figure 4.2. For each simulation or catheter position, the bipolar voltages drop below a cut-off value of 0.5 mV in either one or two bipolar pairs and in one case, even three times. If 0.5 mV is used to differentiate health from unhealthy tissue, the results would imply that

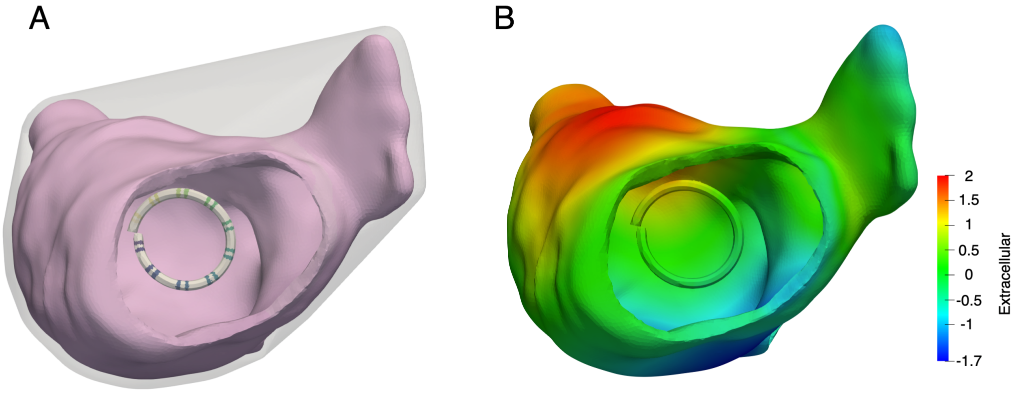

Figure 4.1: Illustrate of simulation setup with the blood shown in grey, the atrial geometry in pink and the lasso catheter placed on the roof in white. Example of simulation of wavefront coming from the Bachmann's bundle with the catheter located in the roof.

around 2 out of 19 bipolar pairs (5-11% of pairs) would be incorrect only due to the angle of the catheter causing the wavefront to reach two electrodes at the same time.

Table 4.1: Table showing the difference in activation time (ΔAT) and bipolar voltages (V) for each of the six simulations for all bipolar pairs. Electrode pairs where the bipolar voltage drops below a cut-off value of 0.5 mV are indicated in yellow.

	Anterior				Posterior				Roof			
	BB		CS		BB		CS		BB		CS	
	ΔAT (ms)	V (mV)	ΔAT (ms)	V (mV)	ΔAT (ms)	V (mV)	ΔAT (ms)	V (mV)	ΔAT (ms)	V (mV)	ΔAT (ms)	V (mV)
Pair 1-2	1.00	4.20	-2.00	3.59	-1.67	4.89	-1.00	6.26	0.00	0.27	0.00	0.14
Pair 2-3	6.67	7.90	-1.67	3.88	-9.00	8.53	2.00	9.34	-11.67	8.01	4.00	6.58
Pair 3-4	2.33	2.27	1.67	3.03	-2.67	7.45	1.67	8.94	-2.00	3.84	2.00	1.92
Pair 4-5	1.67	2.96	0.67	2.12	-7.00	7.82	6.00	9.63	1.67	3.01	-1.00	2.56
Pair 5-6	0.00	0.02	0.00	0.36	0.00	0.21	0.33	1.08	2.67	5.06	-3.00	6.49
Pair 6-7	-0.67	0.97	-7.00	5.06	-1.33	1.99	10.33	8.26	11.33	9.12	-9.67	8.09
Pair 7-8	0.00	0.03	0.00	0.05	0.33	0.73	2.33	3.13	2.67	7.30	-1.33	1.98
Pair 8-9	-0.67	1.06	-0.67	1.53	-0.67	1.33	7.33	6.50	11.00	7.74	2.67	1.77
Pair 9-10	-1.33	1.40	1.33	2.61	1.67	1.50	1.00	1.82	0.00	0.13	0.00	0.11
Pair 10-11	-5.67	7.19	7.33	8.96	3.67	7.34	2.33	4.14	13.67	5.08	-10.33	6.29
Pair 11-12	-2.00	4.18	3.67	6.96	3.00	5.54	1.67	0.88	0.00	0.40	-0.67	1.05
Pair 12-13	-11.33	8.15	9.67	8.66	9.67	8.67	-1.33	1.33	1.00	4.29	-11.33	9.25
Pair 13-14	-4.33	4.76	3.33	5.34	3.67	6.20	1.00	0.60	3.00	1.16	-2.00	6.31
Pair 14-15	-10.00	7.27	10.33	7.12	8.00	6.98	-2.33	1.99	-5.33	5.10	-4.33	7.04
Pair 15-16	-2.67	2.23	3.00	2.49	1.67	3.05	0.00	0.43	-1.00	2.50	1.00	1.11
Pair 16-17	4.67	6.68	-4.33	5.54	7.33	9.19	-2.00	3.16	-4.67	7.75	6.33	8.01
Pair 17-18	3.33	6.46	-2.33	5.28	2.67	9.25	-2.33	3.59	-2.67	3.59	3.00	5.73
Pair 18-19	8.33	9.53	-9.67	9.16	-8.67	9.84	-8.33	8.31	-6.67	6.31	11.00	6.69
Pair 19-20	3.00	7.19	-3.00	7.53	-3.67	6.91	-5.33	5.80	-3.33	2.28	3.33	2.69

From figure 4.2, a quadratic relationship ($y = -0.11x^2 + 1.82x + 0.51$) can be seen between the absolute difference of activation times arriving at the electrodes and the bipolar amplitude. The R^2 value was found to be 0.71. Therefore, 71% of the variation in the bipolar voltage is attributable to the difference in activation times.

By examining the bipolar voltage further in relation to the distance between the electrodes, as seen in figure 4.3, the bipolar voltage only drops close to 0 for distances of 2 mm between electrodes. However, for the majority of electrode pairs the bipolar voltages are only slightly

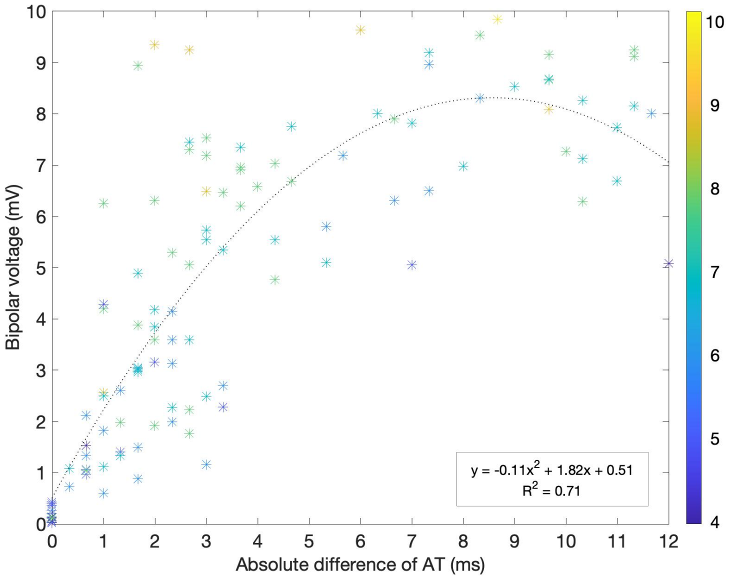

Figure 4.2: Scatter plot showing the relationship between bipolar voltage and the absolute difference of activation time. The points are shown for all simulations with each colour representing the unipolar voltages.

lower than the unipolar voltages. On the other hand, distances of 6 mm between the electrodes can cause the voltage to be even higher than the unipolar voltages.

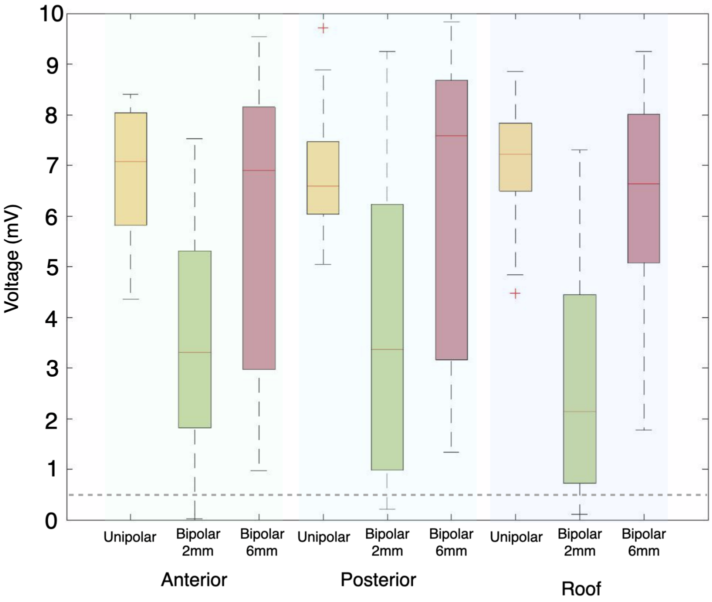

Figure 4.3: Boxplot showing the unipolar and bipolar voltages for different distances between electrodes. The dotted line represents the cut-off value 0.5 mV.

4.2.3 Discussion

The previous study revealed a high correlation between bipolar and unipolar voltage mapping for identifying low voltage areas [80]. One hypothesis for the high correlation despite the known influence of the catheter angle on the bipolar voltage is that the waves always contain some degree of curvature in the three-dimensional space, leading to the wavefront arriving at two electrodes simultaneously unlikely. In this study, where the curvature of the atria was included, it was identified that although the bipolar voltage does not go to 0 mV it sometimes drops below 0.5 mV, a well-established cut-off value for determining low voltage areas.

In the clinical setting, the agreement between the bipolar and unipolar maps in SR was 90 ± 5%. Therefore, 5-10% of the points across the atrium were falsely classified. The simulations with healthy tissue identified that 5-11% of the bipolar pairs would drop below 0.5 mV and be falsely classified as unhealthy tissue. Therefore, one could conclude that the influence of the catheter angle is very much present in the bipolar voltages in the clinical setting. Since the catheter is often rotated while moving within the atrium, these points of false low voltage due to the catheter angle would be more likely spread sporadically across the atrium and unlikely identified as a single region to be ablated.

A quadratic relationship was found between the difference of activation times and the bipolar voltages. When the wavefront hits the two electrodes simultaneously, the unipolar signals will be close to identical. Therefore, the subtraction of the two will reduce the bipolar amplitude. As the difference in activation time increases, the bipolar voltage will increase until it reaches the maximum. This appears to be when there is around an 8 ms difference in the activation time. After, the bipolar voltage decreases again until the two unipolar signals are not aligned and the bipolar voltage equals the unipolar voltage. By obtaining an R^2 of 0.71, it is clear that the activation time plays an essential role in the variation of the bipolar voltages. However, this is not the only factor. One other effect can be the distance of the electrodes to the tissue, specifically, if one of the electrodes is in contact with the tissue while the other is not. Then although the wavefront arrives at a similar time to both electrodes, the amplitude in one electrode would be smaller, resulting in a non-zero bipolar amplitude.

The simulations identified that the wavefront reaching both electrodes in one pair almost simultaneously only occurs when the electrodes have a small distance between them (2 mm). For these close electrode distances, the difference in activation time is relatively small regardless of the angle, causing the bipolar voltages to be typically lower than the unipolar values. Therefore, if the unipolar voltage is only slightly greater than the threshold, a similar activation time between the two electrodes could cause the bipolar voltage to drop just below the threshold. Alternatively, with greater distances between the electrodes (6 mm), the bipolar voltage can be bigger than the unipolar voltages. If the unipolar voltage is slightly below the cut-off value, the bipolar value may end up above the threshold. This would explain why most of the differences between unipolar and bipolar voltage mapping are contained to the border zones between the high and low voltage areas, as identified in Nairn et al. [80]. Although this could cause the area of low voltage to be slightly bigger or smaller than the area of pathological substrate, the specific region identified to be ablated remains the same between mapping modalities. Therefore, one can perform bipolar voltage mapping with the confidence that the catheter angle does not play a significant role in distorting the bipolar voltage values. However, perhaps caution in the diameter of the ablation area should be taken.

4.3 Impact of the Electrode Size

Impact of Electrode Size on Electrogram Voltage in Healthy and Diseased Tissue

Deborah Nairn, Daniel Hunyar, Jorge Sánchez, Olaf Dössel, Axel Loewe

Institute of Biomedical Engineering, Karlsruhe Institute of Technology (KIT), Karlsruhe, Germany

Abstract

Atrial fibrillation can be treated using low voltage (LV) (amplitude of intracardiac electrogram $<$ 0.5mV) targeted ablation. However, catheter characteristics can alter the voltage leading to changes in identified LV areas. This study evaluates the impact electrode size has on the voltage in healthy and diseased tissue. A realistic setup was generated of tissue, bath and two high conductivity electrodes, with centre to centre spacing of 2mm, placed in contact to the tissue and perpendicular to the planar wavefront. Simulations were performed varying the dimensions of the cubic electrodes from 0.2 to 1.6 mm in healthy tissue and including fibrosis in different locations. An inverse relationship was found between the electrode size and the voltage. When including epicardial fibrosis, a voltage decrease of 1 mV was found in electrodes. When fibrosis was placed closer to the electrodes, a morphological signal change was seen and a 9 mV drop in voltage for small electrodes. Large electrodes deliver smaller voltages. A fibrotic area on the epicardial side has a small influence on the voltage, which was not amplified by increasing electrode size. Endocardial fibrosis delivers significantly smaller voltages than healthy tissue. Little difference in the voltage was seen between large electrodes ($>$1 mm) in diseased tissue. Electrode size needs to be accounted for when determining LV areas using different catheters.

1. Introduction

Atrial fibrillation is the most common cardiac arrhythmia, characterised by an irregular, rapid heart rate, which can lead to stroke, heart failure and other complications [1]. One technique used to treat the arrhythmia is performing electroanatomical mapping, specifically targeting areas of low voltage (LV) (amplitude of the bipolar intracardiac electrogram $<$ 0.5 mV) for ablation [2, 3]. This is a commonly used and important technique, however, the method has limitations as characteristics of the catheter can alter the voltage and lead to changes in identified LV areas.

In order to further understand the effects the catheter has on the voltage, previous studies have performed in-silico experiments evaluating the impact of the catheter angle, inter-electrode spacing and the thickness of the tissue [4, 5]. Anter et al. looked into the effect of two different sizes of electrodes (3.5 mm and 1 mm) and identified that areas of LV and scar were enhanced with small electrodes [6]. Additionally, the effect of the electrode size on the spatial resolution was examined and found that changes in the electrode height had the greatest impact [7]. From these studies, it can be seen that the electrode size can have a significant impact on the identification of LV areas. Therefore, it is important to quantify and study the effect further and assess if it is possible to account for the electrode size when identifying LV areas.

In this study, the relationship between the electrode size and the bipolar and unipolar voltage were assessed. The simulations were performed in healthy tissue and diseased tissues, which allowed for an extensive overview of the impact the electrode size has and what measures should be considered in the clinical practice to prevent false LV areas being identified due to characteristics of the catheter used.

2. Methods

In this study, meshes were generated to reproduce a realistic setup of tissue, bath and electrodes. The patch of atrial tissue was comprised of tetrahedral elements with a mean average length of 0.2 mm, and the human atrial cell model by Courtemanche et al. [8] was used. The tissue had dimensions 60x30x2 mm for all simulations, as shown in figure 1. Additionally, in figure 1, the bath can be seen, indicated by the black outline. The dimensions of the bath were chosen as 68x30x10 mm to exceed the tissue in the length and height and to be the same width as the tissue to reproduce the bath load effect on the propagation of the wave. Two highly conductive electrodes were added to the setup, both in contact to the tissue with a centre to centre distance of 2 mm from each other for all simulations (shown as grey cubes in figure 1).

Page 1 ISSN: 2325-887X DOI: 10.22489/CinC.2020.146

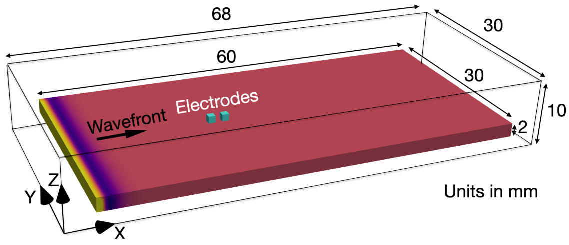

Figure 1: Diagram of the atrial tissue (in red) shown with the surrounding bath (black outline) and two cube electrodes (in grey) placed on the surface and in contact to the tissue. The wave direction within the tissue is from left to right (the yellow region indicates the start of the wavefront).

To allow for interactions between the intra and extracellular space and account for the effects of the electrodes, bidomain simulations were performed. An intracellular stimulus of 50 mA was applied for 2 ms to the left hand side of the tissue (yellow region in figure 1). The direction of the wavefront, additionally indicated in the figure, is defined as a planar wavefront perpendicular to the electrodes. The myocardial intracellular conductivity was set to 0.36 S/m and extracellular to 1.29 S/m to achieve a realistic conduction velocity of 0.71 m/s [9]. The bath was modelled with a conductivity of 0.63 S/m to represent human blood [10]. The conductivity of the electrodes was set as 700 S/m to simulate a highly conductive element.

The first batch of simulations were then performed changing the length, width and/or height of the electrode. The initial size of the electrodes were set to 1 mm^3 and then one or more dimensions were increased or decreased in steps of 0.2 mm. The electrodes were changed from 0.2-1.6 mm in four ways: (1) changing all dimensions of the electrode (x,y,z), (2) changing the height (z), (3) changing the width and height (y,z) and (4) changing the length and width (x,y). The dimensions of the electrodes were chosen to represent a range of electrode sizes that are currently being used in the clinical practice [11].

In the next batch of simulations, the electrode size was again changed in all dimensions (x,y,z) from 0.2 mm^3 to 1.6 mm^3. However, in this case, a patch of fibrotic tissue was included in three locations on the z-axis: on the epicardial side of the tissue, in the middle of the tissue and on the endocardial side. The fibrotic patch was represented by non-conductive mesh elements, that represent collagen fibres, with a length of 0.3mm and a diameter of 0.1mm randomly placed inside an ellipsoid region located in the centre of the patch (x,y), which followed the fibre direction of the tissue.

3. Results

3.1. Electrode Size in Healthy Tissue

When changing the size of the electrode in all dimensions (x,y,z) in healthy tissue, it was found that the voltage decreases as the electrode size increases. In figure 2 the bipolar and unipolar signals are shown for each size of electrode. It can be seen that there is little change to the morphology of the signal, but the amplitude of the signal decreases as the size increases. Additionally, in figure 2, a closer look into the relationship between the voltage and changing all the electrode dimensions can be seen. For smaller electrodes (0.2-0.8 mm^3), the line of best fit has a steeper gradient, voltage = -9.4*size+13.1 for bipolar compared to voltage = -4.4*size+9.1 for electrodes of size >= 0.8 mm^3.

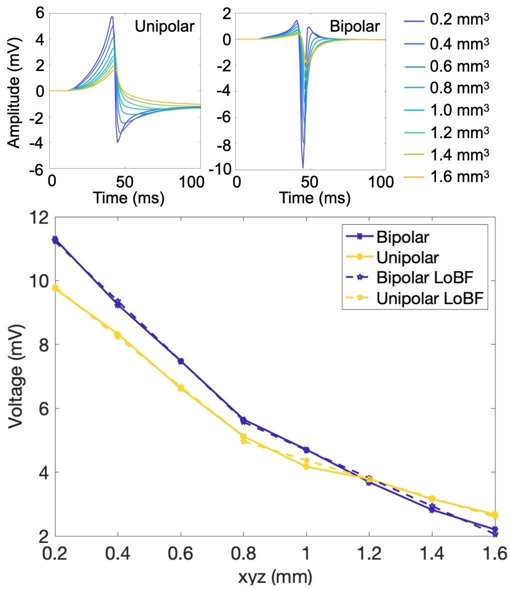

Figure 2: The top figure shows the unipolar electrograms from the electrode closest to the wavefront and the bipolar electrograms. Each colour represents one size of the electrode in mm^3. The bottom row shows the voltage for different electrode sizes, bipolar (purple) and unipolar (yellow). Two lines of best fit (LoBF) were then calculated for each, from 0.2-0.8 mm^3 and 0.8-1.6 mm^3.

To further examine the effect the electrode size has on the voltage, the dimensions of the electrode were altered in four ways, as defined above. In figure 3 it can be seen that in all cases there is an inverse relationship between the electrode size and the voltage. When the dimensions of the electrode are greater than 1 mm there is only a difference of 0.1 mV which is not significant ($p = 0.99$) between increasing the electrode in diameter, height or length and width. However, changing all the dimensions still shows a considerable decrease in the voltage (4.7 to 2.2 mV).

If the length of the electrode was kept constant at 1 mm but the width and height of the electrode was reduced, the voltage will increase (gradient = 6.6) but not as rapidly as reducing the the electrode in all directions (gradient = 8.3), as the volume of the electrode remains larger. Additionally, decreasing the height of the electrode will increase the voltage but not as drastically as changing all the dimensions or the diameter. For electrodes where the height is kept constant at 1 mm it can be seen that this gives lower voltage values (8.3 to 4.7 mV) between 0.2-1 mm compared to changing the dimensions of the electrode (10 to 4.7 mV) even though the volume of the electrode is the same as when the diameter is changed.

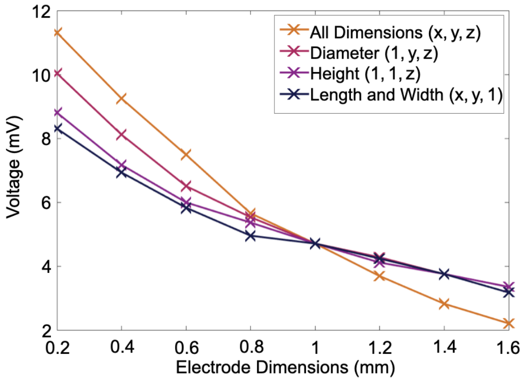

Figure 3: The figure shows a line graph comparing the bipolar voltage to changing the electrode size. The four lines each represent one or more variation in the dimensions of the electrode.

In figure 4, it can be seen that when fibrosis is included in the tissue, the amplitude of the electrogram reduces. When placed on the epicardium, there is little change in the morphology of the signal; however, the voltage is slightly reduced. This reduction in voltage remains approximately constant across the different cubic electrode sizes. When the fibrosis patch is moved into the middle of the tissue, the signal becomes more spread out and there is a time delay of 5 ms. Additionally, a substantial drop in the voltage is seen, specifically for small electrodes (11.3 to 4.9 mV for 0.2 mm^3 electrode) from healthy tissue to when fibrosis is placed in the middle of the tissue. For electrodes of size >0.8 mm^3 little change in the voltage is seen between the different sizes.

When the fibrosis patch is moved to the endocardium it can be seen that the changes are similar to when the fibrosis is located in the middle of the tissue with a slightly further reduction in the voltage. Furthermore, figure 4 shows that when the fibrosis is on the epicardial side, the bipolar voltage is greater than the unipolar. However, when the fibrotic patch is in the middle of the tissue or on the endocardial side, this is no longer the case.

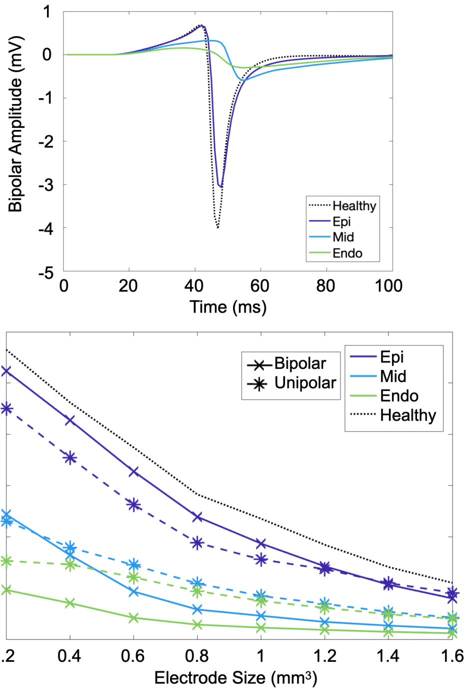

Figure 4: The figures shows the bipolar electrograms for the 1 mm^3 electrodes and the relationship between the voltage and the electrode size on the line graph when the fibrotic patch is placed at different positions in the tissue.

4. Discussion

From the results, it was observed that the electrode size can substantially affect the voltage. A big change occurs when the volume of the electrode is increased or decreased. A substantial decrease of at most 5.7 mV is seen in the voltage when one or more dimension is changed from 0.2 to 0.8 mm. The voltage continues to decrease when the dimensions are changed from 0.8 to 1.6 mm. However, the difference is not as vast, with a max change of 3.5mV. In the smaller electrodes, a much more localized signal is being obtained. Therefore, the voltage reflects the activation of the tissue just below the tissue. However, with larger electrodes, a larger area of tissue is contributing to the signals, so when the tissue at the start of the electrode is being activated the end of the electrode is still obtaining signals far away from the activation point, which will reduce the overall voltage.

A batch of simulations changing only the width and height of the electrode were performed. Therefore, a comparison could be made between changing the width and height and changing the length and height where the volume is the same but the amount of contact the electrode has to the tissue is changed. It can be seen from the results that while keeping the volume the same, the voltage is lower when changing (x,y) for all the different electrode sizes compared to changing (y,z). This shows that not only the volume has an effect on the voltage, but the electrode having more of its area further away from the tissue (larger z) also plays a role.

A fibrotic area on the epicardial side has a small influence on the endocardial voltage. However, the difference remains constant regardless of the electrode size. Therefore, increasing the electrode's volume does not result in better detection of fibrosis placed on the epicardial side. When the fibrosis is placed closer to the electrodes, then significantly smaller voltages ($p < 0.01$) are obtained than in healthy tissue. With diseased tissue, the electrode size's impact on the voltage is explicitly reduced with dimensions greater than 0.8 mm.

5. Conclusion

Electrodes with a larger volume deliver smaller voltages. The impact is much more substantial in electrodes of smaller sizes 0.2 to 0.8 mm. When fibrotic tissue is placed on the epicardium, there is a small decrease in the voltage across all electrode sizes. Fibrotic tissue located closer to the electrodes has a greater impact on the voltage. However, after 1 mm electrodes, increasing the size of the electrode no longer impacts the voltage. Therefore, either a universal electrode size should be used, or the electrode size needs to be accounted for when determining LV areas. However, any adjustment factor will need to depend on which dimension of the electrode is changed.

6. Acknowledgements

The authors thank Giorgio Luongo for his valuable suggestions and gratefully acknowledge financial support by Deutsche Forschungsgemeinschaft (DFG) through DO637/22-3 and by the Ministerium für Wissenschaft, Forschung und Kunst Baden-Württemberg through the Research Seed Capital (RiSC) program.

References

[1] Miyasaka Y, et al. Time trends of ischemic stroke incidence and mortality in patients diagnosed with first atrial fibrillation in 1980 to 2000: Report of a community-based study. Stroke a Journal of Cerebral Circulation 2005;36(11):2362–2366.

[2] Rolf S, et al. Tailored atrial substrate modification based on low-voltage areas in catheter ablation of atrial fibrillation. Circulation Arrhythmia and electrophysiology 2014; 7(5):825–33.

[3] Ammar-Busch S, et al. Predictors of low voltage areas in persistent atrial fibrillation: Is it really a matter of time? Journal of interventional cardiac electrophysiology an international journal of arrhythmias and pacing 2018;.

[4] Beheshti M, Magtibay K, Massé S, Porta-Sanchez A, Haldar S, Bhaskaran A, Nayyar S, Glover B, Deno DC, Vigmond EJ, Nanthakumar K. Determinants of atrial bipolar voltage: Inter electrode distance and wavefront angle. Computers in biology and medicine 11 2018;102:449–457.

[5] Schuler S, Keller MW, Oesterlein T, Seemann G, Dössel O. Influence of catheter orientation, tissue thickness and conduction velocity on the intracardiac electrogram. In Biomedical Engineering/Biomedizinische Technik, volume 58. 1 2013; .

[6] Anter E, Tschabrunn CM, Josephson ME. High-resolution mapping of scar-related atrial arrhythmias using smaller electrodes with closer interelectrode spacing. Circulation Arrhythmia and Electrophysiology 1 2015;8(3):537–545.

[7] Stinnett-Donnelly JM, Thompson N, Habel N, Petrov-Kondratov V, Correa de Sa DD, Bates JHT, Spector PS. Effects of electrode size and spacing on the resolution of intracardiac electrograms. Coronary artery disease 3 2012; 23(2):126–32.

[8] Courtemanche M, Ramirez RJ, Nattel S. Ionic mechanisms underlying human atrial action potential properties: Insights from a mathematical model. The American journal of physiology 7 1998;275(1 Pt 2):H301–21.

[9] Kojodjojo P, Peters NS, Davies DW, Kanagaratnam P. Characterization of the electroanatomical substrate in human atrial fibrillation: the relationship between changes in atrial volume, refractoriness, wavefront propagation velocities, and AF burden. Journal of Cardiovascular Electrophysiology 1 2007;18(3):269–275.

[10] Gimsa J, Müller T, Schnelle T, Fuhr G. Dielectric spectroscopy of single human erythrocytes at physiological ionic strength: Dispersion of the cytoplasm. Biophysical Journal 1 1996;71(1):495–506.

[11] Issa ZF, Miller JM, Zipes DP. Electrophysiological testing 1 2012;62–91.

Address for correspondence:

Deborah Nairn
Institute of Biomedical Engineering, Karlsruhe Institute of Technology (KIT), Fritz-Haber-Weg 1, 76131 Karlsruhe, Germany
publications@ibt.kit.edu

Chapter 5

Electro-anatomical Mapping during Atrial Fibrillation

Electroanatomic mapping is normally performed during SR, in which areas with voltage less than 0.5 or 1 mV are considered low voltage and areas to target when performing ablation [17, 18, 81, 88]. Therefore, if patients arrive with ongoing AF, commonly, they are cardioverted to be mapped during SR. However, mapping during AF may be beneficial to identify underlying substrate not identified during SR. Therefore, patients arriving in SR could also be induced and mapped in AF. Induced arrhythmia may be driven by a different mechanism than the "native" spontaneous AF. Therefore, by cardioverting the patient initially, there may be a loss of information when the patient is then induced back into AF to identify regions of pathological substrate. Additionally, performing the mapping procedure during native AF could help avoid potential multiple cardioversions. Whilst the cut-off values have been well established in SR, there is still uncertainty in AF as to what cut-off value should be applied and how the two rhythms relate to one another to identify LVS.

In the first section of this chapter, the submitted journal manuscript/ pre-print paper investigates the relationship between the two mapping procedures [89]. First, the spatial and quantitative distribution of bipolar low voltage areas in SR vs. in AF was evaluated. It can happen that the voltage maps in SR and in AF are on different geometries for one patient. Therefore, it was important to project the information onto a mean geometry created in this work so that the analysis was not hindered by variations caused by spatial displacement. It was found that setting the AF threshold to 0.34 mV provided the best match to SR (0.5 mV) with an accuracy of 69%. However, this could result in an over or underestimation of the LVS extent when exploring the anatomical regions of the left atrium (LA) separately. By applying separate regional thresholds, this could be corrected. Specifically, the posterior and inferior wall threshold would need to be lower around 0.27-0.30 mV for the extent of LVS to not be overestimated. On the other hand, applying a higher threshold of 0.36-0.39 mV on the anterior and lateral wall could lead to the substrate not being underestimated. While this lead to strong concordance in about 70% of patients, significant discrepancies persist in the remaining patients. Therefore, indicating that perhaps patient specific mapping strategies need to be investigated. To understand the effects of inducing AF rather than mapping patients whom presented in AF, the patient dataset was split accordingly. While the voltage values in native AF were slightly higher, there was no significant difference from the induced AF values. However, when comparing back to the SR maps, it was found that the induced AF maps correlated significantly better to the SR maps (AUC 0.80) compared to the native AF (AUC 0.73).

The first section used the voltage values provided by the CARTO-3 mapping system and their approach to determine the voltage, as it is widely used and accepted. However, there is no clear consensus on how the voltage should be calculated, with other manufacturers using different definitions. In the CARTO-3 system, only one atrial beat is considered when calculating the voltage. In AF, however, this may not be the most robust method to identify LVS when the wavefront propagation is complex, causing the signal to change over time. Therefore, in the second section of this chapter, different AF voltage calculation techniques were compared to the SR voltage map to determine the highest correspondence between mapping in the two rhythms. First, in a conference paper, by comparing the different techniques in non-fractionated signals, it was seen that the CARTO-3 value often differed from using the mean or median voltage value across the signal. However, little variability occurred when using different methods for different regions. Therefore, using one method was sufficient for calculating the voltage across the entire atrium. The study was then advanced, investigating the variability of the signals and comparing the voltage techniques to the SR voltage map. It was identified that while the variation was not substantial in most signal, about 8% of the patients' signals showed greater variability (standard deviation across voltage values of one signal $> 0.5\,\text{mV}$), perhaps due to complex wavefront propagations passing by the electrodes or movement of the catheter. Additionally, looking at the variation within one signal (sample entropy) may help to understand the phenomena taking place below the catheter. Furthermore, the optimal AF voltage calculation technique to identify LVS as found in the SR voltage map (areas $< 0.5\,\text{mV}$) is to take the maximum peak-to-peak (p2p) amplitude of the signal.

The work presented in this chapter indicates that the AF voltage maps using the proposed threshold could identify areas of LVS as located during SR. Therefore, multiple cardioversion procedures could be avoided. However, some discrepancies still exist between the two rhythms. Using the provided regional threshold and using the maximum p2p amplitude of the signal to calculate the voltage, the concordance between the two rhythms can improve and prevent over or underestimates of identifying LVS as found when mapping during SR. Additionally, it was found that mapping with native AF reduced the concordance to SR. However, this helped identify that multiple wavefronts and complex propagation patterns during AF may hinder the mapping procedure and cause discrepancies between the rhythms. Also, looking at the sample entropy may help overcome these discrepancies and further understand the type of pathological substrate below the catheter.

5.1 Voltage Mapping during AF

Spatial Correlation of Left Atrial Low Voltage Substrate in Sinus Rhythm versus Atrial Fibrillation: Identifying the Pathological Substrate Irrespective of the Rhythm

Deborah Nairn[1]*[#], Martin Eichenlaub[2#], Heiko Lehrmann[2], Björn Müller-Edenborn[2], Juan Chen[2], Taiyuan Huang[2], Claudia Nagel[1], Jorge Sánchez[1], Giorgio Luongo[1], Thomas Arentz[2], Olaf Dössel[1], Amir Jadidi[2§] and Axel Loewe[1§]

[1]*Institute of Biomedical Engineering, Karlsruhe Institute of Technology (KIT), Karlsruhe, Germany*

[2]*Department of Electrophysiology, University-Heart-Center Freiburg-Bad Krozingen, Bad Krozingen, Germany.*

[#],[§] *These authors contributed equally.*

Abstract

Background: Low voltage substrate (LVS) identified during electroanatomical mapping is a potential target for atrial fibrillation (AF) ablation. However, it is not clear how the location and extent of LVS correlate between mapping in sinus rhythm (SR) and AF.

Objectives: (1) Identify voltage dissimilarities between mapping in SR and AF. (2) Identification of regional voltage thresholds that improve cross-rhythm substrate detection. (3) Comparison of LVS between SR and native vs. induced AF.

Methods: Forty-one ablation-naive persistent AF patients underwent high-density voltage mapping in SR and AF. Each patient's voltage information was mapped to a joint geometry for analysis. Global and regional voltage thresholds in AF were identified which best match LVS$<$0.5 mV and $<$1.0 mV in SR. Additionally, the correlation between SR-LVS with induced vs. native AF LVS was assessed.

Results: Substantial voltage differences (median: 0.52, IQR: 0.33-0.69, max: 1.19 mV) with predominance of the posterior/inferior LA wall exist between the rhythms. An AF threshold of 0.34 mV for the entire atrium provides an accuracy, sensitivity and specificity of 69%, 67% and 69% to identify SR-LVS<0.5 mV, respectively. Lower thresholds for the posterior wall (0.27 mV) and inferior wall (0.3 mV) result in higher spatial concordance to SR-LVS (4% and 7% increase). Concordance with SR-LVS was higher for induced AF compared to native AF (AUC: 0.80 vs. 0.73). AF-LVS<0.5 mV corresponds to SR-LVS<0.97 mV using high-definition mapping (AUC: 0.73).

Conclusion: The proposed voltage thresholds during AF maximise the consistency of LVS identification as determined during SR. Regional thresholds can further improve concordance.

Key Words: Atrial Fibrillation, Sinus Rhythm, Low Voltage Substrate, Induced AF, Regional Analysis, Voltage Mapping, Ablation

1. Introduction

Atrial fibrillation (AF) is the most common sustained cardiac arrhythmia characterised by rapid irregular beating of the atria and associated with an increased risk for stroke and heart failure [1]. The pulmonary veins are the primary trigger site of AF. Isolating the pulmonary veins can yield a high rate of arrhythmia freedom in paroxysmal AF patients [2]. However, the success rate is often lower in persistent AF patients due to additional pathological substrate contributing to arrhythmia maintenance [3, 4, 5].

Electro-anatomical mapping to identify low bipolar voltages (peak-to-peak amplitudes) <0.5 mV or 1 mV during sinus rhythm (SR) have been shown to be a promising technique to identify the additional pathological substrate [4, 6, 7, 8, 9]. However, mapping in SR is not always feasible: e.g. when AF reoccurs shortly after electrical cardioversion due to recurrent / sustained fibrillatory trigger activity. Moreover, electrophysiologists may chose to perform mapping during AF, in order to identify both the potential arrhythmogenic rapid trigger sites and the underlying pathological substrate [10, 11, 12].

To date, two voltage cut-off values have been reported in SR that allow identification of potentially proarrhythmogenic tissue: <1 mV in SR [13] and Rolf et al. reported ablation and isolation of atrial areas <0.5 mV to improve SR maintenance rates at 12 months [6]. When mapping is done in AF, atrial areas displaying LVS <0.5 mV have been reported as potential arrhythmogenic sites [4, 7]. Uncertainties remain regarding which cut-off values should be applied when mapping during AF and how the voltages in both rhythms relate to one another. The aim of the current study was to compare LVS in SR and AF and to identify regional voltage thresholds to improve cross-rhythm substrate detection.

2. Methods

2.1. Patient cohort

Forty-one patients with persistent AF presenting for their first AF ablation procedure were included in the study. Six weeks prior to AF ablation procedure, all patients were electrically cardioverted to SR, in order to enable favourable reverse electrical remodeling [14]. Patients presenting with SR on procedure date (11/41) underwent voltage and activation mapping in SR first, followed by voltage mapping during induced AF and subsequent PVI. Patients with native AF on procedure date (30/41) first underwent voltage mapping in AF, followed by electrical cardioversion, voltage and activation mapping in SR and finally PVI. Mapping was performed five minutes after AF induction, and only if AF was maintained for the entire mapping time. In two patients (5% of patients) with important sinus rhythm bradycardia and hypotension, pacing from the coronary sinus was performed.

2.2. Electro-anatomical Mapping

High-density voltage mapping was performed on forty-one persistent AF patients using the CARTO-3 mapping system (Biosense Webster, Diamond Bar, CA, USA) and a 20-pole (electrode size: 1 mm, spacing: 2–6–2 mm) Lasso-Nav catheter.

To avoid including information from points with poor contact, measurements were disregarded if the electrodes were located >6 mm from the atrial surface. Band-pass filtering at 16-500 Hz was applied to the bipolar electrograms. To calculate the voltage, in SR a window of interest was chosen restricted to the PR interval in the ECG. In AF, the window of interest was set to include a single

AF beat, with exclusion of QRS complex. Within this window, the peak-to-peak amplitude of the signal was calculated. Voltage values between the electrode positions were interpolated by the CARTO-3 system. Cut-off values of <0.5 and <1.0 mV were then applied to the bipolar SR voltage maps to define the low voltage substrate (LVS) [4, 8]. Areas demonstrating LVS were confirmed using a separate contact force-sensing mapping catheter with a contact threshold of >5 g.

2.3. Analysis

Using the Scalismo statistical shape modelling software [15, 16, 17], the geometries of each patient were aligned and registered to a mean LA geometry [18]. This allowed the transfer of voltage information from each patient's individual geometry to a common geometry represented by the same number of surface points, which represent the same anatomical landmarks. In this way, the analysis is not hindered by variations caused by spatial displacement. Additionally, the pulmonary veins and mitral valve areas could be easily treated separately during the analysis.

Equidistant points were chosen across the entire atria with a 3 mm interpoint distance. The voltage value for each point was calculated as the mean amplitude of all points within a 1.5 mm radius to compare local areas between the two rhythms.

To investigate the correlation between SR and AF, receiver operation curves (ROC) were created across the whole patient cohort, with the SR map being considered as the reference condition. The optimal AF thresholds for both SR cut-off values (0.5 and 1 mV) were identified and the sensitivity, specificity and accuracy were computed for each patient. In a subsequent local analysis, the percentage of patients showing consistent classification as low or high voltage in both rhythms per point was determined to identify the spatial concordance pattern.

A map of the median voltage values was constructed across the entire patient cohort for both rhythms. This allows a visual comparison between the maps without the influence of outliers due to patient-specific differences. Additionally, a map showing the difference between SR and AF median voltage values across all patients was computed.

The atrium was split into anatomical regions to examine the difference between SR and AF voltage mapping and identify optimal voltage thresholds for different atrial regions: inferior wall, lateral wall, posterior wall, anterior wall and roof. The optimal threshold for each region was identified as the top left-hand corner of the ROC curve when comparing the identification of low voltage regions between rhythms in that region.

Finally, the patient cohort was split into two groups: (1) where induced AF was mapped (patients presenting in SR) and (2) where native AF was mapped (patients presenting in AF). The two patients where the CS was paced to maintain SR were removed from this part of the study due to the unknown effect of how different fast pacing from the CS relates to AF. This group was too small to be considered separately. A two-sample t-test was performed to investigate if the voltage values between the two groups were significantly different. The two groups were then compared to their respective SR maps and ROC curves were computed. Since more patients were mapped with native AF (65%), a leave p-out (p=11) cross-validation was performed for the native ROC curve. A two-sample t-test was additionally performed between the distance of the two ROC curves in respect to the top left-hand corner.

3. Results

3.1. Patient characteristics

Forty-one persistent AF patients (63 ± 11.1 years old, 43.9% female) presenting for their first AF ablation procedure were included. On procedure date, 30 of 41 (73%) patients recurred with persistent AF. Table 1 describes further details regarding the patients' characteristics.

3.2. Spatial distribution of left atrial voltage during SR and AF

Figure 1 shows the distribution of LVS for a representative patient for mapping both during SR and AF. While the location of the LVS matches well between the rhythms on both the anterior and posterior wall, the extent is bigger in the AF map when using a cut-off value of 0.5 mV for both maps. The voltage maps for all patients are shown in the supplementary material (Figure S1).

Figure 2 shows the spatial distribution of the median voltages across the entire patient cohort during both SR and AF. Voltages are lower across the entire atrium in AF (0.48±0.32 mV) than in SR (0.93±0.40 mV). The biggest differences between the median voltages in SR and AF of up to 1.1 mV are seen on the posterior and inferior wall. On the anterior wall, differences are smaller (0.35±0.14 mV). In both maps, the lowest voltages occur around the PVs and on the anterior wall (mean±std: 0.77±0.19 mV), with the highest voltages in the LAA (1.87±0.27 mV).

Patient Characteristics	**Total = 41**
Age (years)	63 ± 11.1
Female (%)	18 (43.9)
BMI (kg/sqm^2)	27.8 ± 6.1
Arterial Hypertension (%)	23 (56.1)
Diabetes mellitus (%)	5 (12.2)
Prior stroke (%)	1 (2.4)
structural CMP (%)	12 (29.2)
Coronary artery disease (%)	6 (14.6)
Persistent atrial fibrillation (%)	41 (100)
CHA_2DS_2-VASc score	1.7 ± 1.4
Initial Rhythm SR (%)	11 (26.8)
History of AF (months since diagnosis) (%)	38 ± 41
AA-therapy on admission (%)	17 (41.5)
Betablocker Therapy Only (%)	18 (43.9)
Amiodarone (%)	11 (26.8)
Flecainide (%)	3 (7.3)
Sotalol (%)	1 (2.1)
Dronedarone (%)	2 (4.8)
LA diameter (AP, mm)	42.8 ± 6.9
LVEF (%)	50.4 ± 4.1
LV dysfunction (LVEF<50%)	6 (14.6)
LVEDD (mm)	48.7 ± 6.1
LA dilatation (>40 mm)	28 ± 68.3
Creatinine clearance (ml/min/1.73 sqm)	74.1 ± 16.7

Table 1: **Patient clinical demographics.** Abbreviations: BMI = body mass index, AA = antiarrhythmic, LA = left atrial, LVEF = left ventricular ejection fraction, LV = left ventricle, LVEDD = left-ventricular end-diastolic diameter

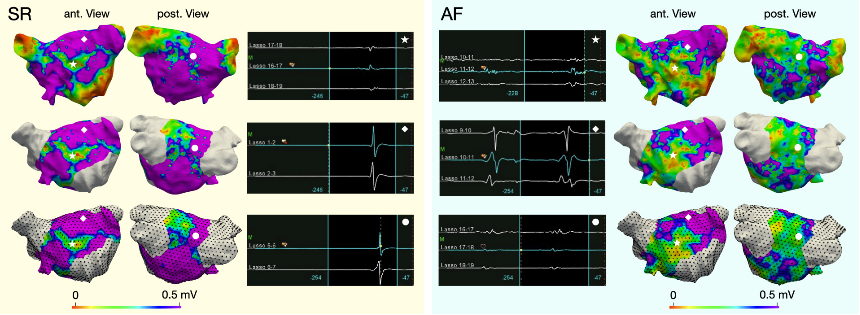

Figure 1: **Spatial distribution of low voltage in SR and AF in one patient.** Voltage maps in the top row are shown on the patient's geometry. The middle row shows the voltage projected onto the joint geometry after exclusion of pulmonary vein and mitral valve areas. The bottom row shows the equidistant points (black dots) where the mean amplitude of all points within a 1.5 mm radius was considered. SR voltage map and relating signals are shown on the left (yellow box), AF on the right (blue box). The icons mark spatial points on the atrial geometry for which the corresponding signals are shown in the middle columns.

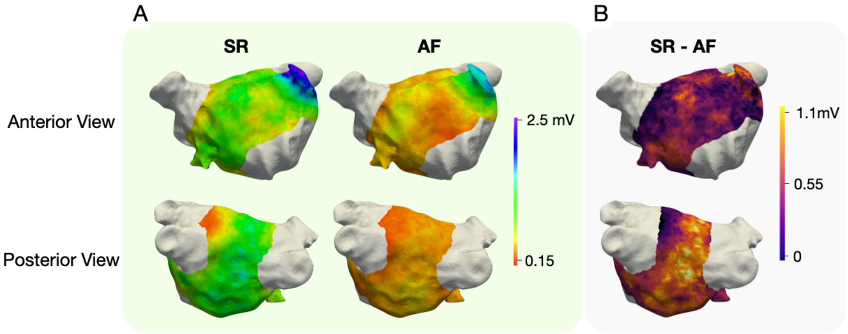

Figure 2: **(A) Median voltage across all patients during SR and AF and (B) the difference of median voltage between the two rhythms.**

3.3. Global AF thresholds for the detection of SR-LVS

ROC curve analysis provided the optimal threshold in AF for identifying LVS in SR. AF thresholds 0.34 and 0.45 mV for SR <0.5 mV and <1 mV provided the best balance between high sensitivity and specificity as identified by the top left-hand corner of the ROC curve (Figure 3A). The percentage of concordance was moderate with a sensitivity of 67% (<0.5 mV) and 66% (<1 mV), specificity 69% (<0.5 mV) and 68% (<1 mV) and accuracy 69% (<0.5 mV) and 65% (<1 mV). The performance of the new AF voltage thresholds varied between patients with per-patient accuracy ranging between 53% and 94% (mean 69±11% for SR <0.5 mV, mean 67±11% for SR <1 mV) (Figure 3B). In the supplementary material figure S2, the ROC curve identifying the optimal threshold in SR for AF <0.5 mV is shown.

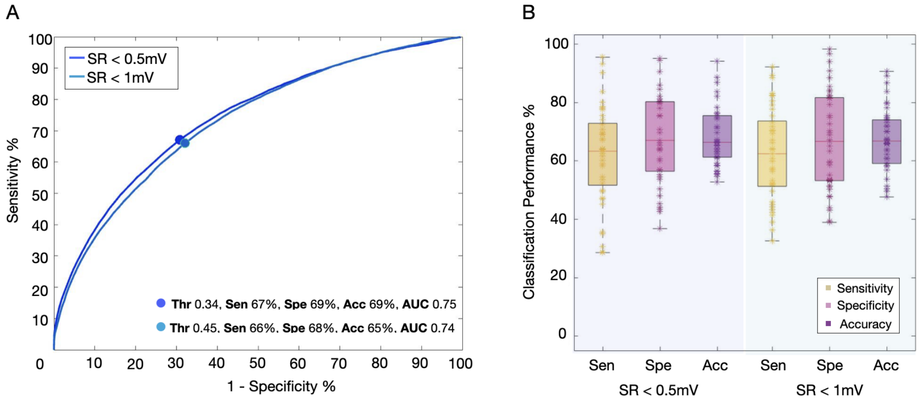

Figure 3: **Cross-rhythm classification consistency**. (A) ROC curve comparing LVS as identified during SR for bipolar thresholds <0.5 mV and 1 mV and during AF. The optimal AF thresholds across all patients and corresponding performance metrics are given in the legend. (B) classification performance parameters for each patient using the threshold obtained from the ROC curve.

Figure 4 shows the spatial distribution of the percentage of patients who demonstrate agreement of LVS areas in both SR and AF in a local neighbourhood. Agreement was high in the LAA (88±3% of patients). When using 0.5 mV as the cut-off value in both SR and AF, there is agreement on the anterior wall (62±8%). However, the agreement is substantially smaller on the inferior and posterior walls (48±8%). By lowering the AF voltage thresholds to the values identified by the ROC curve analysis (figure 3A), the agreement on the anterior wall and inferior increased (69±8% and 61±8%).

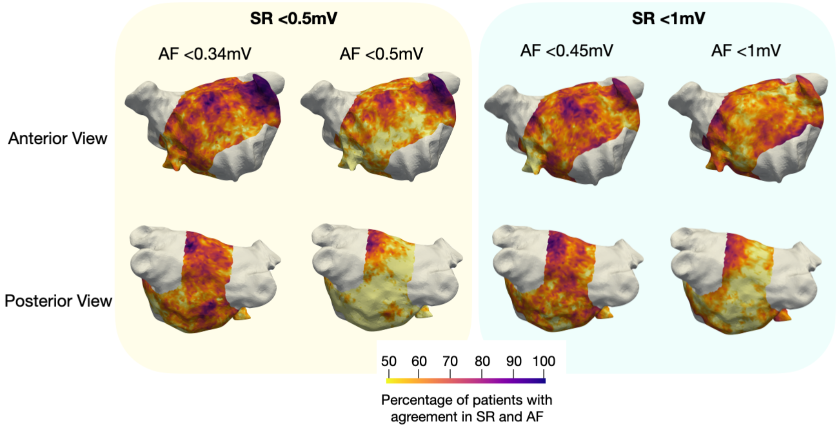

Figure 4: **Agreement map between SR and AF.** Each map shows the percentage of patients in which both voltage maps in SR and AF agree that low or high voltage is located within a local neighbourhood. The yellow box shows the agreement with SR <0.5 mV, the light blue box with SR <1 mV. In each box, the left column uses the optimal AF voltage thresholds as identified by the ROC curve analysis (Figure 3A).

3.4. Regional AF thresholds for the detection of SR-LVS

The lowest concordance between SR and AF using the global optimal threshold for the entire atrium was found at the inferior wall (accuracy: 62%). By applying a regional AF threshold (0.3 mV), the accuracy on the inferior wall increased by 4%. For the posterior wall, an even lower AF threshold (0.27 mV) increased the accuracy from 69% to 76%. In both regions, the new regional thresholds decreased the sensitivity and increased the specificity. From figure 2 it can be seen that the voltage values are markedly higher on the posterior/inferior wall in SR than in AF. The entire atrium threshold is therefore too sensitive for these regions. On the other hand, on the anterior and lateral wall, a slightly higher threshold (0.36 and 0.39 mV respectively) can optimally locate the regions of SR-LVS using the AF voltage map. The optimal AF regional thresholds which correspond to SR <1 mV are shown in the supplementary material (Figure S3). The ROC curves used to find the optimal regional thresholds are shown in Figure S4.

3.5. Impact of inducing AF

The voltage was slightly higher in native AF patients than in patients in whom AF was induced (Figure 6A, not significant). The ROC curves (Figure 6B) show that the correlation between AF-LVS and SR-LVS is significantly ($p<0.05$) better in patients in whom AF was induced (AUC: 0.80 vs. 0.73). The optimal AF threshold for identifying SR-LVS <0.5 mV was lower for patients in whom AF was induced (0.3 mV). In the supplementary material Figure S5, the boxplots and histograms can be seen for SR voltage values for patients who were cardioverted after mapping native AF versus first mapping native SR and then inducing AF. Although the difference was also not significant, the voltage values were typically higher in the patients mapped first in SR (median 1.66 mV vs. 0.77 mV).

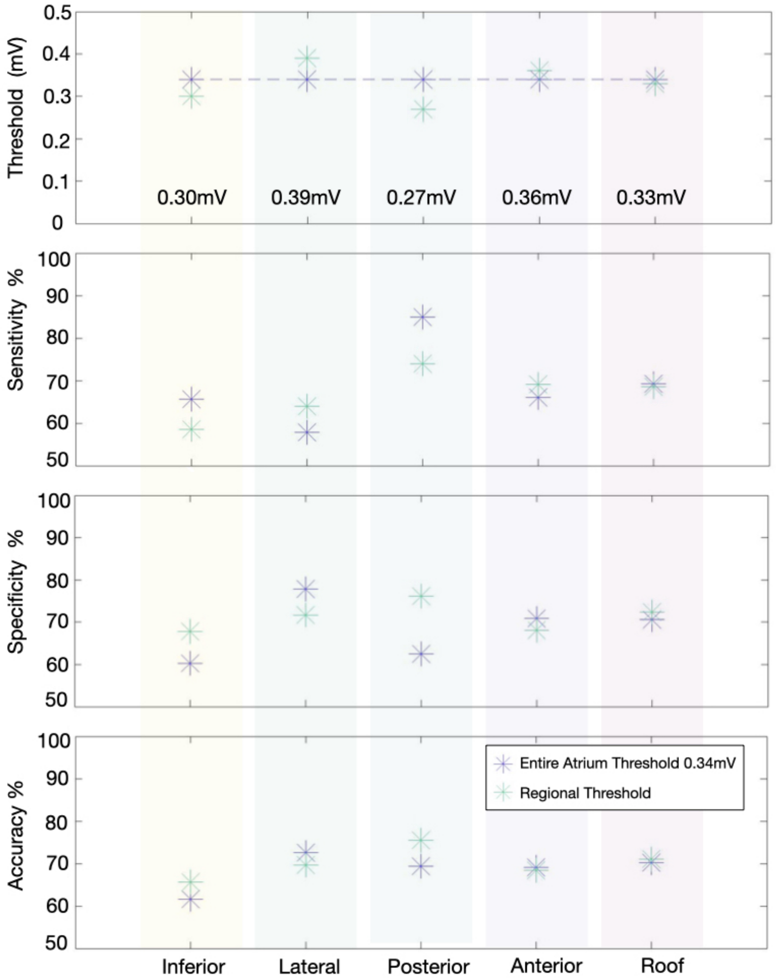

Figure 5: **Optimal AF threshold and the corresponding sensitivity, specificity and accuracy for each anatomical region of the LA comparing to SR <0.5 mV.** The previously defined global threshold for the entire atria is shown by the purple asterisk while the green asterisk represents the regional threshold.

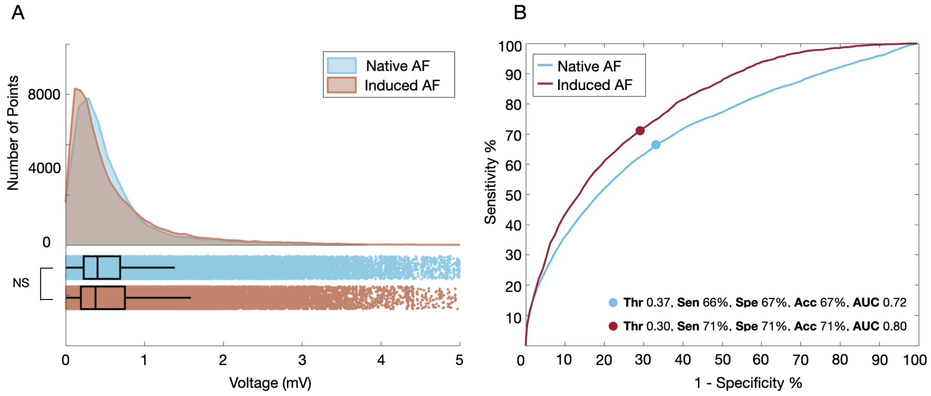

Figure 6: **Histogram and boxplot of the voltage distribution in patients in whom AF was induced versus native AF. ROC curves comparing the AF-LVS in each group to SR-LVS.** Blue: patients which presented with native AF, red: patients with induced AF.

4. Discussion

4.1. Main findings

This study investigated the differences in low voltage substrate identification for mapping during SR and AF. Three key findings can be reported:

1. The overall correspondence of LVS mapped in SR and in AF is moderate.
2. Discrepancies exist between mapping in SR and AF, specifically on the posterior and inferior LA wall.
3. New regional AF cut-off values improve detection of LVS as identified by mapping in SR.
4. The concordance of SR and AF voltage maps is higher when AF was induced compared to native AF.

4.2. AF cut-off values for identifying low voltage substrate

While cut-off values of <0.5 and 1 mV are quite well established for mapping in SR [4, 8, 9], there is still no clear consensus whether the threshold applied when mapping during AF should be the same. A recent study using generalised additive models with a patient cohort of 31 patients found that a cut-off value of 0.31 mV was best for predicting <0.5 mV SR-LVS [19]. However, a point-by-point analysis was performed in this study, which could have been affected by undetected map shifts. To counter this problem, we analyse the data in small equidistant regions with a radius of 3 mm. Regardless, a similar cut-off value was found based on ROC curve analysis and local neighbourhood analysis (as opposed to point-by-point analysis) to determine the best cut-off value (0.34 mV). When examining LVS in AF as identified by regions <1 mV in SR, a cut-off value of 0.45 mV is optimal. However, as identified by the difference of the median voltage maps (figure 2), pronounced differences between the rhythms are present on the posterior and inferior walls. By adjusting the threshold for each region, the extent and location of SR-LVS can be better estimated when mapping during AF.

4.3. Differences in SR and AF voltage mapping

By examining the median voltages across the entire patient cohort for both rhythms, we showed that the voltages in SR are higher than in AF. This result is consistent with other studies [19, 7, 20] and can be due to multiple wavefronts coming from various directions and endo-epicardial dissociation during AF [21]. Therefore, there are fewer coherent sources contributing to the electrograms. Moreover, neighbouring tissue may be depolarised by slightly delayed wavefronts, resulting in more fractionated signals and lower voltage amplitudes in AF [22]. This is further verified by the study from Ndrepepa el al., who identified that a reduction in voltage strongly correlates with the degree of AF disorganization [20].

While the voltage is typically lower in AF than SR, this study identified that this difference is not uniform across the entire atrium. The differences between rhythms were found to be much higher on the posterior and inferior LA wall (difference typically >0.55 mV) than on the anterior (difference typically <0.55 mV). Kurata et al. also reported higher voltages on the posterior region than the anterior region in both patients with and without low voltage areas [23]. Additionally, a recent study comparing voltage maps to LGE-MRI identified that the correlation between the two modalities was significantly better on the posterior wall when the voltage map was acquired during AF vs. SR [24]. One explanation drawn is that non-transmural or patchy fibrosis might be underestimated when mapping in SR. Sánchez et al. reported that low density fibrosis or electrode not located directly on top of the core of the fibrosis may cause discrete changes to the electrogram characteristics [25, 26]. On the other hand, when activation rates are more rapid during AF, non-transmural or patchy fibrotic tissue may be more susceptible to functional reentry, slow conduction or conduction block, which results in low voltage areas [27, 24]. However, catheter ablation of LGE-areas (including those at the posterior LA) did not improve the SR maintenance rates compared to PVI-only, in the large prospective multicenter trial DECAAF II [28]. Further computational studies may elucidate the mechanisms of rhythm-dependent voltage discrepancies on the posterior wall. Moreover, besides low voltage areas and LGE-areas, additional markers for arrhythmogenesis (e.g. repetitive rapid activity in AF or atrial late potentials in SR [12]) need to be considered by electrophysiologists to enable both a sensitive and specific detection of trigger sites for AF.

4.4. Influence of inducing AF in patients

We found that the correlation between SR and AF voltage mapping was better when the AF was induced in the patient. One hypothesis is that native AF is on average more complex, with high level of electrical remodeling, endo-epicardial dissociations of wavelet activities and more wavefronts originating from multiple directions than in induced AF that is mapped few minutes after its initiation [29, 21].

In the current study all persistent AF patients underwent electrical cardioversion to SR six weeks prior to scheduled AF ablation, in order to allow favourable reverse remodelling [14]. Patients who recurred with AF on the procedure date may have a more advanced form of electrical and structural LA remodelling than those who maintained SR. [30]. Thus, they may present with more complex patterns of propagation, such as multiple wavefronts and reentries. In this study, the mean voltages during SR are higher in the patients who presented with SR (median: 1.16 mV, IQR: 0.51-2.18 mV) than those who recurred with AF (median: 0.77 mV, IQR: 0.37-1.44 mV). A recent study reported that patients with extensive mean regional voltage reductions demonstrated whole LA degeneration [23]. This indicates a more advanced stage of arrhythmic remodelling in patients with AF recurrence six weeks after cardioversion to SR.

5. Limitations

The CARTO-3 mapping system was used for this study with a 20-pole Lasso catheter with electrodes of size 1 mm. Therefore, the AF thresholds may not apply to other systems or catheter configurations. In some patients, AF was mapped first and then the patient was cardioverted, potentially affecting the results by undetected map shifts. To counteract this, all patients' voltage information was mapped to a joint geometry and analysis points comprised of the mean voltage in a 1.5 mm radius. The current study used high-density bipolar voltage mapping to compare LVS in SR and AF. The impact of omnipolar voltage mapping was not evaluated. However, comparing unipolar vs. bipolar voltage mapping modes, we recently reported that with high-density mapping, the direction of activation front to mapping electrodes does not significantly influence the extent and localization of detected LVS (both for SR and AF) [8].

6. Conclusion

The proposed AF thresholds improve the identification of SR-LVS, when mapping is performed during AF. However, a global threshold for the entire atria can lead to over- or underestimation of LVS, which can be corrected to some extent by applying the reported regional thresholds. Mapping in AF may be necessary in patients who cannot be cardioverted or maintained in SR or when AF mapping for detection of rapid activity sites is chosen. However, while application of the regional thresholds results in high concordances in LVS detection in about 70% of patients, significant discrepancies persist in the remaining patients. Further investigation needs to be undertaken to identify the role of complex propagation patterns in the characterisation of LVS when mapping during AF.

Acknowledgements

We gratefully acknowledge financial support by Deutsche Forschungsgemeinschaft (DFG) through DO637/22-3, by the Ministerium für Wissenschaft, Forschung und Kunst Baden-Württemberg through the Research Seed Capital (RiSC) program.

References

[1] A. S. Go, D. Mozaffarian, V. L. Roger, et al., Heart disease and stroke statistics–2014 update: a report from the American Heart Association., Circulation 129 (3) (2014) e28–e292. doi:10.1161/01.cir.0000441139.02102.80.

[2] P. Taghji, M. El Haddad, T. Phlips, et al., Evaluation of a strategy aiming to enclose the pulmonary veins with contiguous and optimized radiofrequency lesions in paroxysmal atrial fibrillation: A pilot study., JACC: Clinical Electrophysiology 4 (1) (2018) 99–108. doi:10.1016/j.jacep.2017.06.023.

[3] A. Verma, C. Jiang, T. R. Betts, et al., Approaches to catheter ablation for persistent atrial fibrillation., The New England Journal of Medicine 372 (19) (2015) 1812–22. doi:10.1056/NEJMoa1408288.

[4] A. S. Jadidi, H. Lehrmann, C. Keyl, et al., Ablation of persistent atrial fibrillation targeting low-voltage areas with selective activation characteristics, Circulation. Arrhythmia and Electrophysiology 9 (3) (2016) e002962. doi:10.1161/CIRCEP.115.002962.

[5] S. Kircher, A. Arya, D. Altmann, S. Rolf, A. Bollmann, P. Sommer, N. Dagres, S. Richter, O.-A. Breithardt, B. Dinov, D. Husser, C. Eitel, T. Gaspar, C. Piorkowski, G. Hindricks, Individually tailored vs. standardized substrate modification during radiofrequency catheter ablation for atrial fib-

rillation: a randomized study, EP Europace 20 (11) (2018) 1766–1775. doi:10.1093/europace/eux310.

[6] S. Rolf, S. Kircher, A. Arya, et al., Tailored atrial substrate modification based on low-voltage areas in catheter ablation of atrial fibrillation., Circulation. Arrhythmia and Electrophysiology 7 (5) (2014) 825–33. doi:10.1161/CIRCEP.113.001251.

[7] A. Yagishita, S. DE Oliveira, I. Cakulev, J. R. Gimbel, D. Sparano, H. Manyam, A. Manrique-Garcia, M. Arrendondo, J. Mackall, M. Arruda, Correlation of left atrial voltage distribution between sinus rhythm and atrial fibrillation: Identifying structural remodeling by 3-d electroanatomic mapping irrespective of the rhythm, Journal of Cardiovascular Electrophysiology 27 (2016) 905–912. doi:10.1111/jce.13002.

[8] D. Nairn, H. Lehrmann, B. Müller-Edenborn, et al., Comparison of unipolar and bipolar voltage mapping for localization of left atrial arrhythmogenic substrate in patients with atrial fibrillation, Frontiers in Physiology 11 (2020) 575846. doi:10.3389/fphys.2020.575846.

[9] G. Yang, B. Yang, Y. Wei, F. Zhang, W. Ju, H. Chen, M. Li, K. Gu, Y. Lin, B. Wang, K. Cao, P. Kojodjojo, M. Chen, Catheter ablation of nonparoxysmal atrial fibrillation using electrophysiologically guided substrate modification during sinus rhythm after pulmonary vein isolation., Circulation. Arrhythmia and electrophysiology 9 (2) (2016) e003382. doi:10.1161/CIRCEP.115.003382.

[10] J. Seitz, C. Bars, G. Théodore, et al., AF ablation guided by spatiotemporal

electrogram dispersion without pulmonary vein isolation: A wholly patient-tailored approach., Journal of the American College of Cardiology 69 (3) (2017) 303–321. doi:10.1016/j.jacc.2016.10.065.

[11] M. Haissaguerre, M. Hocini, P. Sanders, Y. Takahashi, M. Rotter, F. Sacher, T. Rostock, L.-F. Hsu, A. Jonsson, M. D. O'Neill, P. Bordachar, S. Reuter, R. Roudaut, J. Clementy, P. Jais, Localized sources maintaining atrial fibrillation organized by prior ablation, Circulation 113 (5) (2006) 616–625. doi:10.1161/CIRCULATIONAHA.105.546648.

[12] A. Jadidi, M. Nothstein, J. Chen, et al., Specific electrogram characteristics identify the extra-pulmonary vein arrhythmogenic sources of persistent atrial fibrillation - characterization of the arrhythmogenic electrogram patterns during atrial fibrillation and sinus rhythm., Scientific Reports 10 (1) (2020) 9147. doi:10.1038/s41598-020-65564-2.

[13] A. Jadidi, B. Müller-Edenborn, J. Chen, C. Keyl, R. Weber, J. Allgeier, Z. Moreno-Weidmann, D. Trenk, F.-J. Neumann, H. Lehrmann, T. Arentz, The duration of the amplified sinus-p-wave identifies presence of left atrial low voltage substrate and predicts outcome after pulmonary vein isolation in patients with persistent atrial fibrillation., JACC. Clinical electrophysiology 4 (4) (2018) 531–543. doi:10.1016/j.jacep.2017.12.001.

[14] L. Rivard, M. Hocini, T. Rostock, B. Cauchemez, A. Forclaz, A. S. Jadidi, N. Linton, I. Nault, S. Miyazaki, X. Liu, O. Xhaet, A. Shah, F. Sacher, N. Derval, P. Jaïs, P. Khairy, L. Macle, S. Nattel, S. Willems, M. Haïssaguerre, Improved outcome following restoration of sinus rhythm prior to catheter ablation of persistent atrial fibrillation: A

comparative multicenter study, Heart Rhythm 9 (7) (2012) 1025–1030. doi:10.1016/j.hrthm.2012.02.016.

[15] M. Lüthi, T. Gerig, C. Jud, T. Vetter, Gaussian process morphable models., IEEE transactions on pattern analysis and machine intelligence 40 (8) (2018) 1860–1873. doi:10.1109/TPAMI.2017.2739743.

[16] G. Bouabene, et al., Scalismolab: Scalable image analysis and shape modelling., `https://scalismo.org`.

[17] C. Nagel, S. Schuler, O. Dössel, et al., A bi-atrial statistical shape model for large-scale in silico studies of human atria: model development and application to ECG simulations, Medical Image Analysis 74 (2021) 102210. doi:10.1016/j.media.2021.102210.

[18] D. Nairn, C. Nagel, B. Mueller-Edenborn, et al., Spatial and quantitative assessment of the correlation between sinus rhythm and atrial fibrillation voltage mapping to identify low voltage substrate in persistent atrial fibrillation, in: EP Europace. EHRA Abstracts, Vol. 23 (S3), 2021. doi:10.1093/europace/euab116.163.

[19] M. Rodríguez-Mañero, M. Valderrábano, A. Baluja, et al., Validating left atrial low voltage areas during atrial fibrillation and atrial flutter using multielectrode automated electroanatomic mapping, JACC: Clinical Electrophysiology 4 (12) (2018) 1541–1552. doi:10.1016/j.jacep.2018.08.015.

[20] G. Ndrepepa, M. A. Schneider, M. R. Karch, et al., Impact of atrial fibrillation on the voltage of bipolar signals acquired from the left and right

atria, Pacing and Clinical Electrophysiology 26 (4p1) (2003) 862–869. doi:10.1046/j.1460-9592.2003.t01-1-00151.x.

[21] J. Eckstein, B. Maesen, D. Linz, S. Zeemering, A. van Hunnik, S. Verheule, M. Allessie, U. Schotten, Time course and mechanisms of endo-epicardial electrical dissociation during atrial fibrillation in the goat, Cardiovascular Research 89 (4) (2011) 816–824. doi:10.1093/cvr/cvq336.

[22] M. Masuda, M. Fujita, O. Iida, S. Okamoto, T. Ishihara, K. Nanto, T. Kanda, A. Sunaga, T. Tsujimura, Y. Matsuda, T. Ohashi, M. Uematsu, Comparison of left atrial voltage between sinus rhythm and atrial fibrillation in association with electrogram waveform., Pacing and Clinical Electrophysiology: PACE 40 (5) (2017) 559–567. doi:10.1111/pace.13051.

[23] N. Kurata, M. Masuda, T. Kanda, M. Asai, O. Iida, S. Okamoto, T. Ishihara, K. Nanto, T. Tsujimura, Y. Matsuda, Y. Hata, H. Uematsu, T. Mano, Left atrial localized low-voltage areas indicate whole left atrial electrophysiological degeneration in atrial fibrillation patients, Circulation Journal 86 (2) (2022) 192–199. doi:10.1253/circj.CJ-21-0527.

[24] N. Qureshi, S. Kim, C. Cantwell, others., Voltage during atrial fibrillation is superior to voltage during sinus rhythm in localizing areas of delayed enhancement on magnetic resonance imaging: An assessment of the posterior left atrium in patients with persistent atrial fibrillation., Heart Rhythm 16 (9) (2019) 1357–1367. doi:10.1016/j.hrthm.2019.05.032.

[25] J. Sánchez, M. Nothstein, L. Unger, et al., Influence of fibrotic tissue arrangement on intracardiac electrograms during persistent atrial fibrilla-

tion, in: Computing in Cardiology conference (CinC), Vol. 46, 2019. doi:10.22489/CinC.2019.342.

[26] J. Sánchez, G. Luongo, M. Nothstein, L. A. Unger, J. Saiz, B. Trenor, A. Luik, O. Dössel, A. Loewe, Using machine learning to characterize atrial fibrotic substrate from intracardiac signals with a hybrid in silico and in vivo dataset, Frontiers in Physiology 12 (2021) 699291. doi:10.3389/fphys.2021.699291.

[27] E. Vigmond, A. Pashaei, S. Amraoui, et al., Percolation as a mechanism to explain atrial fractionated electrograms and reentry in a fibrosis model based on imaging data, Heart Rhythm 13 (7) (2016) 1536–1543. doi:10.1016/j.hrthm.2016.03.019.

[28] N. F. Marrouche, T. Greene, J. M. Dean, et al., Efficacy of LGE-MRI-guided fibrosis ablation versus conventional catheter ablation of atrial fibrillation: The DECAAF II trial: Study design, Journal of Cardiovascular Electrophysiology 32 (4) (2021) 916–924. doi:10.1111/jce.14957.

[29] V. Jacquemet, N. Virag, Z. Ihara, L. Dang, O. Blanc, S. Zozor, J.-M. Vesin, L. Kappenberger, C. Henriquez, Study of unipolar electrogram morphology in a computer model of atrial fibrillation, Journal of Cardiovascular Electrophysiology 14 (s10) (2003) S172–S179. doi:10.1046/j.1540.8167.90308.x.

[30] Y.-k. Iwasaki, K. Nishida, T. Kato, S. Nattel, Atrial fibrillation pathophysiology, Circulation 124 (20) (2011) 2264–2274. doi:10.1161/CIRCULATIONAHA.111.019893.

5.2 AF Voltage Calculation Techniques

Comparison of Voltage Map Calculation Methods Using Non-Fractionated EGM Signals in a Persistent AF Patient

Deborah Nairn[1], Heiko Lehrmann[2], Amir Jadidi[2], Olaf Dössel[1], Axel Loewe[1]

[1] Institute of Biomedical Engineering, Karlsruhe Institute of Technology (KIT), Karlsruhe, Germany
[2] Universitäts-Herzzentrum Bad Krozingen, Bad Krozingen, Germany

Abstract

Catheter ablation targeting low voltage areas (LVA) is commonly being used to treat atrial fibrillation (AF) in patients with persistent AF. However, it is not always certain that the areas marked as low voltage (LV) are correct. This can be related to how the voltage is calculated. Therefore, this paper focuses on comparing different calculation methods, specifically, with regards to spatial distribution.

Two voltage maps obtained in AF were used, removing points which did not meet the required specifications. The peaks for the remaining points, in regions of the left atrium, were then found and the voltage was calculated based on taking the peak to peak (p2p) for different beats.

For around 30% of the points on the map, the voltage only changed by 0.1mV when taking one beat versus all beats. However, for some individual points, the difference was substantial, around 0.8mV, depending on the beat chosen. Additionally, the inter-method variability increased by around 0.1mV when considering all methods compared to only methods calculated using more than one point.

It was found that taking the median over all p2p values in each point would be a more appropriate method for calculating the voltage. Thus, providing a technique, which could improve the accuracy of identifying LVA in an AF map.

1. Introduction

Atrial fibrillation (AF) is a common cardiac arrhythmia characterised by an irregular heart rhythm, which can cause various complications such as heart failure and stroke [1]. It is therefore very important to treat this arrhythmia. One technique is pulmonary vein isolation, which has become widely used to provide freedom from AF, especially in paroxysmal AF [2, 3]. However, in persistent AF this technique alone is not always successful, with variation occurring between patient success rates [4]. It has been seen in many studies, that additionally targeting low voltage areas (LVA) can significantly improve the outcome of ablation [5–7]. Currently, work is being done to correlate the voltage maps between sinus rhythm (SR) and AF [8]. However, with the noise and irregular rhythm that is associated with AF, it remains unclear if the voltage provided in the map has been calculated robustly. Therefore, it must be determined whether there exists an appropriate method for voltage calculation to accurately locate the areas of LV.

In this paper, it will be investigated how different calculations methods relate to one another. Specifically assessing the difference in voltage when only one beat in the bipolar signal is used in comparison to the whole signal. Additionally, ten regions of the left atrium will be analysed to understand whether inter-method variability may be region-dependent.

2. Methods

For this study, 2.5 sec electrocardiogram (ECG) and bipolar electrogram (EGM) signals were provided by the CARTO3 system, allowing the voltage to be calculated in different ways on each point of the induced AF map. To ensure the accuracy of the data being used, certain considerations were made to determine which points would be analysed. This consisted of using the tissue proximity indicator on CARTO to ensure that all points included in the analysis were obtained with sufficient contact to the tissue.

Prior to calculating the voltage for each point, the QRS area in the corresponding ECG was identified. Therefore, the voltage is only calculated on beats in a window before the QRS complex to ensure information from the ventricles was not included. Using a similar approach to the Pan-Tompkin's QRS detection algorithm, zero crossings of the derived ECG and a template matching algorithm, the QRS area was identified [9].

The peaks used for the voltage were then found in these windows, based again on the Pan Tompkin's algorithm which instead of the differentiation, squaring and moving-window integration used a Non-Linear Energy Operator (NLEO) and a Gaussian Lowpass filter [10]. Additionally, points on the map in which no peak was found with an amplitude over 0.05mV were removed from the analysis as the signals appeared to be very noisy. Moreover, if the time stamp indicated that the catheter was moved during the 2.5 sec signal, a part of the signal was removed to avoid problems due to motion artefact.

Furthermore, as it is not easy to determine which peaks should be used for evaluation in fractionated signals, the complex fractionated atrial electrograms (CFE) mean was calculated for each point, using a similar method to that of NavX. All signals with a CFE mean $<$ 80 ms were then considered as continuously fractionated and removed from the analysis [11].

The voltage provided by CARTO was obtained by taking the peak to peak (p2p) value (local maximum - local minimum) of one beat. Although this seems adequate for SR since there is not a lot of variation in the signal, it is important to identify if this is also the case in AF. Therefore, for each point, the mean and median over all the p2p values of the signal were calculated, to allow a direct comparison between taking the whole signal and taking only one beat. Moreover, to further examine how the voltage values change with different methods, the maximum and minimum of the p2p values were also calculated. The 75th percentile of the p2p beats was also taken to identify a method which would give the voltage calculated on beats with higher amplitudes but without including the outliers, like the max and min. Finally, the points of the left atrium were separated into ten regions by k-means clustering to correlate the voltage with its spatial distribution.

3. Results

Two patients in persistent AF undergoing their first ablation were used for this study, with a total of 4241 and 2436 mapping points, respectively. After the removal of the points which did not meet the criteria, as mentioned above, 3076 and 1223 were left for analysis.

When assessing the voltage values at different points, it was seen that calculating the voltage on one beat can give very different values to using the same way but over all beats. In Figure 1, this can be seen in the form of a bar chart, where the voltage is calculated using the different p2p methods described above. Each of the first four bars are calculated using only one beat, the following two bars are then calculated by taking the mean and median over the four p2p values. Finally, the last bar is the value provided by the CARTO system which was also calculated from p2p over one beat.

To further understand the values being provided in the bar chart, the 2.5 sec signal of that point can be seen in Figure 2, with the QRS regions set to zero, so that the areas which were used for analysis are more defined.

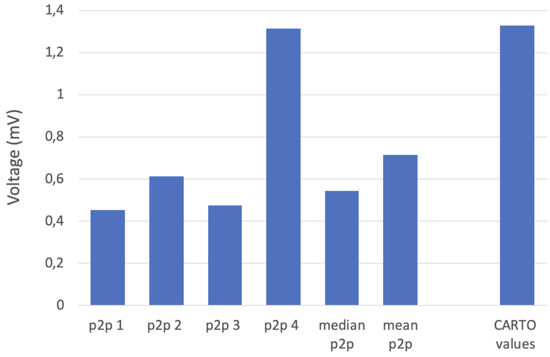

Figure 1. Bar chart showing the voltage calculated for one point in one of the maps with different beats of the signal

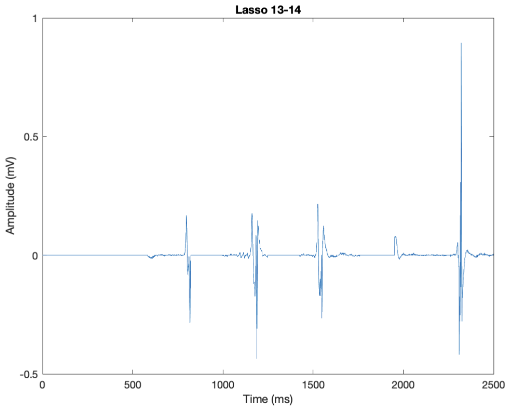

Figure 2. (2.5 sec signal of the same point on the map, as in Figure 1, with the information in the QRS region set to 0

It can be seen by the first figure that taking only one beat to calculate the voltage can give a significantly different value than if the voltage was calculated over all the beats. However, it must be assessed if this is true for all points on both maps. Therefore, for each method mentioned above, the mean and standard deviation of the voltage values were calculated over all points. Additionally, the absolute difference between each method and the median p2p method for each point was calculated and the mean was taken over all points. Figure 3 shows a bar chart where the bars represent the mean value of the voltage and absolute difference for each method and the error bars represent the standard deviation.

When comparing the median and CARTO value in Figure 2 a difference of 0.8mV is seen. However, in Figure 3 there is an average difference of 0.2/0.3mV. Therefore, it can be seen that the situation for that one point is not the situation for all points but in general a change is occurring when calculating the voltage using only one beat.

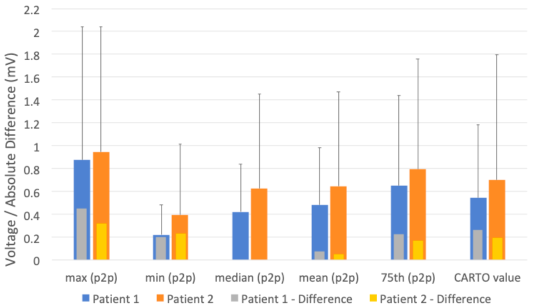

Figure 3. Bar chart with error bars showing the mean and standard deviation of the voltage value and the absolute difference between each method and the median p2p value for both patients

This is further verified by all the methods having an average difference of around 0.2mV except the mean p2p when compared to the median.

To assess more clearly how many points have a similar voltage when calculated with median p2p to that of the CARTO value, Table 1 was created. This shows that when comparing the voltage calculated by the median p2p, around 30% of points were in a 0.1mV range from the CARTO value. Although 0.1mV does not seem a substantial difference, areas which were classed as LVA may no longer be, or vice versa. The columns Max and Min present the same results but instead of comparing the median with the CARTO value, they are compared with the max p2p and min p2p values respectively. The percentage of points with similar values to the median p2p appears lower than with the CARTO value, with around 21.5% of points having a 0.1mV difference between the median p2p and the max p2p.

Table 1. Percentage of points for which the absolute difference in voltage values between using one beat and the whole signal is less than the difference given

Comparison	Patient 1			Patient 2		
Difference (mV)	CARTO	Max	Min	CARTO	Max	Min
0	23 %	22%	22%	31 %	25%	26%
0.1	31 %	21%	25%	29 %	22%	26%
0.2	17 %	13%	17%	15 %	13%	13%
0.3	8 %	10%	12%	9 %	10%	10%

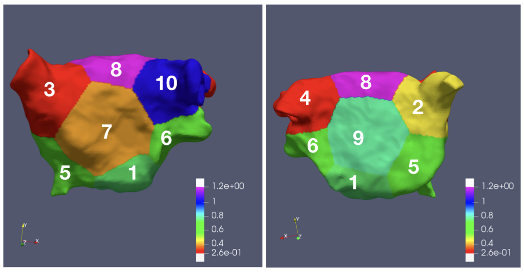

Figure 4. Image showing the left atrium split into ten sections with the average median voltage given for each section

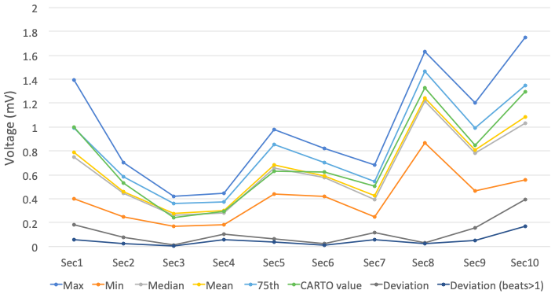

Figure 5. Line graph showing the average voltage for each section and method and the standard deviation between methods

In Figure 4 the same methods for calculating the voltage are analysed, with the added aspect of looking at the spatial distribution. The left atrium was split into ten sections for both patients and the average median voltage for each section of patient 2 are shown. The line graph in Figure 5 then shows the average voltage in each section for the different calculation methods for the same patient. Additionally, the standard deviation between the methods for each section is given, along with the standard deviation between only methods where more than one beat was used for the calculation.

From Figure 5 it can be seen that the voltage is changing depending on which area of the atrium is being looked at, which can be due to the thickness of the tissue or areas of diseased tissue. However, the variation between methods remains relatively constant between sections, except for the CARTO method which causes most of the variation in the deviation line. When considering the variation between only methods calculated using more than one beat, the average standard deviation is 0.05mV, which raises to 0.13mV when all methods are included. Patient 1 also shows similar results with an increase of 0.1 mV between calculating the variation of all methods and just methods calculated with more than one beat.

4. Discussion

Currently, the voltage is calculated based on taking the p2p value of one beat of the signal for each point. This along with a threshold is then used to determine the LVA. Therefore, the question arose, if one beat is sufficient to calculate the voltage or if all the beats within the measured time segment should be used. From the results, it can be seen that taking one beat can be sufficient but it depends on which beat is taken, for example using the max or min p2p values may have outliers and not give a true representation of the voltage at that point. Additionally, the same situation may occur when using the 75th percentile method, if the number of beats used is too small. For the CARTO method, only 30% of points had voltage values in a range of 0.1mV compared to the median. Therefore, showing that there may be many points in which an outlier beat may have been taken.

Additionally, the atrium was split into ten sections to further look at the inter-method variability with respect to the regions. For methods calculated with more than one beat, the variability was low, for most sections. However, the max and min method shows more variation between regions, which can be due to outliers being taken. The CARTO method shows the most variability, having an average voltage similar to that of the median method in some sections and the 75th percentile method in others. This indicates that it may not always be providing a true value for the voltage, rather choosing sometimes the outliers and others a peak which better represents the signal.

It can be seen that calculating the voltage based on taking a method which does not only take one beat could be a more appropriate method. However, a further investigation must be carried out on how the areas change on the map in regards to being classified as low/high voltage points with these new methods and if they can provide a higher correlation between voltage maps in SR and AF. Additionally, since only two patient were used for the analysis, it is unknown if these results are representative of all patients.

5. Conclusion

In this study, different methods for calculating the voltage were used and compared. It was seen that using a method which considers all beats within the measured time window rather than just one beat can give a better representation of the signal at each point. Additionally, there is little inter-variability between these methods for different regions of the atrium. Based on this study, it has been found that using the median p2p method can provide an appropriate way to calculate the voltage which can help to correctly identify LVA in the map.

Acknowledgments

We gratefully acknowledge financial support by Deutsche Forschungsgemeinschaft (DFG) through DO637/22-3 and by the Ministerium für Wissenschaft, Forschung und Kunst Baden-Württemberg through the Research Seed Capital (RiSC) program

References

[1] Miyasaka Y, et al. Time trends of ischemic stroke incidence and mortality in patients diagnosed with first atrial fibrillation in 1980 to 2000: report of a community-based study. Stroke a Journal of Cerebral Circulation 2005;36(11):2362–2366.

[2] Oral H, et al. Pulmonary vein isolation for paroxysmal and persistent atrial fibrillation. Circulation 2002;105(9):1077–1081.

[3] Verma A, et al. Pre-existent left atrial scarring in patients undergoing pulmonary vein antrum isolation: an independent predictor of procedural failure. Journal of the American College of Cardiology 2005;45(2):285–292.

[4] Magnani S, et al. Adjunct ablation strategies for persistent atrial fibrillation-beyond pulmonary vein isolation. Journal of Thoracic Disease 2015;7(2):178–184.

[5] Rolf S, et al. Tailored atrial substrate modification based on low-voltage areas in catheter ablation of atrial fibrillation. Circulation Arrhythmia and electrophysiology 2014; 7(5):825–33.

[6] Blandino A, et al. Left atrial substrate modification targeting low-voltage areas for catheter ablation of atrial fibrillation: A systematic review and meta-analysis. Pacing and clinical electrophysiology PACE 2017;40(2):199–212.

[7] Ammar-Busch S, et al. Predictors of low voltage areas in persistent atrial fibrillation: is it really a matter of time? Journal of interventional cardiac electrophysiology an international journal of arrhythmias and pacing 2018;.

[8] Rodríguez-Mañero M, et al. Validating left atrial low voltage areas during atrial fibrillation and atrial flutter using multielectrode automated electroanatomic mapping. JACC Clinical Electrophysiology 2018;4(12):1541–1552.

[9] Pan J, Tompkins WJ. A real-time QRS detection algorithm. IEEE Transactions on Biomedical Engineering 1985; 32(3):230–236.

[10] Nguyen M, et al. A new approach for automated location of active segments in intracardiac electrograms. IFMBE Proceedings World Congress on Medical Physics and Biomedical Engineering 2009;25/4:763–766.

[11] Jadidi A, et al. Inverse relationship between fractionated electrograms and atrial fibrosis in persistent atrial fibrillation: combined magnetic resonance imaging and high-density mapping. Journal of the American College of Cardiology 1 2013;62(9):802–812.

Address for correspondence:

Deborah Nairn
Institute of Biomedical Engineering, Karlsruhe Institute of Technology (KIT), Fritz-Haber-Weg 1, 76131 Karlsruhe, Germany
publications@ibt.kit.edu

5.3 Comparability to SR

This section partially contains the work performed in a master thesis which aimed at comparing SR and AF voltage maps with different voltage calculation methods in AF [90]. Within the master thesis, a technique was developed to determine the reliability of a detected peak by assessing the characteristics of a segment surrounding the peak. If the detected peaks were sharp and clear with no surrounding variations in the segment, they would have a very high-reliability score. The work then used peaks deemed reliable to calculate the voltage for each signal in various ways, as described below. The results of comparing these voltage calculation techniques to SR are presented in this section. Using the predefined reliable peaks of the master thesis, the work was continued to gain a deeper insight into the variability of the signals when recorded during AF. This was done by calculating the sample entropy of the signal and the standard deviation across all peak-to-peak values.

5.3.1 Methods

Forty-one patients undergoing high-density mapping using the CARTO-3 mapping system (Biosense Webster, Diamond Bar, CA, USA) and 20-pole Lasso-Nav catheter (electrode size: 1 mm; spacing: 2-6-2 mm) were used for this study. For each catheter position in the left atria, 19 bipolar EGMs were collected. EGMs, where the electrodes were > 7 mm away from the tissue were removed. The voltage determined by the CARTO-3 system was provided, in which it calculates the local maximum - local minimum of one atrial beat at time x. EGMs were then provided for the 2 s before and 0.5 s after x.

Atrial activity was then detected in the 2.5 s signals using the NLEO [91]. Peaks detected in one atrial activity segment which were considered as (1) unreliable, as defined in [90], (2) had an amplitude < 0.05 mV, and (3) within the QRS window were removed from further analysis. The signal's first and last 250 ms were also excluded to avoid movement artefact detection.

The irregular rhythm of AF leads to the question of whether using only one atrial beat is a robust method for calculating the voltage during AF. The voltage (peak-to-peak (p2p) amplitude) was then determined using the remaining peaks detected in one EGM. Therefore, the voltage for one signal was additionally calculated as the 25th percentile, median, mean, 75th percentile and max over all p2p values. The standard deviation was then calculated across all p2p values in each signal, to assess how much variability exists in each signal. Aside from the voltage the sample entropy has been shown to indicate location of fibrotic tissue, as it captures irregularities in the signal. The sample entropy was calculated as $SampEn = -log\frac{A}{B}$, where A is the number of pairs having distance $d[X_{m+1}(i), X_{m+1}(j)] < r$ and B pairs having distance $d[X_m(i), X_m(j)] < r$, $(i \neq j)$ with $m = 2$ and $r = 0.2 \cdot std$, as applied in literature [92].

To evaluate which method provides the highest correlation between the voltage maps in SR and AF, an ROC curve was built. The SR map (low voltage areas (<0.5 mV)) was considered the “true condition” and the electrogram at each point of the AF map (with the different voltage calculation methods and the entropy measure) were classified depending on the AF threshold. For each new method, it could then be observed what AF threshold would need to be used to obtain the best match.

5.3.2 Results

Figure 5.1 shows the standard deviation, for all signals and all patients, calculated across all voltage values within one signal. The standard deviation values are generally low (IQR: 0.05-0.25 mV), implying that very little change occurs within the signal. However, the voltage values of each beat can substantially differ with standard deviation values between 0.5-4 mV. By examining the patients separately (shown as two examples in the middle column), it can be identified that the outliers (standard deviation > 0.5 mV) occur in about 8% of signals in one patient. Therefore, these 8% of signals would be greatly impacted by which voltage calculation technique is applied. Examining the unipolar and bipolar signal examples with high standard deviations in figure 5.1 and figure 5.2, the variation in the bipolar signal can either be due to a substantial change in both unipolar signals or just one electrode.

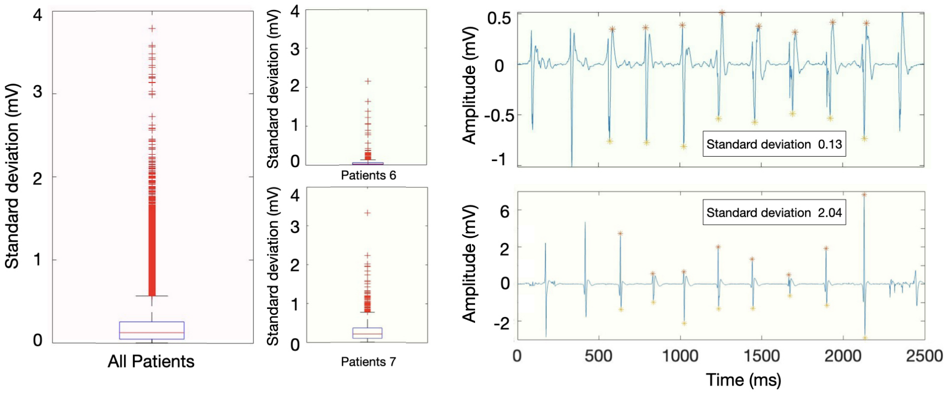

Figure 5.1: Boxplot showing the standard deviation of the voltages calculated in one signal. On the left shows the standard deviation values for all signals of all patient. In the middle, two example patients are shown and on the right, a corresponding bipolar signal for each patient.

Comparing each method applied to the signals in AF to the voltage in SR reveals that using the maximum voltage of the signal provides the best relation (AUC: 0.76), figure 5.3. However, for each method to obtain the optimal compromise between sensitivity and specificity, a different threshold needs to be applied. When using the maximum p2p amplitude of the signal (0.67 mV) is needed to be applied.

By examining an example patient where the previously defined thresholds are applied, matching areas for voltage and sample entropy can be identified (figure 5.4). It is interesting to observe that while some areas are related to high voltage and low entropy (marked with

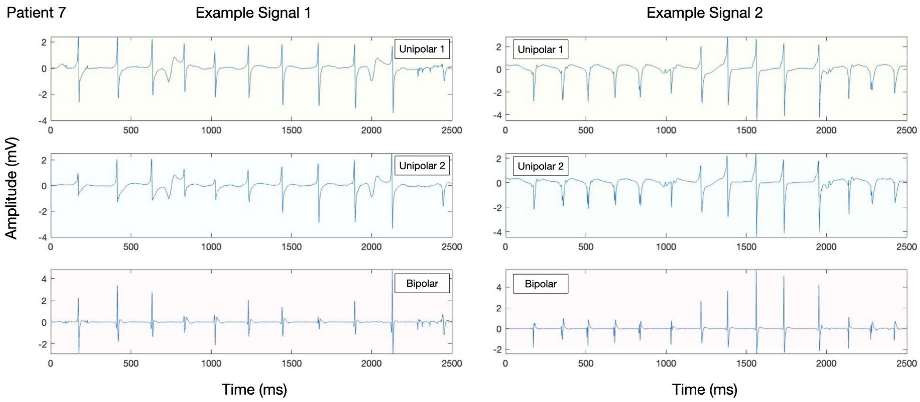

Figure 5.2: Example unipolar and bipolar signals for high standard deviation values. On the left the unipolar and bipolar signals for the example signal in figure 5.1 are shown. On the right, an additional example of a high standard deviation bipolar signal and the corresponding unipolar signals are shown.

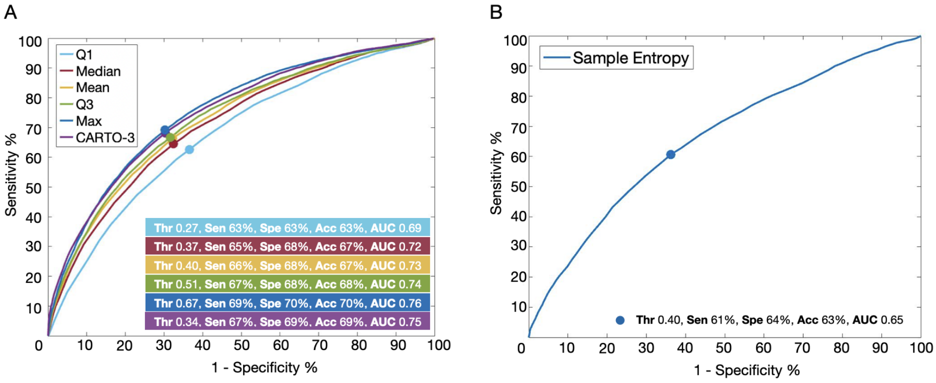

Figure 5.3: ROC curves comparing (A) different voltage calculation methods and (B) sample entropy to SR voltage map. True positive was defined as points with SR < 0.5 mV and AF voltage < a defined threshold or sample entropy > a defined threshold.

star) or low voltage and high entropy (marked with triangle), other regions are discordant, with low voltage and low entropy (or high).

5.3.3 Discussion

Evaluating the signals shown in figure 5.1 and figure 5.2, one could hypothesise that perhaps the signals are affected by multiple wavefronts or collisions, as identified by Jacquement et al. [93]. In this situation, multiple wavefronts could pass near to the electrodes at similar times, reducing or increasing the amplitude depending on the direction of the waves. It is clear that by only taking one beat of the signal, the information about the substrate below the electrode could be missed depending on how the waves are reacting. However, this could also be the case for other voltage calculation methods. Additionally, using the

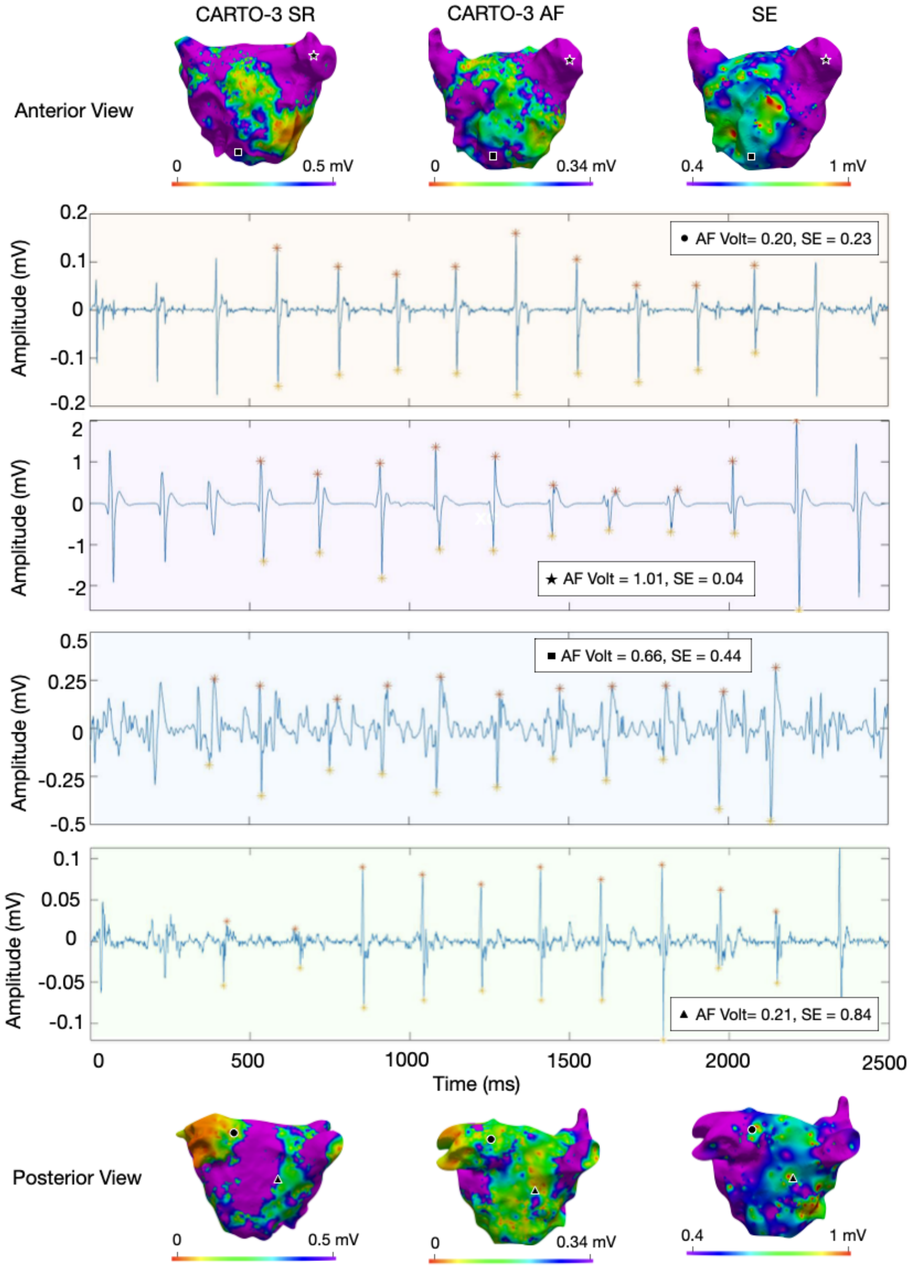

Figure 5.4: Spatial distribution of voltage and entropy in AF in one patient. The top and bottom rows show the CARTO-3 SR and AF voltage map and AF sample entropy (SE) map anterior and posterior view. The geometric shapes represent the spatial points on the atrial geometry for which the corresponding signals are shown in the middle rows.

sample entropy, which identifies complexity in signals, can help identify regions that need further investigation, as seen by figure 5.4 (signal marked with a square), where the tissue is defined as healthy by the voltage. However, there is a high sample entropy and the signal is fractionated, implying that some phenomena may be occurring below the electrode affecting the signal.

The entropy could also help distinguish different types of fibrosis. One hypothesis is that in dense fibrotic tissue, the variation in the signal would be reduced due to the block in conduction. On the other hand, in patchy fibrosis, the effect of the complex propagation would be more prominent. Thus, the entropy would be high (as seen with the signal marked with a triangle). Therefore, looking at the variation (sample entropy) within one signal may help identify areas of interest that require further investigation to understand the phenomena taking place below the catheter.

By examining the unipolar signals of another example signal in figure 5.2 right column, it appears that perhaps the catheter may have moved location during the signal acquisition. At the beginning of the signal, it appears as if the catheter is above pathological substrate (due to the fractionated, non-symmetric signals) and later moved over healthy tissue (where signals are clear). In such situations, only taking one peak when the catheter has stopped moving would be optimal, as the CARTO-3 system does. Therefore, leading to a higher correlation when compared to SR. Since large variations in the signals only occur about 8% of the time and not all of them are due to catheter movement, it is assumed that this does not substantially hinder the analysis. However, further investigation using longer signals where it can be ensured that the catheter stays in one position for the entire time should be performed.

When comparing AF voltage calculation techniques to identify areas of LVS as defined in SR ($< 0.5\,\mathrm{mV}$), using the maximum voltage is optimal. However, the accuracy is only 1% higher than calculating the voltage on just one atrial beat as the CARTO-3 system does. One assumption is that the maximum voltage value of the signal corresponds to the point when the electrode is closest to the tissue and, therefore, not as much affected by far-field effects [94]. Additionally, if the catheter is slightly rotated during the acquisition of the signal, the maximum of the signal would be less likely to the point when the electrode pair is perpendicular to the wavefront, as seen in section 4.2.

Chapter **6**

Multi-Modality Identification of Atrial Cardiomyopathy

A further modality for the detection of atrial pathological substrate associated with atrial cardiomyopathy (ACM) is the localisation of areas with high LGE-MRI contrast [31, 42, 95]. The technique has the advantage of being less invasive than electro-anatomical mapping and could improve the planning of the AF ablation procedure [27] by indicating regions of interest for the physician to guide the electrophysiological mapping procedure and providing information on the optimal procedure option [28]. However, the spatial resolution of LGE-MRI is limited to 1.25x1.25x2.5 mm, which is above the thickness of the thin-walled LA (0.5-3 mm) [96, 97].

Additionally, computational studies have shown how fibrotic tissue can affect the conduction velocity. For example, patchy fibrosis can slow the conduction velocity due to the separation of myocardial bundles, creating blocks and resulting in local reentrant sources, known for AF maintenance [33]. During electro-anatomical mapping, delayed activity has been seen in the bipolar signals in SR [21]. Therefore, besides low voltage, slow conduction sites in SR are another potential indicator of atrial fibrosis.

While LGE-MRI and voltage mapping have been shown to identify fibrotic regions in the atria, the correlation between these two modalities is unsatisfactorily low. Using a spatial frequency histogram of LGE, Higuchi et al. found that 60% of their patients showed enhancement on the posterior wall [98]. In contrast, low voltage areas are located most frequently on the anterior wall of the LA [99].

In the study presented in this chapter, the location and extent of pathological substrate is compared between different modalities currently applied in clinical practice (voltage, conduction velocity and LGE-MRI). In this work (the currently submitted journal manuscript/ pre-print paper [100]) a spatial histogram for each mapping modality was created to assess which areas most commonly exhibit pathological substrate. In all modalities pathological substrate was located on the anterior wall in around 20-40% of patients depending on the modality (22% LVS < 0.5 mV, 22% MRI image intensity ratio > 1.2, 25% MRI Utah method, 31% CV < 0.2 m/s). Important discordances, however, were identified in localisation of detected pathological low voltage and LGE-MRI areas, specifically on the posterior wall. To combat these discrepancies, a new thresholding method for the LGE-MRI to identify patients with ACM was developed. Using the newly provided linear equation and the patients' mean MRI blood-pool value, patients with LGE-extent $> 13\%$ on the anterior wall could identify patients with ACM (LVS extent $\geq 5\%$). Therefore, the new thresholding method enabled a more accurate (sensitivity: 83%, specificity: 88% and AUC: 0.94) LGE-MRI-based ACM diagnosis in AF patients.

The work presented in this chapter provides a spatial histogram of low-voltage and slow conduction areas for the first time, which can help guide clinicians during the mapping procedure. Additionally, the new LGE-MRI thresholding method can provide a deeper insight into whether PVI would be sufficient or if the entire atrium should be mapped during the procedure, thus, providing a way to aid in treatment planning and reduce the procedure time during catheter mapping and ablation.

Discrepancy Between LGE-MRI, Electrogram Voltage and Conduction Velocity for Detecting Left Atrial Fibrotic Substrate

Deborah Nairn, MSc[1*#], Martin Eichenlaub, MD[2#], Björn Müller-Edenborn, MD[2], Heiko Lehrmann, MD[2], Claudia Nagel, MSc[1], Luca Azzolin, PhD[1], Giorgio Luongo, PhD[1], Rosa M. Figueras Ventura, PhD[3], Barbara Rubio Forcada, MSc[3], Anna Vallès Colomer, MSc[3], Thomas Arentz, MD[2], Olaf Dössel, PhD[1], Axel Loewe, PhD[1§] and Amir Jadidi, MD[2§]

[1]*Institute of Biomedical Engineering, Karlsruhe Institute of Technology, Karlsruhe, Germany*
[2]*Department of Electrophysiology, University-Heart-Center Freiburg-Bad Krozingen, Bad Krozingen, Germany*
[3]*Adas 3D Medical SL, Carrer Paris 179, Barcelona, Spain*

[#],[§] *These authors contributed equally.*

Short title: *LGE-MRI for diagnosis of left atrial cardiomyopathy*

Address for correspondence: *Deborah Nairn, MSc, Fritz-Haber-Weg 1, 76131 Karlsruhe, Germany, publications@ibt.kit.edu*

Conflict of Interest Statement: *RF, BF and AC are employees of Adas 3D Medical. This investigator-initiated study was financially supported by Medtronic. Medtronic had no influence on collection, analysis and interpretation of data, in the writing of the report, and in the decision to submit the article for publication.*

Abstract

Background: Electro-anatomical voltage or conduction velocity (CV) mapping and late-gadolinium-enhancement magnetic-resonance-imaging (LGE-MRI) have been correlated with atrial cardiomyopathy (ACM). However, discordances between these modalities exist.

Objectives: (1) Comparison of pathological substrate extent and location between current modalities. (2) Development of new estimated optimised image-intensity-thresholds (EOIIT) for LGE-MRI identifying patients with ACM.

Methods: Thirty-six ablation-naive persistent AF patients underwent LGE-MRI and high-definition electro-anatomical mapping in sinus rhythm. Significant ACM was defined as low voltage substrate (LVS) extent≥5% of the left atrium (LA) surface at <0.5 mV. LGE areas were classified using the Utah, image-intensity-ratio (IIR>1.20) and new EOIIT method for comparison to LVS and slow conduction areas <0.2 m/s. ROC-analysis determined the LGE-extent enabling accurate diagnosis of ACM.

Results: The degree and distribution of detected pathological substrate varied significantly (p<0.001) across the mapping modalities: 3% (IQR 0-12%) of the LA displayed LVS<0.5 mV vs. 14% (3-25%) slow conduction areas<0.2 m/s vs. 16% (6-32%) LGE with Utah method vs. 17%(11-24%) using IIR>1.20, with enhanced discrepancies on posterior LA. A linear correlation was found between the optimised image-intensity-thresholds and each patient's mean blood pool intensity (R^2=0.89, p<0.001). LGE-MRI-based ACM-diagnosis improved with the novel EOIIT (83% sensitivity, 88% specificity, AUC:0.94) in comparison to the Utah method (60% sensitivity, 75% specificity, AUC:0.76), and IIR>1.20 (58%

sensitivity, 75% specificity, AUC:0.71)

Conclusion: Important discordances in distribution of pathological substrate exist between LA-LVS, CV and LGE-MRI, irrespective of the LGE-detection protocol that is used. However, the new EOIIT method improves LGE-MRI-based ACM diagnosis in ablation-naive AF patients.

Key Words: Atrial fibrillation, LGE-MRI, Electro-anatomical mapping, Conduction velocity, Pathological substrate.

Condensed Abstract: Significant discordances exist between different mapping modalities (electro-anatomical voltage mapping, late-gadolinium enhancement magnetic resonance imaging (LGE-MRI) and conduction velocity mapping) to detect pathological substrate in the left atrium. We compared location and extent of pathological substrate between modalities in 36 ablation-naive persistent atrial fibrillation patients. Most important discordances in substrate location and extent were found at posterior LA. A new estimated optimised image-intensity-threshold (EOIIT) for LGE-MRI was developed, improving LGE-MRI based atrial cardiomyopathy diagnosis in ablation-naive AF patients (AUC: 0.94). EOIIT-based LGE-MRI provides a non-invasive approach that can aid procedure planning by identifying the extra-pulmonary-vein substrate.

List of Acronyms:

LGE-MRI	late gadolinium-enhancement magnetic resonance imaging
AF	atrial fibrillation
EOIIT	estimated optimised image intensity thresholds
ACM	atrial cardiomyopathy
CV	conduction velocity
LVS	low voltage substrate
ROC	receiver operating characteristic
IQR	interquartile range
IIR	image intensity ratio
AUC	area under curve
PVI	pulmonary vein isolation
EAM	electro-anatomical mapping
SR	sinus rhythm

1. Introduction

Atrial fibrillation (AF) is the most common cardiac arrhythmia causing an irregular heart rhythm, associated with increased risk for stroke and heart failure [1]. Pulmonary vein isolation (PVI) is a commonly used treatment for AF with a high success rate (75-90%) in paroxysmal AF patients [2]. However, persistent AF patients may present atrial cardiomyopathy (ACM) with extra-PV pathological substrate, which contributes to the maintenance of AF and reduces the success rate markedly [3, 4].

Electro-anatomical mapping (EAM) during sinus rhythm (SR) identifying low voltage bipolar electrograms (<0.5 mV) is a common technique used to locate pathological substrate [5, 6]. Conduction velocity (CV) mapping has also been investigated due to the structural and functional abnormalities resulting in conduction slowing [7, 8, 9]. Another commonly used method is late-gadolinium-enhancement magnetic-resonance-imaging (LGE-MRI) [10, 11, 12]. The advantage of LGE-MRI is that it is a non-invasive diagnostic method. However, the spatial resolution of LGE-MRI is limited. Although all the above-mentioned methods detect pathological substrate, discordances in their location and extent have been reported when mapping during AF [13].

This study assessed the spatial distribution of pathological left atrial substrate as detected in LGE-MRI (using various MRI post-processing methods), voltage and CV mapping during sinus rhythm (SR) in ablation-naive AF patients. The mapping modalities were compared to one another. Additionally, a new estimated optimised image-intensity-thresholding method (EOIIT) for LGE-MRI was developed, enabling identification of patients with ACM as diagnosed by low-voltage areas (SR <0.5 mV).

2. Methods

2.1. Electro-anatomical mapping (EAM)

High-density (>1,200 mapped sites per left atrium (LA)) activation and voltage mapping was performed using a 20-polar Lasso-Nav mapping catheter or a PentaRay catheter (electrode size: 1 mm, spacing: 2–6–2 mm). Mapping was conducted while the patient was in SR prior to PVI using the CARTO-3 mapping system (Biosense Webster, Diamond Bar, CA, USA). Further details about the signal processing and calculation of the LAT, voltage and CV can be found in the supplementary material section 1.1. The study was approved by the institutional ethics committee of the University of Freiburg (Germany) and all patients provided written informed consent prior to enrolment.

In two series of analyses, cut-off values of <0.5 and <1.0 mV were applied to the bipolar voltage maps to define the low voltage substrate (LVS) [14, 15]. Additionally, a CV cut-off value was set at 0.2 m/s to indicate pathological slow conducting substrate [16].

2.2. Late gadolinium enhancement magnetic resonance imaging (LGE-MRI)

LGE-MRI was performed on a 3 T scanner (Somatom Skyra, Siemens Healthcare, Erlangen, Germany) as described previously [10, 11]. In brief, LGE-MRI was acquired in SR 15 minutes after contrast injection with a dose of 0.1 mmol Gadoteridol per kg body weight (ProHance®, Bracco, Milan, Italy). Voxel size was 1.25×1.25×2.5 mm (reconstructed to 0.625×0.625×1.25 mm), repetition time was 3.1 ms, echo time was 1.4 ms and flip angle was 14°.

Two independent expert core laboratories performed the LA segmentation and detection of LGE-areas: Merisight (Marrek Inc., Sandy, Utah, USA) for the Utah method and the Adas group (Adas3D Medical SL, Barcelona, Spain) for the ”image-intensity-ratio (IIR)” method by Benito et al. [12]. All image analysts were blinded to any clinical data. Further details about the two methods can be found in the supplementary material section 1.2.

2.3. Analysis

2.3.1. LA mean geometry and statistical analysis of pathological substrate

Geometries obtained from each modality for all patients were aligned to a mean LA shape. Thus, a direct comparison between EAM and LGE-MRI and between patients could be performed without variations caused by spatial displacement. The steps behind this approach are introduced in the supplementary material, section 1.2 and figure S1. Information on the pulmonary veins (PVs) and mitral valve (MV) were excluded from all substrate analyses.

The median value for each point on the geometry across all patients was calculated for the voltage, CV and MRI maps (image-intensity values), providing a visual comparison between mapping modalities without the influence of outliers due to patient-specific differences.

A spatial histogram for each mapping modality was created to assess which areas most commonly exhibit pathological substrate. Providing for the first time a spatial histogram of LVS and slow conduction areas and a comparison of LGE-MRI spatial histograms with the one previously reported by Higuchi et al. [17].

Additionally, a correlation analysis was performed between each pair of mapping modalities identifying the difference in pathological substrate extent for each patient.

2.3.2. Detection of LA LGE-areas based on estimated optimised image intensity thresholding method "EOIIT"

The individual patient's "optimised image-intensity-threshold" was considered as the threshold with best quantitative match between LGE-extent and LVS-extent (<0.5 mV) and plotted against the mean bloodpool value of the LA-LGE-MRI for each patient. A linear correlation was calculated using a leave-one-out cross-validation method to determine the EOIIT method for the entire cohort. This analysis was performed for the (1) entire LA, (2) anterior LA and (3) posterior LA. Details on this semi-automatic segmentation approach are given in the supplementary material section 1.3.

The performance of the new thresholds were then evaluated by examining the relationship between the LVS-extent (<0.5 mV) and LGE-MRI substrate for each MRI post-processing method (Utah, IIR>1.20 and EOIIT). Patients with a LVS-extent ≥5 cm^2 of LA surface corresponding to a LVS-extent of ≥5% at <0.5 mV were classified as having substantial extent of LVS [18].

Reciever operating curves were created for the IIR>1.2 method and the EOIIT method for the entire LA, anterior and posterior. In this way, the most sensitive and specific LGE-extent was determined to detect significant LA-LVS. A fibrotic tissue extent ≥20% of the total LA-wall (Utah-stages III and IV) was classified as relevant LGE for the Utah method [19].

3. Results

3.1. Patient characteristics

Thirty-six patients with persistent AF (66±9 years old, 84% male) underwent EAM and LGE-MRI prior to PVI. All patients were electrically cardioverted

4-6 weeks prior to PVI. Fourteen (39%) patients with AF recurrence were cardioverted again on admission. The supplementary material provides details of the patients' characteristics (Table S1) and EAM and LGE-MRI data (Table S2).

3.2. Spatial distribution of left atrial pathological substrate in electro-anatomical voltage-activation mapping versus LGE-MRI

Figure 1 reveals discrepancies in the distribution and extent of pathological substrate between EAM modalities and LGE-MRI. Both LGE-MRI methods identified extensive pathological substrate on the inferior wall, whereas the electrograms in this area (marked with a square) are non-fractionated signals with high amplitudes. In contrast, low amplitude signals are seen (marked with a circle) where LVS and slow CV were identified. All patient-specific substrate maps are shown in the supplementary material figure S2.

3.3. Spatial distribution of left atrial pathological substrate as identified by median voltage values, conduction velocity and LGE-MRI intensity

Figure 2 reveals notable differences in the median voltages between the anterior (median 1.22 mV, IQR 1.05-1.46 mV) and posterior wall (median 1.58 mV, IQR 1.34-1.90 mV). The CV shows similar differences although less pronounced (anterior: median 0.27 m/s, IQR 0.25-0.29 m/s and posterior: median 0.33 m/s, IQR 0.31-0.35 m/s). On the other hand, the LGE-MRI IIR method reveal relatively little difference between the anterior and posterior wall, with median IIR values 0.98 (IQ3 0.96-1.11) and 0.99 (IQ3 0.90-1.12), respectively, signifying more pathologically enhanced tissue at posterior LA.

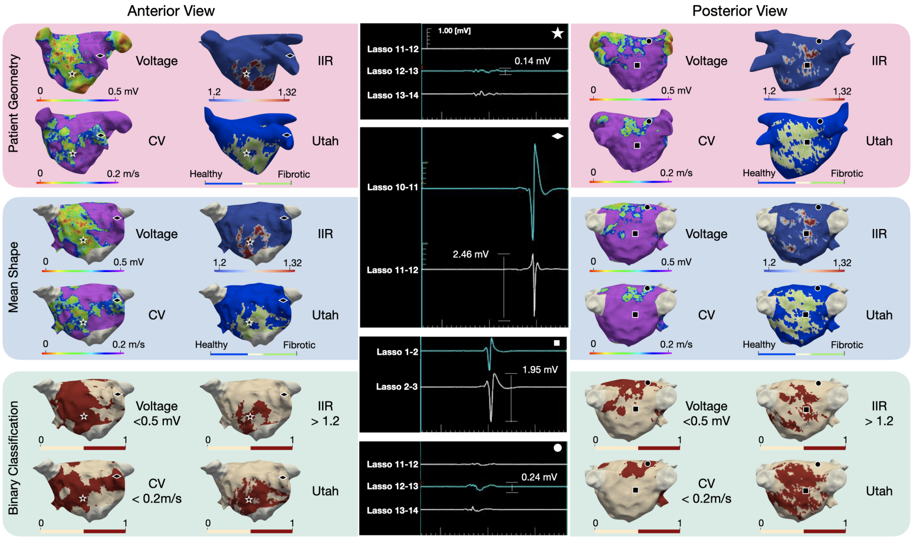

Figure 1: **Three-dimensional distribution of voltage <0.5 mV, CV <0.2 m/s and LGE-areas detected with IIR 1.2-1.32 and the Utah method in a representative patient.** The top and middle row show the EAM and LGE-MRI information on the patient's geometry and the mean shape, respectively. The bottom row shows a binary classification, where pathological substrate is shown in red and healthy tissue in cream. Each geometric shape represents a point on the map where the corresponding electrogram is shown in the middle column.

3.4. Spatial localisation frequency of atrial sites displaying pathological substrate

Figure 3 shows that the highest probability for LGE-MRI areas was found around the left inferior PV (with the UTAH method median 56% and IIR>1.20 44% of the patients). In contrast, the LVS <0.5 mV spatial histogram rarely (8% of patients) indicated pathological substrate on posterior wall. Evaluating LVS <1 mV and CV <0.2 mV, the percentage of patients with pathological substrate

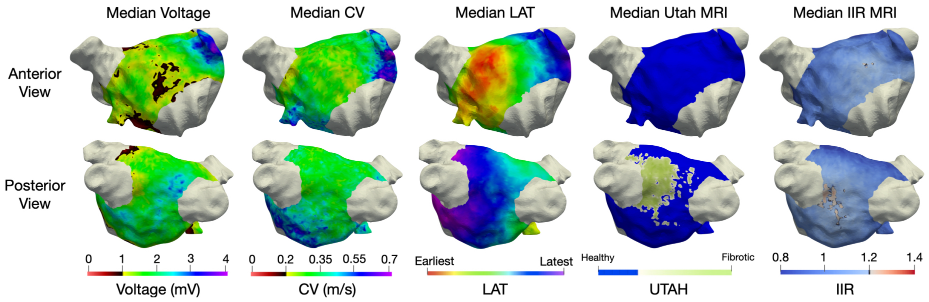

Figure 2: **Spatial distribution of the pathological substrate as detected by the different mapping modalities.** Each column shows the median values of total study cohort on a representative LA geometry of the mapping modality mentioned at the head of the column.

for both methods was 28% adjacent to the left inferior PV. All methods identified a similar percentage of patients with pathological substrate on the anterior wall (22% LVS <0.5 mV, 22% IIR>1.2, 25% UTAH, 31% CV< 0.2 m/s, 42% LVS < 1 mV).

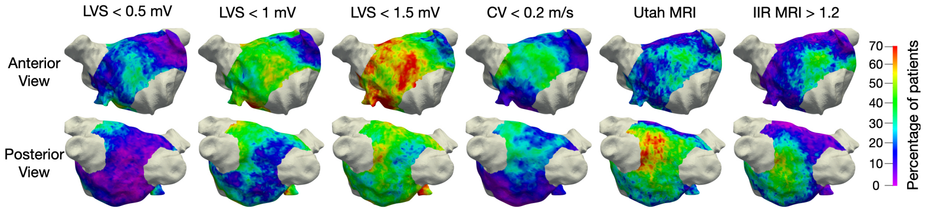

Figure 3: **Spatial histogram of left atrial pathological substrate.** The colour indicates the percentage of patients for which the respective method identified pathological substrate at the specific location. Each column shows the spatial histogram of the mapping modality mentioned at the top.

3.5. Quantification of left atrial pathological substrate.

Figure 4 reveals that the lowest difference in terms of global pathological LA substrate extent was found for LVS <0.5 mV and CV <0.2 m/s (median difference 6%) and LGE-extent assessed with IIR >1.2 and UTAH (11%). When comparing LVS <0.5 mV and the LGE-extent with UTAH method, the difference of globally detected substrate was relatively low (median difference 10% of the LA surface; range from 0 to 25%). While both methods detected a similar total extent of pathological LA substrate, the location of detected substrate differed importantly between the methods (see supplementary material figure S2).

3.6. Optimising the LGE-MRI threshold to identify low-voltage substrate

The "optimised-image-intensity-threshold" was reported to each patient's left atrial mean bloodpool intensity value (figure 5). For the entire LA, anterior and posterior wall, the linear relationship can be described as $y = 0.97x + 86$ ($R^2 = 0.88$), $y = 0.96x + 72$ ($R^2 = 0.89$) and $y = 0.93x + 85$ ($R^2 = 0.86$), respectively, corresponding to the EOIIT. Depending on the individual patient's mean bloodpool intensity value, the EOIIT-value can be determined using the linear correlation, improving the concordance between LGE-extent and LVS-extent (figure 6C&D).

Supplementary material figure S3 demonstrates the distribution extent of LVS and LGE-areas (for the entire LA, anterior and posterior LA) for both the IIR>1.2 and the new EOIIT method for all patients. Analysis of EOIIT-based LGE-extent revealed similarities with LVS-extent (figure 6A and B) with good correlation on the anterior wall (r=0.68, figure 6C). Supplementary material section 2.4 provides more information on the performance of the new EOIIT compared to voltage on the posterior wall, the entire atrium and CV mapping. Detection of LA-LGE-areas

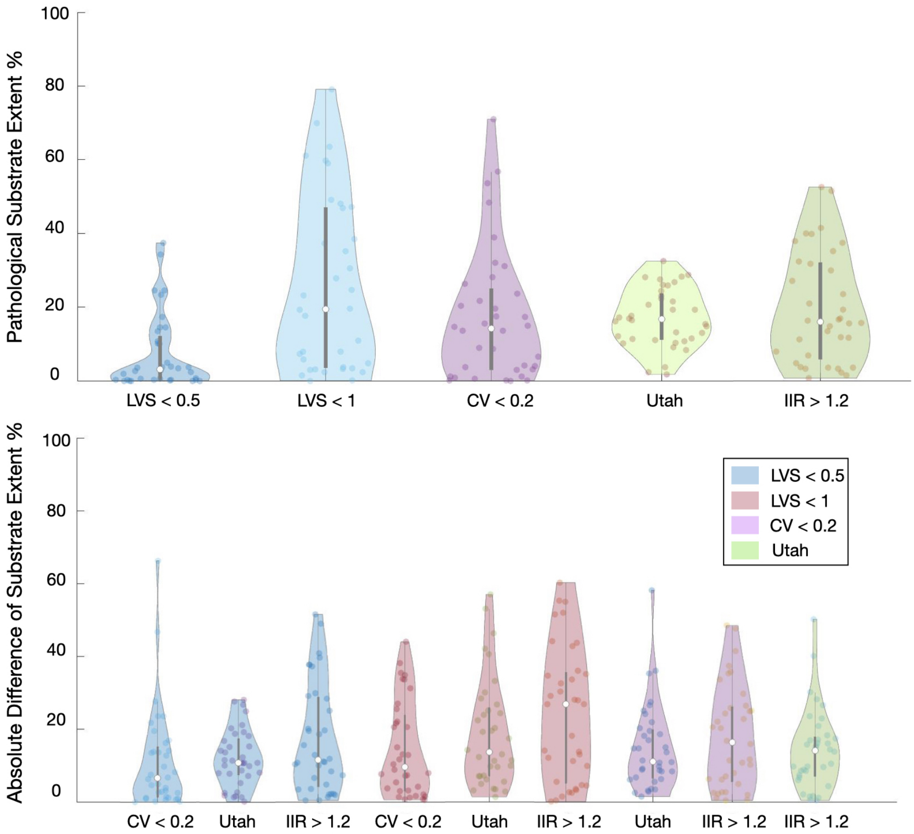

Figure 4: **Violin plot demonstrating the extent of pathological substrate (as percentage of LA surface area) for different mapping modalities and the difference of detected substrate between the methods.** Top row shows the extent for each mapping modality defined on the x-axis. Bottom row shows the difference in extent of detected substrate for the method on the x-axis with the one identified by the colour of the violin plot as reference. Each dot inside a violin plot represents the value for one patient, the white dot represents the median and the bar shows the interquartile range.

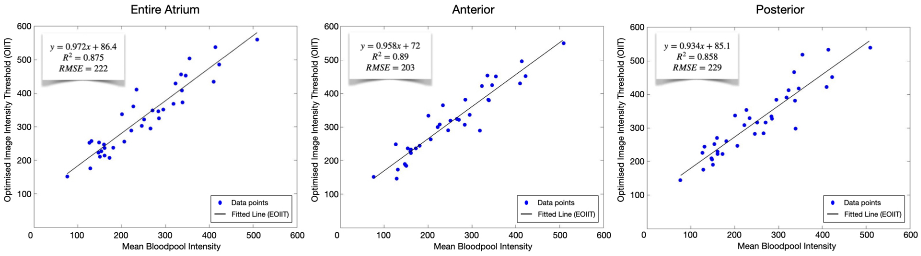

Figure 5: **Identification of the EOIIT using linear correlation between the individual patient's mean bloodpool intensity (x-axis) and optimal image-intensity-threshold (y-axis).** From left to right, the results for the entire left atria, anterior wall and posterior wall are shown. Each blue dot represents one patient and the black line is the best linear fit.

using the new EOIIT-method still did not provide an exact match to LVS-extent in every patient. This is due to the OIIT-value of each patient not lying precisely on the EOIIT-line (figure 5). As seen in figure 6, EOIIT-based LGE-extent (42%) is similar to LVS-extent<0.5 mV (55%) in patient 35. However, the locations of detected substrate remain different between voltage mapping and LGE-MRI.

3.7. Estimated optimised image intensity threshold (EOIIT) enables LGE-MRI-based diagnosis of patients with atrial cardiomyopathy presenting low-voltage substrate

Despite difficulties in exact quantitative match between EOIIT-based LGE-extent and LVS-extent, we hypothesized that the new EOIIT-method could be useful to diagnose patients with significant ACM (defined as LVS <0.5 mV at >5% of LA surface area). ROC-analysis determined the best quantitative LGE-extent for ACM-diagnosis (figure 7). ACM-diagnosis was most accurate when using the EOIIT-based LGE-extent>13% at the anterior LA (sensitivity: 83%, specificity:

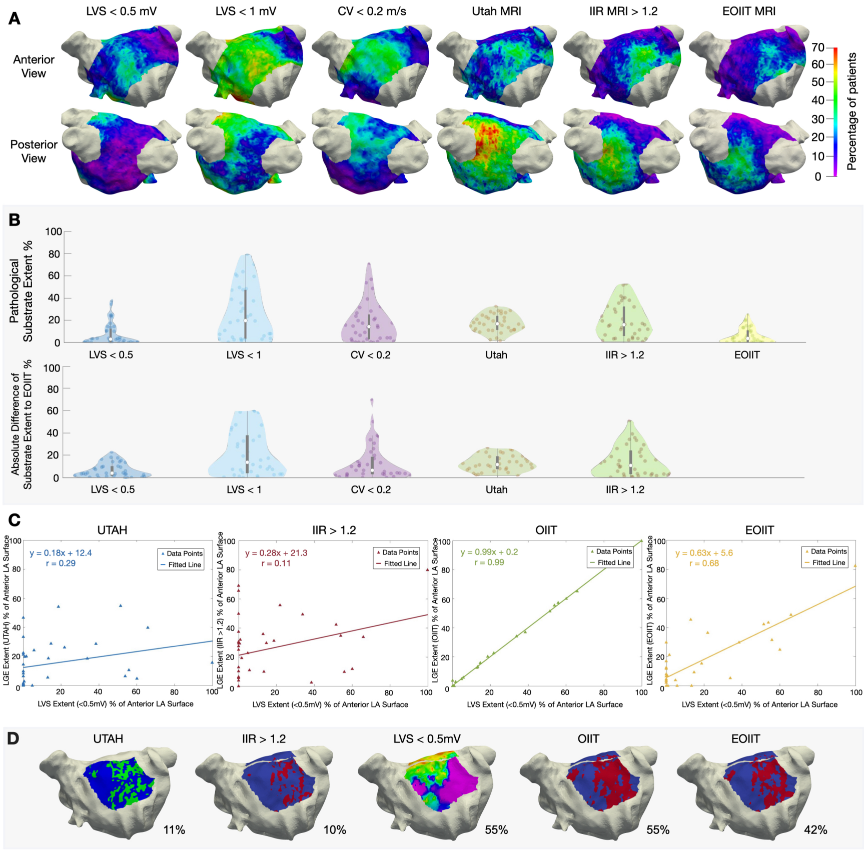

Figure 6: **(A) Spatial histogram of each mapping modality including the new EOIIT method. (B) violin plot showing the pathological substrate extent for different mapping modalities and the difference between them and the new EOIIT method. (C) Percentage of substrate extent of each LGE-MRI method versus LVS-extent for the anterior LA-wall. (D) Distribution extent of LVS and LGE-areas for the anterior LA in patient 35.**

88%, AUC: 0.94), compared to IIR>1.20-based LGE-extent≥31% (sensitivity: 58%, specificity: 75%, AUC: 0.71). Figure 8 additionally illustrates these results, where the mid panel dashed line corresponds to >13% EOIIT-based LGE-extent and >31% IIR>1.20-based LGE-extent at the anterior LA. For the entire LA, the EOIIT-based (>4%) and Utah-based (≥20%) LGE-extent had a sensitivity and specificity of 75% and 67% (AUC: 0.65) and 60% and 75% (AUC: 0.76), respectively.

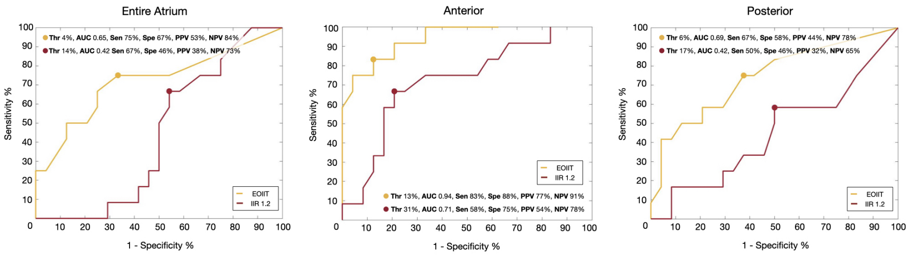

Figure 7: **ROC analysis determines the diagnostic LGE-extent that identifies patients with ACM (defined as LVS <0.5 mV at ≥5% of total LA surface**. From left to right: results for identification of ≥5% LVS-extent on the entire atria when using LGE-extent from the entire LA, anterior and posterior wall. Yellow and red lines show the ROC of the EOIIT-based and IIR >1.2-based methods for LGE-detection, respectively.

4. Discussion

4.1. Main findings

This study investigated the similarity of different mapping modalities in detecting left atrial pathological substrate. Three key findings can be reported:

1. Important discordances exist in the extent and spatial localisation of identified pathological left atrial substrate when comparing electro-anatomical voltage and conduction velocity mapping to LGE-MRI. These discordances

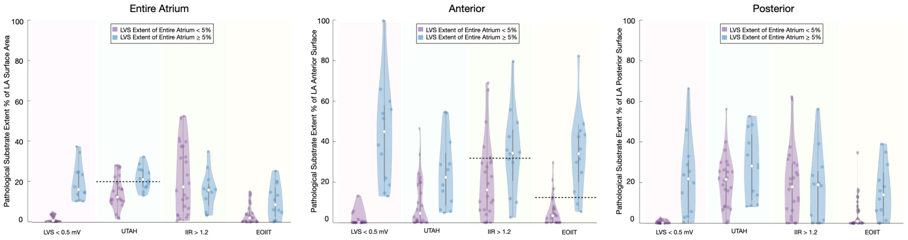

Figure 8: **Violin plots illustrate the extent of detected LA substrate compared to pathological low-voltage substrate<0.5 mV at ≥5% of total LA surface.** The results for the entire LA, anterior wall and posterior wall are shown from the left to right. The blue violins illustrate the extent of pathological substrate in patients who had significant low-voltage extent ≥5%. The purple violins illustrate the extent of pathological substrate in patients who had no significant low-voltage substrate (low-voltage extent <5%).

exist with all LGE-detection protocols and are more pronounced on the posterior LA wall.

2. The extent of left atrial slow-conduction-areas (CV<0.2 m/s) correlated moderately (r = 0.57) well to LVS (LVS<0.5 mV).
3. Applying the new EOIIT-method on the anterior LA-wall enables LGE-MRI-based diagnosis of AF patients with ACM (presenting significant low voltage substrate<0.5 mV at ≥5% LA surface) with a sensitivity of 83% and a specificity of 88%. However, significant differences in localisation of LGE-areas to LVS still remain.

4.2. Clinical significance of left atrial cardiomyopathy in patients with atrial fibrillation

Several studies have demonstrated the relevance of LA-LVS<0.5 mV regarding increased arrhythmia recurrences within 12 months following pulmonary vein isolation (PVI) for AF [14, 20]. Since the correlation of bipolar electrogram voltage with the amount of viable tissue in histology has been shown, this approach was used as a reference [21].

Recently, the predictive value of LVS<0.5 mV at >5% of LA surface was demonstrated concerning arrhythmia recurrence rate following PVI. [18]. Therefore, this LVS-extent was used in the current study. In addition, the presence of ACM, as assessed by LA-LVS is associated with an increased risk for ischemic stroke [22]. Therefore, the most recent European guidelines on the management of patients with AF recommend diagnosis of ACM in order to initiate therapeutic efforts in limiting progression and related complications of ACM [1].

4.3. Regional differences in detected left atrial substrate - comparing EAM to LGE-MRI

Pathological substrate was most consistently (20-40% of patients) found with all modalities (low-voltage, slow conduction and LGE-MRI) at the anterior LA-wall, confirming preferential profibrotic remodeling in this area. Across the whole LA, the CV was 0.48 ± 0.39 m/s, which is comparable to previous findings in AF patients [8, 9]. Our study confirms that low-voltage and slow-conduction areas most frequently develop on the anteroseptal LA-wall and roof [23, 24].

In contrast, both the Utah and IIR>1.20 methods most frequently (56% (Utah-method) and 44% (IIR>1.20-method)) detect LGE at the left posterior LA adjacent to the descending aorta, which is consistent with previous reports [17, 25, 13]. Caixal et al. demonstrated that the spatial proximity of the posterior LA-wall to the descending aorta determines the degree of LGE in this region [25]. Caixal et al. and Spragg et al. reported a reduction of bipolar voltages and agreement between LGE-MRI and low voltage regions at the left posterior LA [26, 27]. However, these were relatively small patient cohorts (16 and 10 patients with only three persistent AF patients in both studies). The current study, which includes 36 persistent AF patients and applies an extended approach to study the spatial extent and distribution between the methods, revealed that CV<0.2 m/s was found in only 28% and LVS<0.5 mV in 8% of patients on the posterior wall. Although voltage reduction can be observed in some patients within this LA area, the electrograms are non-fractionated and display voltages>1.0 mV in >70% of patients. Thus, discrepancies in substrate qualification remain, even when defining LVS as <1.0 mV or <1.5 mV (figure 3).

4.4. Complementarity of mapping systems

Pathological substrate is frequently in opposite locations when comparing electrophysiological substrate to LGE-areas. When considering all patients (supplementary material figures S2-S3), the distribution and location of the pathological substrate is well correlated in some, while they differ in others.

One could hypothesise that the mapping modalities provide complementary information that could be leveraged when determining ablation targets. It has been reported that different fibrotic patterns of various types and densities exist, which could affect the mapping modalities differently [28]. Small patchy fibrotic strands with small contributions to the signal may be compensated by surrounding myocytes and atrial far-fields, causing “undersensing” of fibrotic areas. Additionally, endocardial mapping measurements are dominated by the first 1-2 mm endocardial layer substrate. Fibrosis solely expressed on the epicardial side may be hidden to endocardial catheters. Examining all three methods (CV, LVS and LGE-MRI) may help to comprehensively assess the pathological LA substrate with a more localised analysis than possible with the ECG [29, 30]. However, the fact that ablation of LGE-areas in the DECAAF II study did not improve sinus rhythm maintenance rates, indicates that the detected LGE-areas (using the Utah-method) may not have a major arrhythmogenic role in human AF [19].

4.5. Optimising LGE-MRI thresholds

Identifying the same regions of pathological substrate across all established mapping modalities was not possible with the current techniques. Therefore, we sought to improve LGE-based detection of total LA LVS-extent, thus allowing a more accurate ACM-diagnosis. In this analysis, new LGE-MRI thresholds were identified, which, similarly to the IIR method, can be determined using each patient's mean bloodpool intensity.

Benito et al. studied 30 patients with various stages of AF. They set the threshold to determine pathological substrate at >1.20 [12]. As discussed, determining the exact extent of pathological substrate on the thin posterior wall remains challenging, which may be related to MRI resolution [31]. Since the high-intensity areas were mostly located on the posterior wall across the patient cohort, taking the mean tissue IIR + 2 SD as the threshold in the study by Benito et al. was potentially influenced by these high-intensity areas on the posterior wall. Therefore, their suggested threshold might be too high to identify pathological substrate on the anterior wall.

The new EOIIT-based thresholds presented in this work, however, can provide a better estimate of the LVS-extent located on the anterior LA-wall, thus enabling the diagnosis of ACM in individuals. Previous studies revealed that LVS first develops on the anterior LA, and in later stages involves the posterior LA-wall. [23, 24] Therefore, diagnosis of ACM that is based on analysis of LGE-presence on the anterior LA-wall is both sensitive and specific for ACM-diagnosis, as shown in our study. Accurate diagnosis of ACM provides a deeper insight into whether PVI-only would be sufficient or if additional LA mapping is needed.

5. Limitations

The CV calculation method in the current study did not exclude uncertain LAT values coming from fractionated multicomponent electrograms, potentially limiting the accuracy of CV-maps. LGE-MRI is limited in its spatial resolution (1-2mm) and cardiac and respiratory motions and adjacent enhanced vascular structures (eg aorta) may produce partial volume effect, resulting in “false” LA-LGE-sites and a lack of spatial correlation between LGE-areas and LVS. Additionally, the patient cohort size for this study was relatively small. Thus, overfitting may play a role when computing the linear fit to determine the new LGE-MRI thresholds. To compensate for this effect, leave-one-out-cross validation was used to obtain the best fit. The new EOIIT-LGE-MRI-based ACM-diagnosis needs further validation in larger external cohorts, assessing its predictive value for arrhythmia recurrence following PVI for persistent AF. Furthermore, adaptations for determination of lab-specific EOIIT-curves may be necessary due to the fact that LGE-detection depends on multiple factors (e.g. type, dosage and timing of contrast injection, magnetic field strength, acquisition protocol).

6. Conclusion

Important discordances exist in localisation of detected pathological LA-LVS vs. slow conduction vs. LGE-areas in MRI. Despite a good correlation between the extent of LA-LVS and EOIIT-LGE-areas, the exact locations of identified pathological substrate differ. The new EOIIT-method enables more accurate LGE-MRI-based ACM diagnosis in ablation-naive AF-patients.

Acknowledgements

We gratefully acknowledge financial support by Deutsche Forschungsgemeinschaft (DFG) through DO637/22-3, by the Ministerium für Wissenschaft, Forschung und Kunst Baden-Württemberg through the Research Seed Capital (RiSC) program and by Medtronic.

References

[1] G. Hindricks, T. Potpara, N. Dagres, et al., 2020 ESC guidelines for the diagnosis and management of atrial fibrillation developed in collaboration with the European Association for Cardio-Thoracic Surgery (EACTS), European Heart Journal 42 (5) (2021) 373–498. doi:10.1093/eurheartj/ehaa612.

[2] P. Taghji, M. El Haddad, T. Phlips, et al., Evaluation of a strategy aiming to enclose the pulmonary veins with contiguous and optimized radiofrequency lesions in paroxysmal atrial fibrillation: A pilot study., JACC: Clinical Electrophysiology 4 (1) (2018) 99–108. doi:10.1016/j.jacep.2017.06.023.

[3] A. Verma, C. Jiang, T. R. Betts, et al., Approaches to catheter ablation for persistent atrial fibrillation., The New England Journal of Medicine 372 (19) (2015) 1812–22. doi:10.1056/NEJMoa1408288.

[4] A. Goette, J. M. Kalman, L. Aguinaga, et al., EHRA/HRS/APHRS/SOLAECE expert consensus on atrial cardiomy-

opathies: Definition, characterization, and clinical implication., Heart rhythm 14 (1) (2017) e3–e40. doi:10.1016/j.hrthm.2016.05.028.

[5] A. Jadidi, M. Nothstein, J. Chen, et al., Specific electrogram characteristics identify the extra-pulmonary vein arrhythmogenic sources of persistent atrial fibrillation - characterization of the arrhythmogenic electrogram patterns during atrial fibrillation and sinus rhythm., Scientific Reports 10 (1) (2020) 9147. doi:10.1038/s41598-020-65564-2.

[6] J. Seitz, C. Bars, G. Théodore, et al., AF ablation guided by spatiotemporal electrogram dispersion without pulmonary vein isolation: A wholly patient-tailored approach., Journal of the American College of Cardiology 69 (3) (2017) 303–321. doi:10.1016/j.jacc.2016.10.065.

[7] R. Morgan, M. A. Colman, H. Chubb, et al., Slow conduction in the border zones of patchy fibrosis stabilizes the drivers for atrial fibrillation: Insights from multi-scale human atrial modeling., Frontiers in physiology 7 (2016) 474. doi:10.3389/fphys.2016.00474.

[8] Y. Zheng, Y. Xia, J. Carlson, et al., Atrial average conduction velocity in patients with and without paroxysmal atrial fibrillation, Clinical Physiology and Functional Imagingdoi:10.1111/cpf.12342.

[9] B. Verma, T. Oesterlein, A. Loewe, et al., Regional conduction velocity calculation from clinical multichannel electrograms in human atria, Computers in Biology and Medicine 92 (2018) 188–196. doi:10.1016/j.compbiomed.2017.11.017.

[10] R. S. Oakes, T. J. Badger, E. G. Kholmovski, et al., Detection and quantification of left atrial structural remodeling with delayed-enhancement magnetic resonance imaging in patients with atrial fibrillation, Circulation 119 (13) (2009) 1758–1767. doi:10.1161/CIRCULATIONAHA.108.811877.

[11] N. F. Marrouche, D. Wilber, G. Hindricks, et al., Association of atrial tissue fibrosis identified by delayed enhancement MRI and atrial fibrillation catheter ablation: the DECAAF study, The Journal of the American Medical Association 311 (5) (2014) 498–506. doi:10.1001/jama.2014.3.

[12] E. M. Benito, A. Carlosena-Remirez, E. Guasch, et al., Left atrial fibrosis quantification by late gadolinium-enhanced magnetic resonance: a new method to standardize the thresholds for reproducibility., EP Europace 19 (8) (2017) 1272–1279. doi:10.1093/europace/euw219.

[13] J. Chen, T. Arentz, H. Cochet, et al., Extent and spatial distribution of left atrial arrhythmogenic sites, late gadolinium enhancement at magnetic resonance imaging, and low-voltage areas in patients with persistent atrial fibrillation: comparison of imaging vs. electrical parameters of fibrosis and arrhythmogenesis, EP Europace 21 (10) (2019) 1484–1493. doi:10.1093/europace/euz159.

[14] A. S. Jadidi, H. Lehrmann, C. Keyl, et al., Ablation of persistent atrial fibrillation targeting low-voltage areas with selective activation characteristics, Circulation. Arrhythmia and Electrophysiology 9 (3). doi:10.1161/CIRCEP.115.002962.

[15] D. Nairn, H. Lehrmann, B. Müller-Edenborn, et al., Comparison of unipo-

lar and bipolar voltage mapping for localization of left atrial arrhythmogenic substrate in patients with atrial fibrillation, Frontiers in Physiology 11. doi:10.3389/fphys.2020.575846.

[16] K. P. Anderson, R. Walker, P. Urie, et al., Myocardial electrical propagation in patients with idiopathic dilated cardiomyopathy., Journal of Clinical Investigation 92 (1) (1993) 122–140. doi:10.1172/JCI116540.

[17] K. Higuchi, J. Cates, G. Gardner, et al., The spatial distribution of late gadolinium enhancement of left atrial magnetic resonance imaging in patients with atrial fibrillation, JACC: Clinical Electrophysiology 4 (1) (2018) 49–58. doi:10.1016/j.jacep.2017.07.016.

[18] B. Müller-Edenborn, Z. Moreno-Weidmann, S. Venier, et al., Determinants of fibrotic atrial cardiomyopathy in atrial fibrillation. a multicenter observational study of the RETAC (reseau européen de traîtement d'arrhythmies cardiaques)-group, Clinical Research in Cardiologydoi:10.1007/s00392-021-01973-1.

[19] N. F. Marrouche, T. Greene, J. M. Dean, et al., Efficacy of LGE-MRI-guided fibrosis ablation versus conventional catheter ablation of atrial fibrillation: The DECAAF II trial: Study design, Journal of Cardiovascular Electrophysiology 32 (4) (2021) 916–924. doi:10.1111/jce.14957.

[20] S. Rolf, S. Kircher, A. Arya, et al., Tailored atrial substrate modification based on low-voltage areas in catheter ablation of atrial fibrillation., Circulation. Arrhythmia and electrophysiology 7 (5) (2014) 825–33. doi:10.1161/CIRCEP.113.001251.

[21] C. A. Glashan, B. J. Tofig, H. Beukers, et al., Multielectrode unipolar voltage mapping and electrogram morphology to identify post-infarct scar geometry: Validation by histology, JACC: Clinical Electrophysiology-doi:10.1016/j.jacep.2021.11.012.

[22] P. Müller, H. Makimoto, J. W. Dietrich, Others, Association of left atrial low-voltage area and thromboembolic risk in patients with atrial fibrillation, EP Europace 20 (2018) 359–365. doi:10.1093/europace/eux172.

[23] Y. Huo, T. Gaspar, M. Pohl, et al., Prevalence and predictors of low voltage zones in the left atrium in patients with atrial fibrillation, EP Europace 20 (6) (2018) 956–962. doi:10.1093/europace/eux082.

[24] B. Müller-Edenborn, J. Chen, J. Allgeier, et al., Amplified sinus-p-wave reveals localization and extent of left atrial low-voltage substrate: implications for arrhythmia freedom following pulmonary vein isolation., EP Europace-doi:10.1093/europace/euz297.

[25] G. Caixal, T. Althoff, P. Garre, et al., Proximity to the descending aorta predicts regional fibrosis in the adjacent left atrial wall: aetiopathogenic and prognostic implications, EP Europace 23 (10) (2021) 1559–1567. doi:10.1093/europace/euab107.

[26] D. D. Spragg, I. Khurram, S. L. Zimmerman, et al., Initial experience with magnetic resonance imaging of atrial scar and co-registration with electroanatomic voltage mapping during atrial fibrillation: Success and limitations, Heart Rhythm 9 (12) (2012) 2003–2009. doi:10.1016/j.hrthm.2012.08.039.

[27] G. Caixal, F. Alarcón, T. F. Althoff, et al., Accuracy of left atrial fibrosis detection with cardiac magnetic resonance: correlation of late gadolinium enhancement with endocardial voltage and conduction velocity., EP Europacedoi:10.1093/europace/euaa313.

[28] B. J. Hansen, J. Zhao, V. V. Fedorov, Fibrosis and atrial fibrillation: Computerized and optical mapping, JACC: Clinical Electrophysiology 3 (6) (2017) 531–546. doi:10.1016/j.jacep.2017.05.002.

[29] C. Nagel, G. Luongo, L. Azzolin, et al., Non-invasive and quantitative estimation of left atrial fibrosis based on p waves of the 12-lead ECG-a large-scale computational study covering anatomical variability., Journal of Clinical Medicine 10 (8). doi:10.3390/jcm10081797.

[30] G. Luongo, L. Azzolin, S. Schuler, et al., Machine learning enables noninvasive prediction of atrial fibrillation driver location and acute pulmonary vein ablation success using the 12-lead ECG, Cardiovascular Digital Health Journal 2 (2) (2021) 126–136. doi:10.1016/j.cvdhj.2021.03.002.

[31] S. Y. Ho, J. A. Cabrera, D. Sanchez-Quintana, Left atrial anatomy revisited, Circulation: Arrhythmia and Electrophysiology 5 (1) (2012) 220–228. doi:10.1161/CIRCEP.111.962720.

Chapter 7

Summary and Conclusion

In persistent AF patients, it has been identified that extra-PV pathological substrate located in the body of the atria may be maintaining the arrhythmia [12–15]. Additionally, targeting these areas can improve the success rate of the ablation procedure. However, about 30-50% of patients have AF recurrence after the procedure [11, 12]. The lack of consensus regarding a precise, unambiguous method to locate the ablation targets may cause these high recurrence rates. Therefore, this thesis, comprised of three parts, used simulated and clinical data to compare, understand and improve techniques to accurately and robustly identify pathological substrate areas. Furthermore, allowing comparability between studies and centres and contributing to leveraging techniques' full potential to guide catheter ablation in persistent AF patients.

Chapter 4 investigated if bipolar voltage mapping to identify pathological substrate is affected by the characteristics of the catheter used. This investigation suggests that while the catheter angle to the wavefront and the inter-electrode distance do play a role in altering the bipolar voltages, the changes are not significant to discredit the approach for identifying pathological substrate. Using the unipolar thresholds identified in this work could allow clinicians to better estimate the size of the pathological substrate areas. Aside from the challenges which affect the bipolar voltage mapping, factors such as the electrode size can impact both the bipolar and unipolar voltage. This work identified that the electrode size could substantially impact the voltage in both healthy and diseased tissue. However, the impact is less pronounced in diseased tissue. It is advised to take caution when applying results across centres. All centres using the same size and configuration of electrodes would be optimal. Nevertheless, while this is not the case, using the relationship identified in this work between different electrode sizes can help to improve multi-centre comparability, for example, understanding why a study may suggest higher voltage thresholds to identify the same extent of LVS in a patient.

Chapter 5 explored the relationship between performing voltage mapping during two rhythms (SR and AF). It was identified that areas of LVS as located during SR could be found using the proposed AF thresholds. However, discordances remain between mapping in the different rhythms. By investigating further, it was identified that the difference in voltage between the two maps was not consistent across the atrium. By applying different voltage thresholds to anatomical regions, the area and extent of LVS could be better approximated. Moreover, this work identified that calculating the voltage based on the maximum peak-to-peak amplitude in the signal provides the greatest correspondence between methods. Finally, these studies identified that more complex propagation patterns in AF might cause the discrepancies found when compared to SR. This was marginally verified by the lower correlation between the SR and AF voltage map in patients mapped in native AF rather than induced AF, since it is likely that these patients may have a more advanced form of remodelling and, thus, more complex propagation patterns. The variability measure (sample entropy) studied in this thesis may help identify the regions where more complex propagation patterns affect the catheter's signals and distinguish different types of fibrosis.

Chapter 6 extends the identification of pathological substrate to the LGE-MRI and electro-anatomical voltage and conduction velocity mapping. Important discrepancies between each mapping modality were identified, specifically on the posterior region of the LA, indicating a key area that needs further investigation. Spatial histograms showing low voltage and slow conduction areas were created, providing the opportunity to identify where regions to target for ablation are typically located. Specifically, all modalities indicated that pathological substrate was often located on the anterior wall, indicating the importance of mapping this region. Thus this work supplies a guide to the clinicians of essential areas to map during the procedure and perhaps take extra time collecting information to better estimate the extent of pathological substrate needed to be targeted during the ablation procedure. Alternatively, since in other regions of the atrium each of these modalities differed, it could indicate that each holds complementary information, which could be beneficial to further understand and identify the pathological substrate. Finally, the new LGE-MRI thresholding method developed in this work could allow a less invasive way to identify patients with atrial cardiomyopathy. This could provide insight into whether PVI would be sufficient or if the atrium needs to be mapped to locate extra-PV sources driving the arrhythmia.

In conclusion, this work has provided the community with a deeper understanding of the different mapping modalities used to identify pathological substrate. With the addition of in silico experiments, open questions that could not be answered by clinical data alone, where the ground truth is unknown, could be assessed. Additionally, clear, comparable methods and cut-off values were proposed, which can help to identify low voltage areas and guide persistent AF ablation therapy.

Chapter 8

Outlook

While the projects presented in this thesis have helped to answer open questions in the field, the projects have also led to more questions and identified areas where more investigation needs to be applied.

Computational modeling allowed to further understand the mechanisms driving AF while knowing the ground truth. In this work, a simulation setup was built by deforming a replica of a clinical catheter on the wall of a 3D left atrial geometry. This tool provides endless opportunities to understand AF within a controlled environment while providing more realistic signals and phenomena than a simple 2D patch simulation. One possibility for further study is to include areas of pathological substrate into the tissue and observe how the voltage values change and if the same region of LVS can be identified by applying a cut-off value. Multiple wavefronts can then be introduced into the model, allowing the possibility to observe how complex propagation patterns may alter the detection of these substrate areas. This would also help answer whether this could cause the discrepancies between SR and native AF voltage mapping. Additionally, it could help to better understand mapping during AF and its applicability and benefit to the clinical practice.

Additionally, these 3D geometry simulations can be extended to other catheter geometries, such as the Orion, where the electrode size is small. Therefore, while multiple systems are being used across centres, this approach could help identify the exact translation factor needed to determine the same region of pathological substrate in a patient regardless of the system used to perform the procedure.

One part of this work investigated how calculating the voltage during AF in different ways would compare to mapping during SR. While it was found that using the maximum peak-to-peak amplitude in the signal was optimal, it was also identified that the catheter may have unintentionally moved while collecting some of the signals. Additionally, the signals are only 2.5 s, which means that there are few peaks to determine the median, mean, and percentiles. The CARTO-3 system has recently been upgraded to record and export signals of up to 30 s. Therefore, it would be beneficial to reanalyse the results using different calculation methods in AF when longer signals are acquired and where the catheter was held at one position for longer. The disadvantage of this approach is that it increases the time of the procedure, adding potential additional risks to the patient. Therefore, it may be challenging to obtain such long signals. However, even investigating 10 s signal could already be beneficial to perform the analysis.

While investigating the relationship between SR and AF voltage mapping, it was identified that there is a difference if the AF was induced. Some speculation was given into why this may be the case. Using simulations as mentioned above may help to verify this. However, it would be very interesting to obtain clinical data from patients where all three maps were obtained: SR, native AF, and induced AF. Therefore, one could directly observe any differences between mapping during induced and native AF.

Additionally, discrepancies were still found between mapping in SR and AF. It was identified that while there was a reasonable agreement for the majority of the patients, this was not the case for all. In fact, across most studies, agreement between mapping modalities would vary from patient to patient. Implementing a more personalised ablation approach may help overcome the remaining dissimilarities.

Finally, a new LGE-MRI analysis method was proposed for the diagnosis of ACM. By examining follow-up data and identify cases of arrhythmia recurrence, it could be determined if this method is predictive for the outcome of PVI after 12 months.

Appendix A

Supplementary Materials

A.1 Determinants of Bipolar Voltage Mapping

---

1 SUPPLEMENTARY TABLES AND FIGURES

1.1 Figures

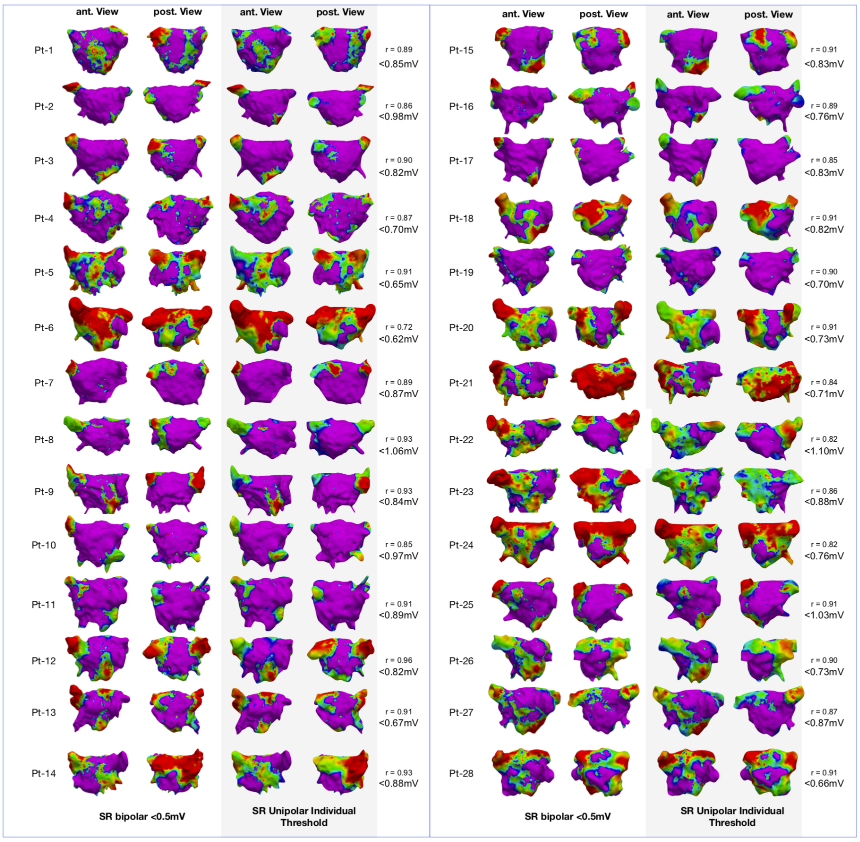

Figure S1. Three-dimensional distribution patterns of low voltage substrate in bipolar vs. unipolar voltage mapping mode for each one the 28 patients in SR with a bipolar threshold $<$0.5 mV. On the left side, patients 1-14 are shown, where the columns from left to right indicates: (1) the bipolar map (anterior view), (2) the unipolar map (anterior view), (3) the bipolar map (posterior view) and (4) the unipolar map (posterior view). On the right side the same is shown for patients 15-28. The voltage threshold of the unipolar maps were optimized for each patient to find the highest spatial overlap between LVS in bipolar vs unipolar maps. This optimal patient-specific unipolar threshold and the Pearson correlation coefficient is annotated at the right side of each row.

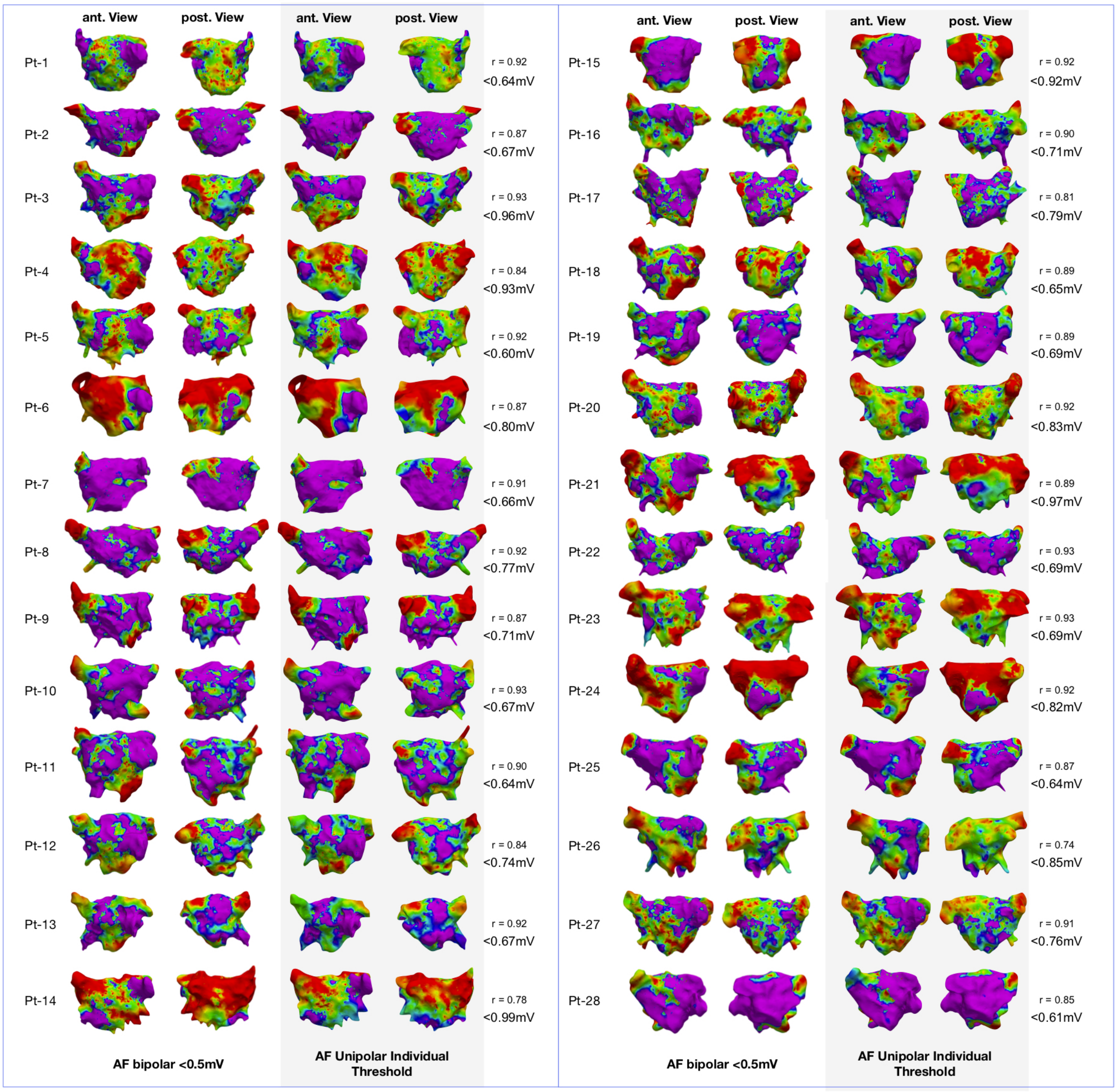

Figure S2. Three-dimensional distribution patterns of low voltage substrate in bipolar vs. unipolar voltage mapping mode for each one the 28 patients in AF with a bipolar threshold <0.5 mV. On the left side, patients 1-14 are shown, where the columns from left to right indicates: (1) the bipolar map (anterior view), (2) the unipolar map (anterior view), (3) the bipolar map (posterior view) and (4) the unipolar map (posterior view). On the right side the same is shown for patients 15-28. The voltage threshold of the unipolar maps were optimized for each patient to find the highest spatial overlap between LVS in bipolar vs unipolar maps. This optimal patient-specific unipolar threshold and the Pearson correlation coefficient is annotated at the right side of each row.

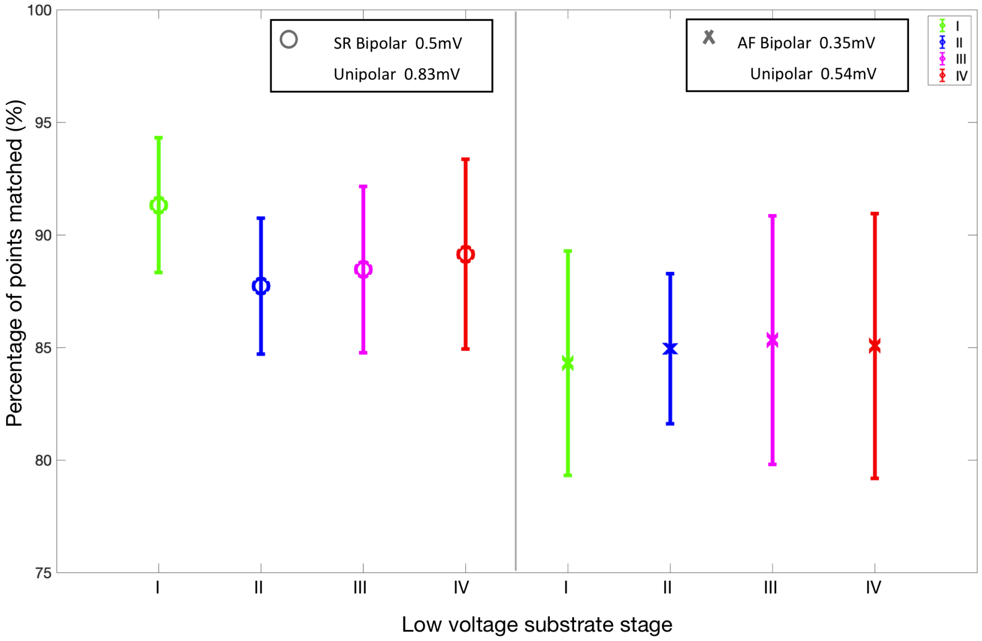

Figure S3. Mean and standard deviation of the percentage of points which match for the 4 different patient subgroups defined by the extent of low voltage substrate. Each color represents a subgroup (I-IV) in SR and AF for the given bipolar and unipolar thresholds as found in figure 4 of the main article.

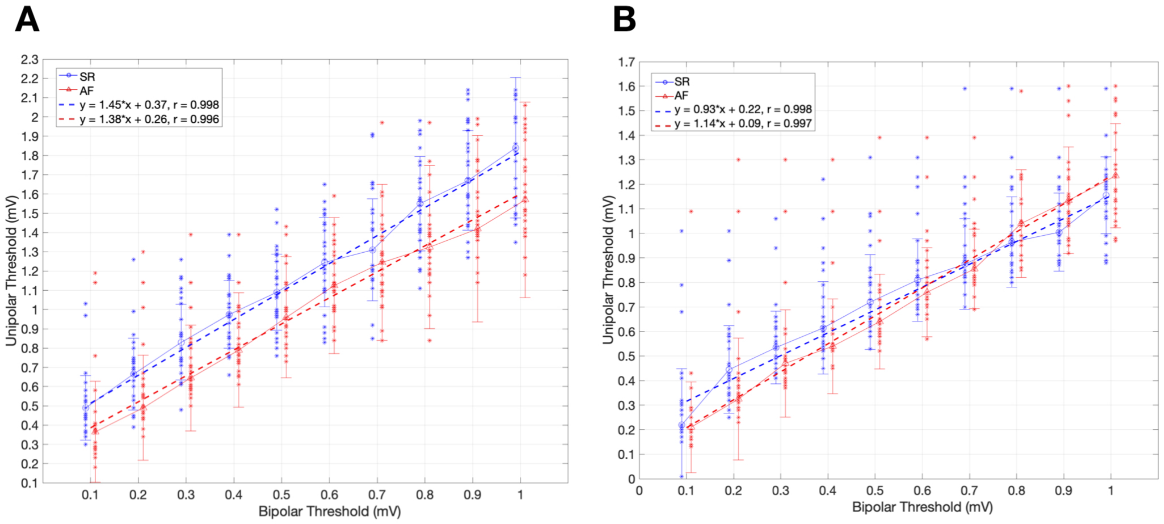

Figure S4. Relationship between the bipolar and unipolar threshold in SR (blue) and AF (red) using only 2mm bipoles (A) and 6mm (B). The unipolar threshold with highest concordance to the bipolar map is shown for different bipolar thresholds and each individual patient (blue and red dots for SR and AF, respectively). Standard deviation is represented by bars. The optimal unipolar threshold is identified as the optimal point on the ROC curve of each bipolar threshold using all patients. Linear regression shown as dotted lines, depending on the rhythm (SR blue, AF red). Pearson correlation coefficient (r) is provided.

A.2 Electro-anatomical Mapping during Atrial Fibrillation

Supplementary Material for “Spatial Correlation of Left Atrial Low Voltage Substrate in Sinus Rhythm versus Atrial Fibrillation: Identifying the Pathological Substrate Irrespective of the Rhythm”

Deborah Nairn[1]*[#], Martin Eichenlaub[2#], Heiko Lehrmann[2], Björn Müller-Edenborn[2], Juan Chen[2], Taiyuan Huang[2], Claudia Nagel[1], Jorge Sánchez[1], Giorgio Luongo[1], Thomas Arentz[2], Olaf Dössel[1], Amir Jadidi[2§] and Axel Loewe[1§]

[1]*Institute of Biomedical Engineering, Karlsruhe Institute of Technology, Karlsruhe, Germany*
[2]*Department of Electrophysiology, University-Heart-Center Freiburg-Bad Krozingen, Bad Krozingen, Germany*

[#],[§] *These authors contributed equally.*

1. Supplementary Figures

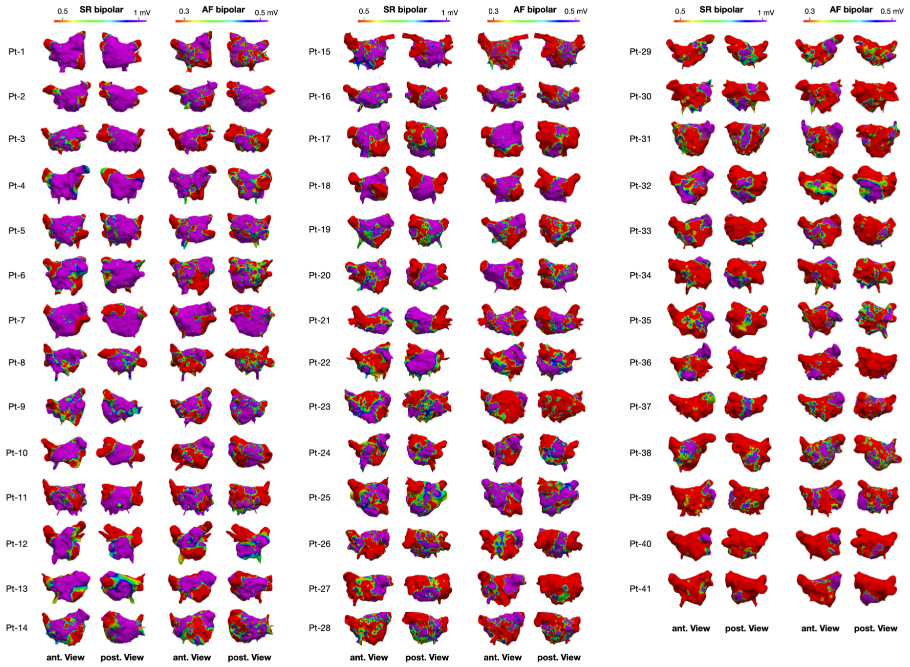

Figure 1: **Voltage maps acquired during SR and AF for all 41 patients.** For each patient the anterior (left) and posterior (right) view of the voltage map is shown. Cutoff values of 0.5-1 mV were set for the SR map and 0.3-0.5 mV for AF.

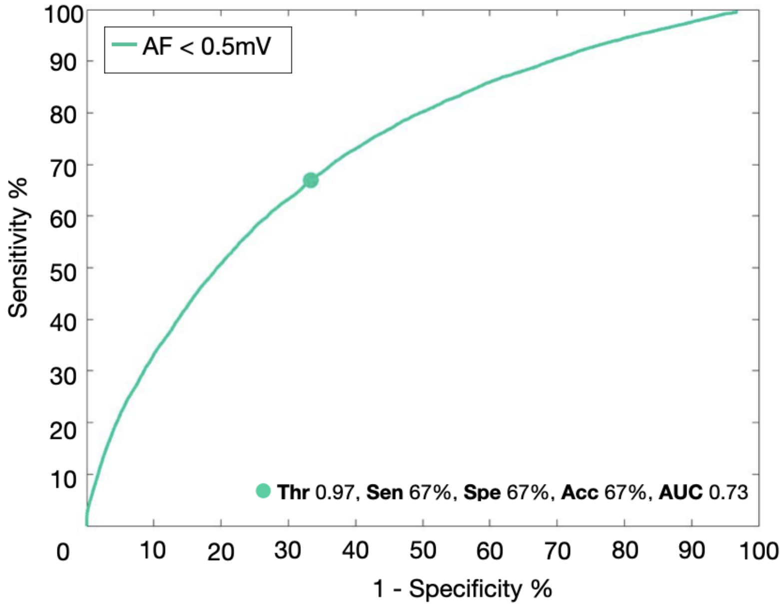

Figure 2: **ROC curve comparing LVS as identified during AF (<0.5 mV) and during SR .** The optimal SR threshold across all patients and corresponding performance metrics are given in the legend.

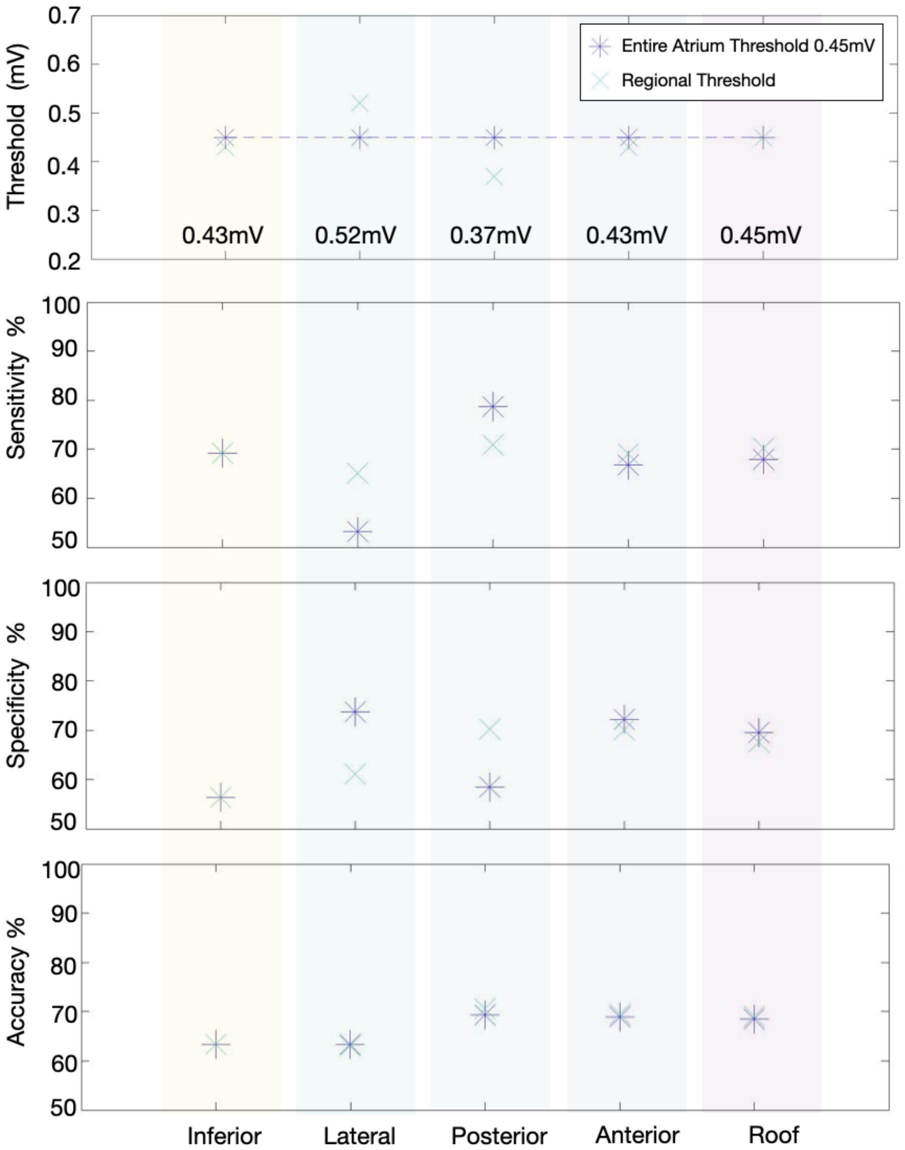

Figure 3: **Optimal AF threshold and the corresponding sensitivity, specificity and accuracy for each anatomical region of the LA comparing to SR-LVS <1 mV.** The previously defined global threshold for the entire atria is shown by the purple asterisk and the green cross presents the regional thresholds.

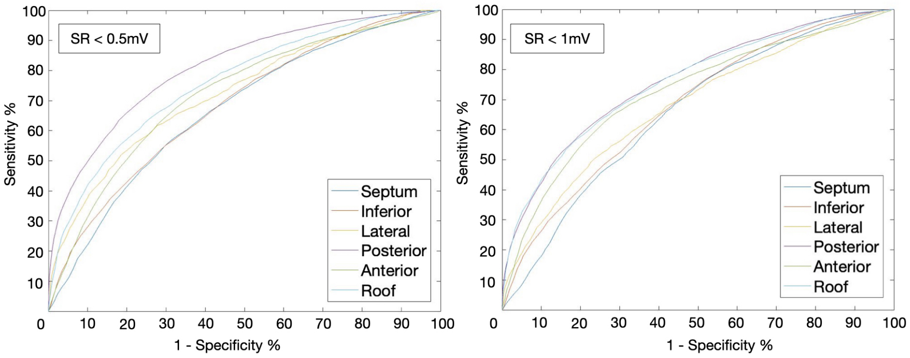

Figure 4: **ROC curves comparing the AF maps to the SR maps (<0.5 and <1 mV) for different anatomical regions of the left atria.**

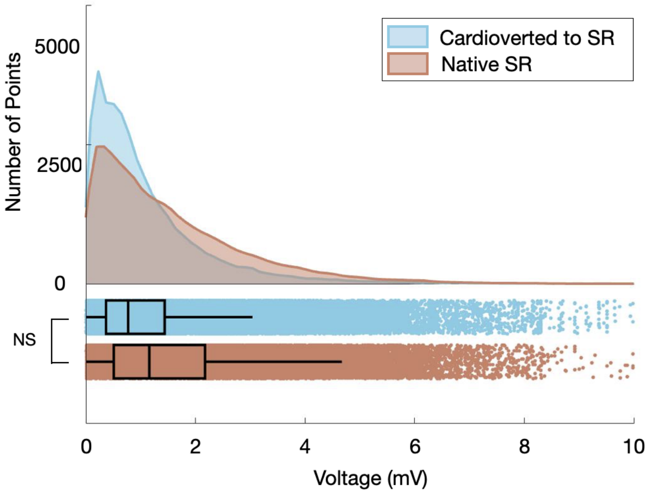

Figure 5: **Histogram and boxplot of the voltage distribution in patients in whom were cardioverted to SR (after mapping native AF) versus native SR.** Blue: patients whom were cardioverted to SR, red: patients presenting with native SR.

A.3 Multi-Modality Identification of Atrial Cardiomyopathy

Supplementary Material for “Discrepancy Between LGE-MRI, Electrogram Voltage and Conduction Velocity for Detecting Left Atrial Fibrotic Substrate”

Deborah Nairn, MSc[1]*[#], Martin Eichenlaub, MD[2#], Björn Müller-Edenborn, MD[2], Heiko Lehrmann, MD[2], Claudia Nagel, MSc[1], Luca Azzolin, PhD[1], Giorgio Luongo, PhD[1], Rosa M. Figueras Ventura, PhD[3], Barbara Rubio Forcada, MSc[3], Anna Vallès Colomer, MSc[3], Thomas Arentz, MD[2], Olaf Dössel, PhD[1], Axel Loewe, PhD[1§] and Amir Jadidi, MD[2§]

[1] *Institute of Biomedical Engineering, Karlsruhe Institute of Technology, Karlsruhe, Germany*

[2] *Department of Electrophysiology, University-Heart-Center Freiburg-Bad Krozingen, Bad Krozingen, Germany*

[3] *Adas 3D Medical SL, Carrer Paris 179, Barcelona, Spain*

[#],[§] *These authors contributed equally.*

1. Supplementary Methods

1.1. Electro-anatomical mapping

Bandpass filtering at 16-500 Hz was applied to all bipolar electrograms using the CARTO-3 system. Any electrograms obtained when the electrodes were >7 mm from the atrial surface were removed from the analysis. Manual quality assessment was conducted to discard electrograms containing only noise or major artefacts. The system calculated the bipolar voltage values as the peak-to-peak amplitude of a single atrial beat in SR (the window of interest was restricted to the PR-interval with exclusion of the QRS complex). In this window, the local activation times (LAT) were also determined automatically by locating the maximum amplitude of the bipolar signal. The LAT was adjusted manually if it was incorrectly detected. All areas demonstrating LVS as displayed by the multi-electrode mapping catheters were confirmed using a separate contact force-sensing mapping catheter with a contact threshold of >5 g.

The CV was calculated from the LAT maps using the algorithms based on the polynomial fit technique described by Nagel et al. [1]. A feature to detect areas of potential wavefront collisions was additionally used. In these areas, the CV was recalculated in a second iteration in regions where only homogeneous excitation propagation occurred. The range of CV values can vary depending on the density of the fibrosis, which is unknown in this study [2].

1.2. Late gadolinium enhancement magnetic resonance imaging (LGE-MRI)

1.2.1. Image intensity ratio method

For the IIR method, a mid-myocardial layer was defined to create a shell in 3-dimensional space [3]. Left atrial mean blood pool intensity was automatically identified and IIR was calculated as the ratio between signal intensity of each voxel of the mid-myocardial LA layer normalized by the mean blood pool intensity. As described by Benito et al., voxels with an IIR of >1.20 were considered as pathological substrate and an IIR of >1.32 as dense scar [3].

1.2.2. Utah method

For the Utah LGE segmentation method, endocardial and epicardial borders of the LA were manually traced. Subsequently, the threshold was calculated as 2 to 4 standard deviations above the mean of the “normal tissue” on a slice-by-slice basis based on the operator’s opinion [4, 5].

1.3. LA mean geometry

A mean LA geometry built for a previous study was used [6]. The geometries obtained from each modality for all 36 patients were then aligned to the mean LA shape automatically using the iterative closest point algorithm with Scalismo, a statistical shape modelling software [7, 8]. After, Gaussian process morphable models were used to obtain a dense correspondence between each geometry and the mean LA. This is the same approach as used for building statistical shape models [9]. This approach yields the same number of surface points representing the same anatomical landmarks for each geometry. In this way, the patient's voltage, CV, LGE-MRI intensity values and Utah classification could be obtained for every point of the mean geometry.

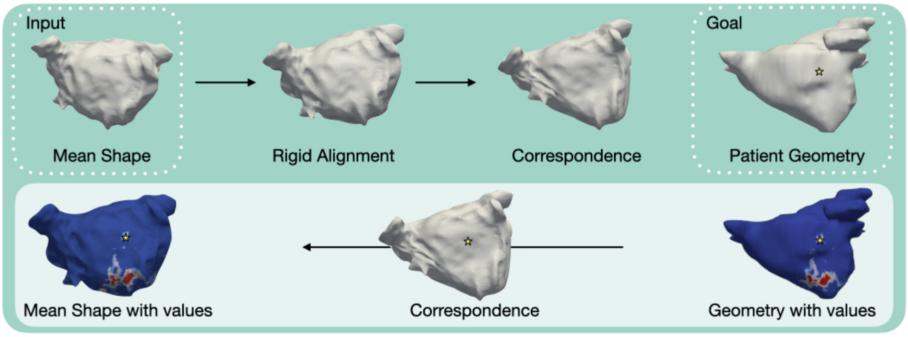

Figure 1: **Schematic diagram of the patient's information being projected onto the mean shape for an example patient.** On the top row, the steps applied to the mean shape to find correspondence with the patient-specific geometry are shown. The bottom row illustrates that a point is chosen (the star) and identified on the correspondence map, which has the same point ID's as the mean shape so that the information can be transferred back.

1.4. Region-specific analysis

The regions were obtained semi-automatically: first, rings around the PVs, MV and the left atrial appendage (LAA) were drawn using Blender, a 3D computer graphics software [10]. Following, the Eikonal equation was solved to obtain the shortest path between all rings. Paths were then chosen, which split the atria into the aforementioned regions.

2. Supplementary Results

2.1. Patient characteristics

Patient Characteristics	**Total = 36**
Age (years)	66 ± 9
Male (%)	31 (84)
BMI (kg/m^2)	27.4 ± 3.5
LVEF (%)	57 ± 8
LA diameter (AP, mm)	47 ± 6
CHA$_2$DS$_2$-VASc score	2 (1-3)
Hypertension (%)	27 (73)
Diabetes mellitus (%)	3 (8)
Prior stroke or TIA (%)	1 (3)
Coronary artery disease (%)	5 (14)
Procedure duration (min)	146 ± 19
Successful circumferential PVI (%)	36 (100)
CTI ablations (%)	8 (22)
Prior antiarrhythmic therapy (%)	29 (78)

Table 1: **Patient clinical demographics.** Abbreviations: BMI = body mass index, LVEF = left ventricular ejection fraction, LA = left atrial, AP = anterior-posterior, TIA = transient ischemic attack, PVI = pulmonary vein isolation, CTI = cavotricuspid isthmus .

Electro-anatomical Mapping	**SR**
Map points (pts)	2098 ± 515
Bipolar voltage (mV)	1.84 ± 1.59
CV (m/s)	0.48 ± 0.49
LVS surface area, SR < 0.5 mV (cm^2(%))	14 ± 19 (7 ± 10)
Slow CV surface area, CV < 0.5 mV (cm^2(%))	22 ± 24 (12 ± 13)

LGE-MRI	
IIR Intensity values	1.01 ± 0.23
High intensity surface area, IIR > 1.2 (cm2 (%))	37 ± 27 (20 ± 15)
UTAH fibrotic surface area (cm^2(%))	22 ± 10 (12 ± 5)

Table 2: **Mapping information of patients included in the study.**

2.2. Spatial distribution of electro-anatomical and LGE-MRI maps

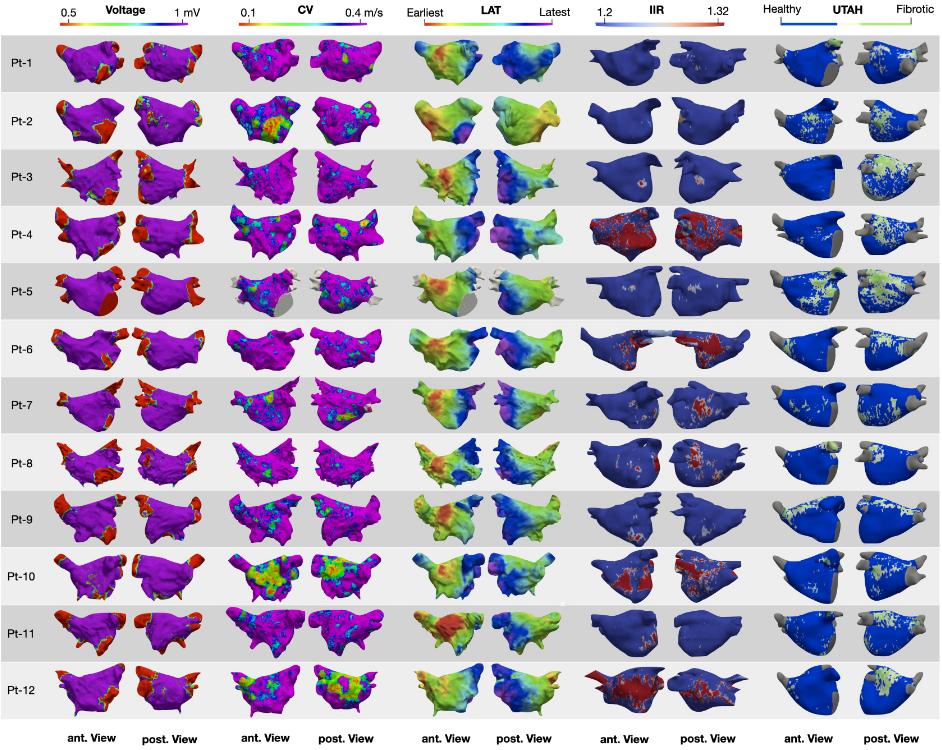

(a) Patient 1-12

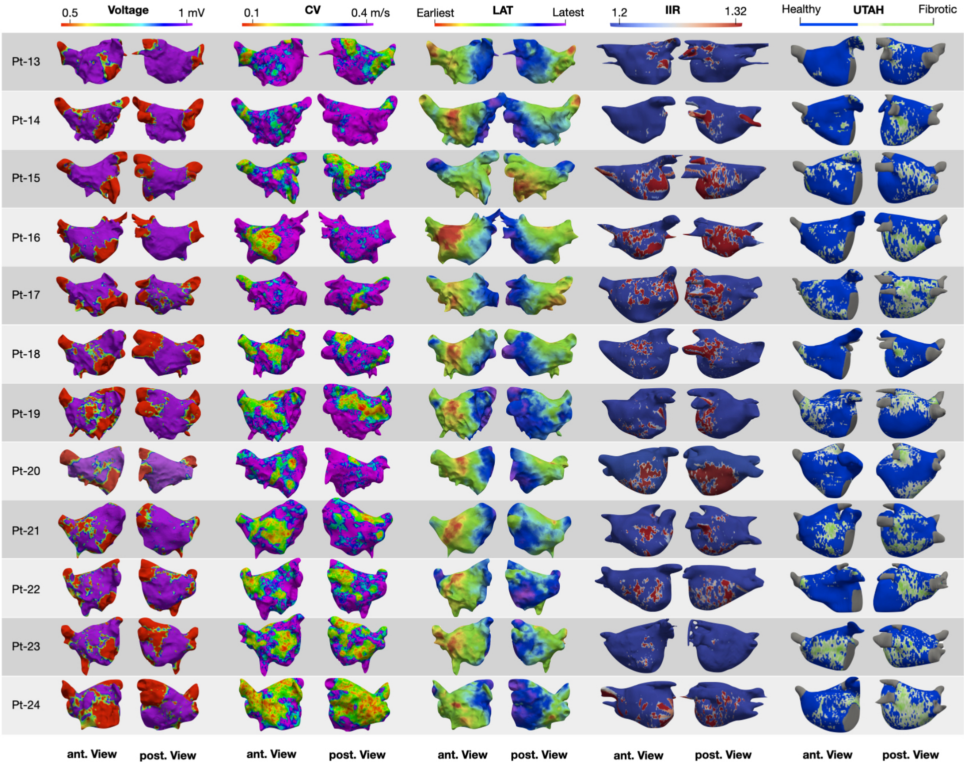

(b) Patient 13-24

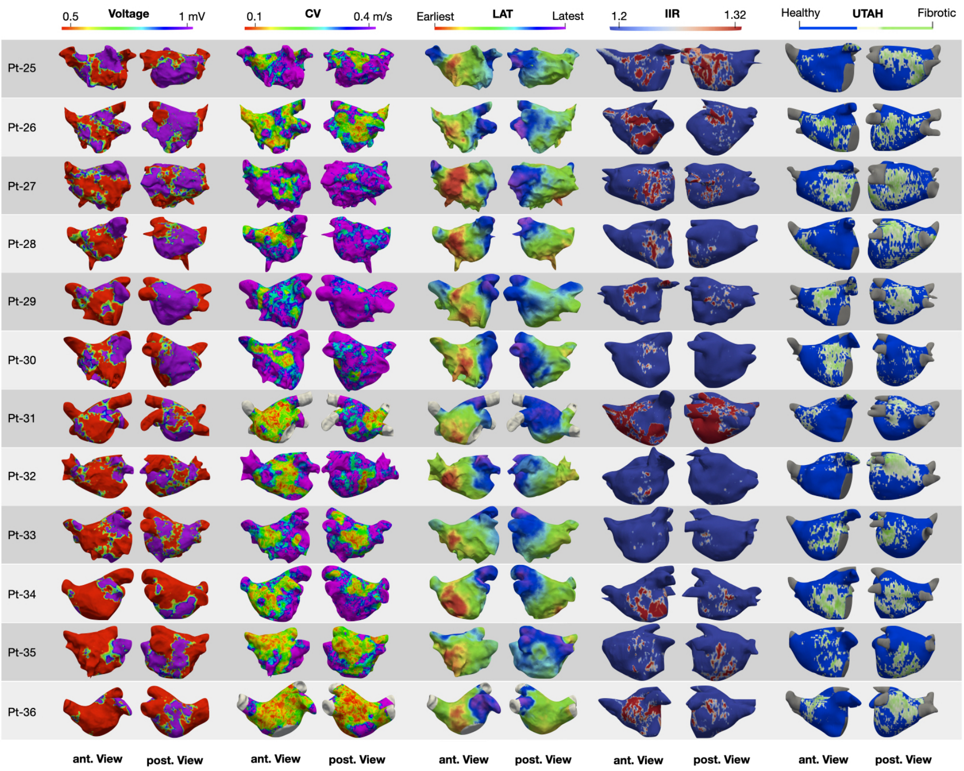

(c) Patient 25-36

Figure 2: **Three-dimensional distribution patterns of the pathological substrate in different mapping modalities for all patients.** Each row shows one patient and each column pair shows the anterior and posterior view for that patient. On the left the voltage map can be seen, with voltages below 0.5 mV in red and above 1 mV in purple. Next the conduction velocity between 0.2 and 0.4 m/s. The LAT map is then shown from earliest to latest activation for each patient. Following is the LGE-MRI using the IIR method shown with cut off values between 1.2 and 1.32. Finally, the LGE-MRI using the Utah method is shown, with fibrotic areas in green and healthy areas in blue.LVS and slow CV was found to extensively cover the anteroseptal wall in all patients presenting LVS ≥5% of total LA at <0.5 mV.

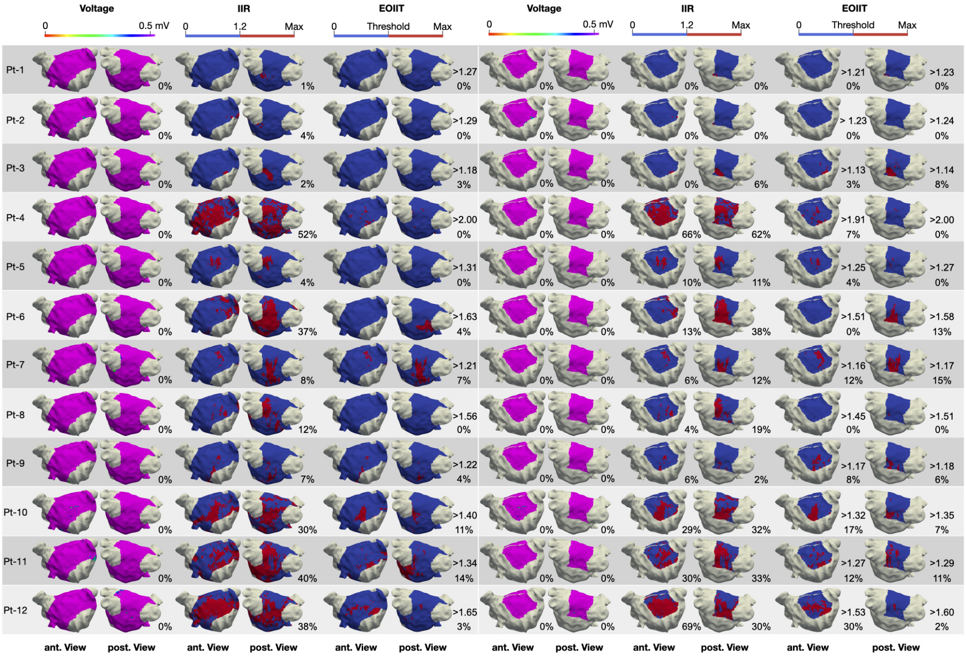

(a) Patient 1-12

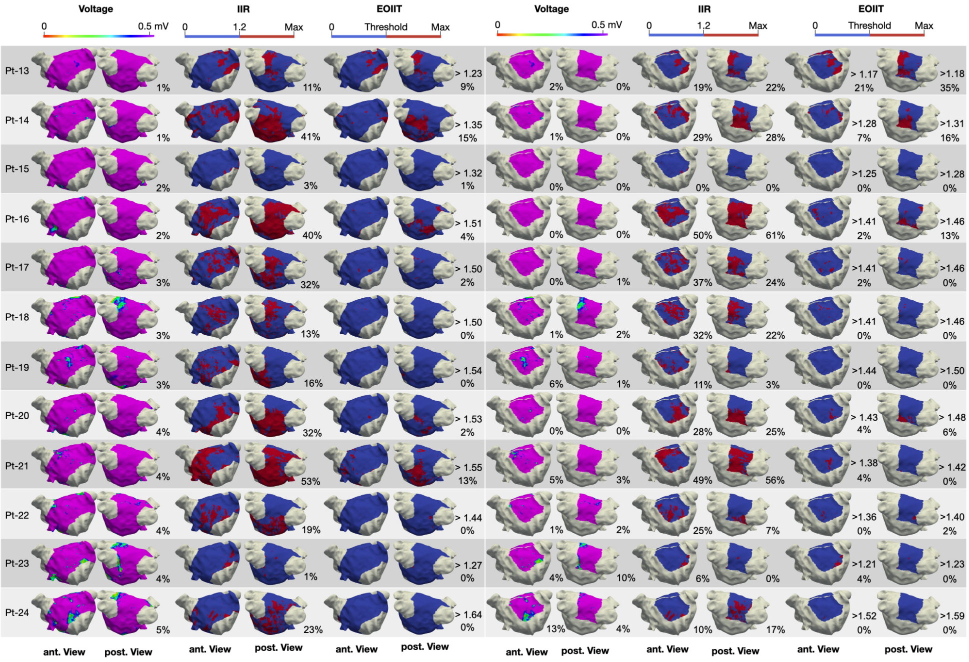

(b) Patient 13-24

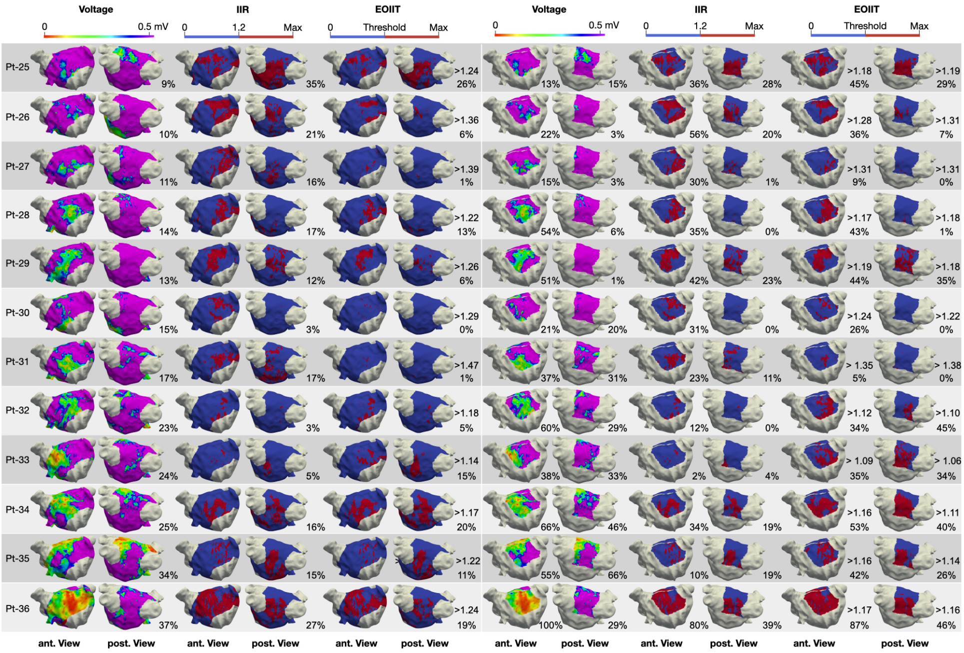

(c) Patient 25-36

Figure 3: **Three-dimensional voltage and LGE-MRI maps showing the high intensity areas defined by the IIR > 1.2 threshold and using the new EOIIT thresholds.** Each row shows one patient and each column pair shows the anterior and posterior view for that patient. On the left hand side the percentage of low voltage and high intensity can be seen for the entire atria excluding the PV's and MV. On the right, the percentage can be seen for the the anterior and posterior wall seperately. The new EOIIT threshold for each patient is given divided by that patients mean bloodpool value to allow for quick comparability to the IIR method.

2.4. Optimising the LGE-MRI threshold to identify low-voltage substrate

To quantify the performance of the new EOIIT, the percentage of LGE-MRI extent defined by the new thresholds was plotted against the percentage of LVS extent (<0.5 mV) as shown in figure 4. Figure 4 shows for the anterior wall, a substantial improvement (y = 0.63x + 5.6, R^2 = 0.68, p <0.001) occurred when using the new EOIIT compared to the IIR >1.2 threshold (y = 0.28x + 21.3, R^2 = 0.11) with the optimal relationship being a diagonal line. From figure 4 the Bland-Altman plot shows that previously the LGE-MRI was measuring on average 10% more pathological substrate than the voltage map. Using the new thresholds, this value is reduced to 0%. Figure 5 shows the plots for the entire atrium and the posterior wall. Only a slight improvement was seen in estimating the percentage of LV extent from the MRI compared to using the IIR >1.2 threshold. Additionally, the new EOIIT thresholds show an improvement (y = 0.56x + 13.9, R^2 = 0.22) in identifying the same extent of substrate as when assessing slow conduction areas compared to using the IIR 1.2 threshold 6. However, the best relationship is seen with CV and LVS (y = 1.02x+9.7, R^2 = 0.57).

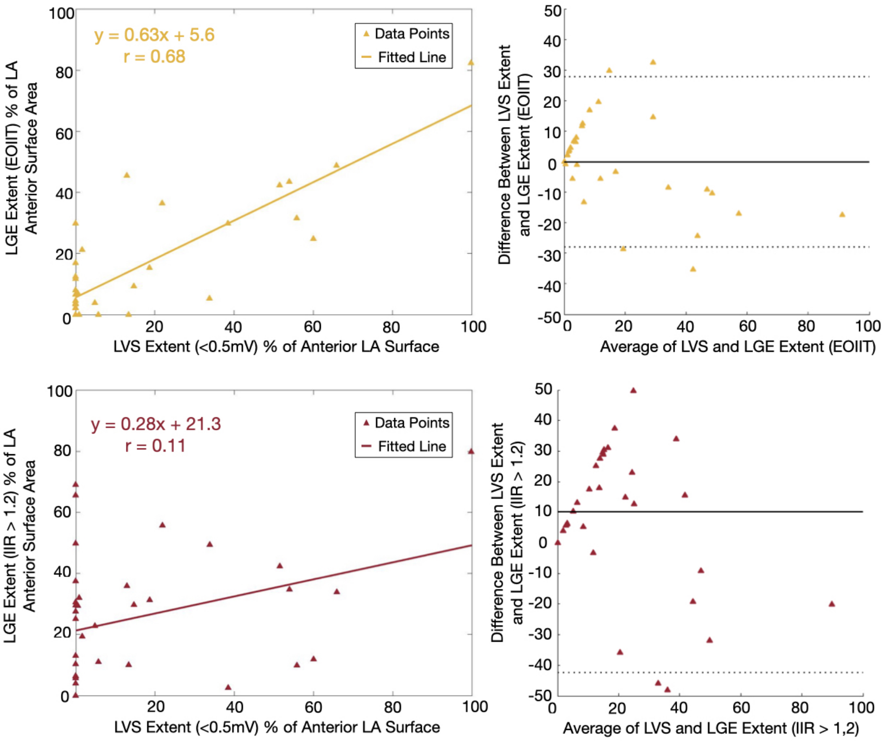

Figure 4: **Percentage of LGE-MRI extent against the percentage of LVS extent and Bland-Altman plot for the anterior wall.** Each triangle represents one patient. On the top row, the LGE-MRI extent obtained using the new thresholds is shown. On the bottom row, the extent is based on IIR >1.2.

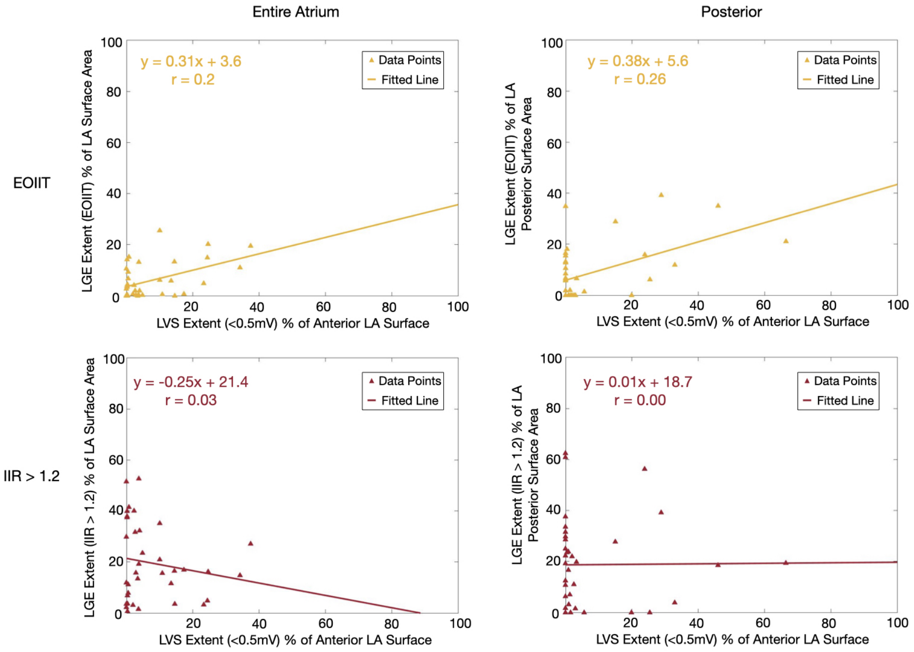

Figure 5: **Percentage of LGE-MRI extent against the percentage of LVS extent for the entire atrium and posterior wall.** Each triangle represents one patient. On the top row, the LGE-MRI extent obtained using the new thresholds is shown. On the bottom row, the extent is based on IIR >1.2.

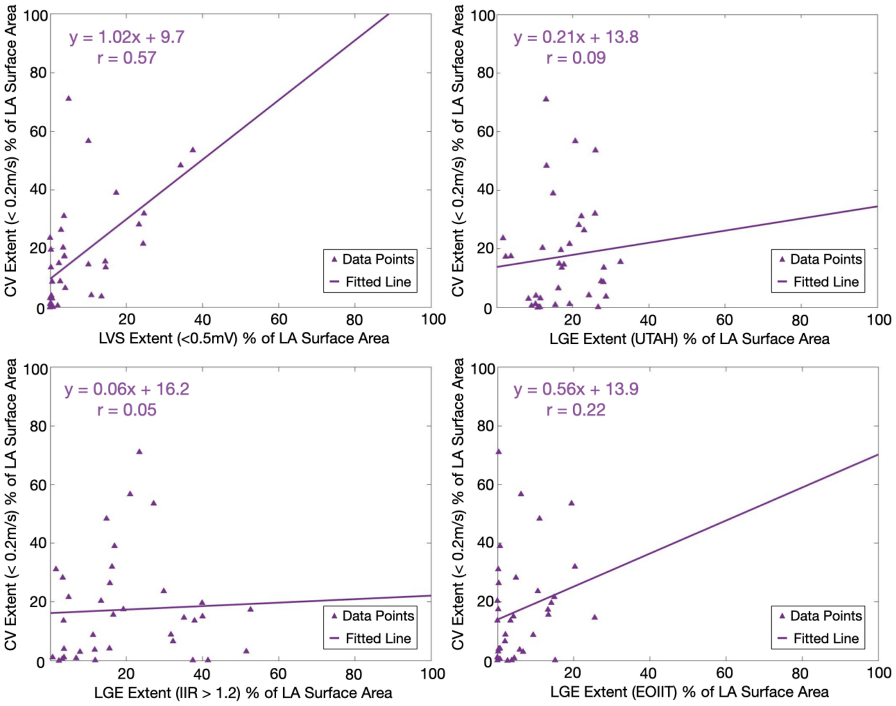

Figure 6: **Percentage of CV <0.2 m/s extent against the percentage of LVS <0.5 mV (top left), LGE-MRI UTAH (top right), LGE-MRI IIR >1.2 (bottom left) and EOIIT (bottom right) extent for the entire atrium.** Each triangle represents one patient.

References

[1] C. Nagel, N. Pilia, L. Unger, et al., Performance of different atrial conduction velocity estimation algorithms improves with knowledge about the depolarization pattern, in: Current Directions in Biomedical Engineering, Vol. 5, De Gruyter, 2019, pp. 101–104. `doi:10.1515/cdbme-2019-0026`.

[2] E. Vigmond, A. Pashaei, S. Amraoui, et al., Percolation as a mechanism to explain atrial fractionated electrograms and reentry in a fibrosis model based on imaging data, Heart Rhythm 13 (7) (2016) 1536–1543. `doi:10.1016/j.hrthm.2016.03.019`.

[3] E. M. Benito, A. Carlosena-Remirez, E. Guasch, et al., Left atrial fibrosis quantification by late gadolinium-enhanced magnetic resonance: a new method to standardize the thresholds for reproducibility., EP Europace 19 (8) (2017) 1272–1279. `doi:10.1093/europace/euw219`.

[4] R. S. Oakes, T. J. Badger, E. G. Kholmovski, et al., Detection and quantification of left atrial structural remodeling with delayed-enhancement magnetic resonance imaging in patients with atrial fibrillation, Circulation 119 (13) (2009) 1758–1767. `doi:10.1161/CIRCULATIONAHA.108.811877`.

[5] N. F. Marrouche, D. Wilber, G. Hindricks, et al., Association of atrial tissue fibrosis identified by delayed enhancement MRI and atrial fibrillation catheter ablation: the DECAAF study, The Journal of the American Medical Association 311 (5) (2014) 498–506. `doi:10.1001/jama.2014.3`.

[6] D. Nairn, C. Nagel, B. Mueller-Edenborn, et al., Spatial and quantitative assessment of the correlation between sinus rhythm and atrial fibrillation voltage mapping to identify low voltage substrate in persistent atrial fibrillation, in: EP Europace, Vol. 23, 2021. `doi:10.1093/europace/euab116.163`.

[7] Y. Chen, G. Medioni, Object modelling by registration of multiple range

images, Image and Vision Computing 10 (3) (1992) 145–155. `doi:10.1016/0262-8856(92)90066-C`.

[8] G. Bouabene, et al., Scalismolab: Scalable image analysis and shape modelling., `https://scalismo.org`.

[9] C. Nagel, S. Schuler, O. Dössel, et al., A bi-atrial statistical shape model for large-scale in silico studies of human atria: model development and application to ECG simulations, Medical Image Analysis 74 (2021) 102210. `doi:10.1016/j.media.2021.102210`.

[10] Blender., `https://www.blender.org`, accessed: 2021-03-01.

References

[1] G. Hindricks, T. Potpara, N. Dagres, et al., "2020 ESC guidelines for the diagnosis and management of atrial fibrillation developed in collaboration with the european association for cardio-thoracic surgery (EACTS)," *European Heart Journal*, vol. 42, pp. 373–498, 2021. doi:10.1093/eurheartj/ehaa612

[2] S. S. Chugh, R. Havmoeller, K. Narayanan, et al., "Worldwide epidemiology of atrial fibrillation: A global burden of disease 2010 study," *Circulation*, 2014. doi:10.1161/CIRCULATIONAHA.113.005119

[3] D. M. Lloyd-Jones, T. J. Wang, E. P. Leip, et al., "Lifetime risk for development of atrial fibrillation: the framingham heart study," *Circulation*, vol. 110, pp. 1042–1046, 2004. doi:10.1161/01.CIR.0000140263.20897.42

[4] M. Velleca, G. Costa, L. Goldstein, et al., "A review of the burden of atrial fibrillation: Understanding the impact of the new millennium epidemic across europe," *EMJ*, 2019.

[5] R. B. Schnabel, X. Yin, P. Gona, et al., "50 year trends in atrial fibrillation prevalence, incidence, risk factors, and mortality in the Framingham Heart Study: A cohort study," *The Lancet*, 2015. doi:10.1016/S0140-6736(14)61774-8

[6] A. S. Go, D. Mozaffarian, V. L. Roger, et al., "Heart disease and stroke statistics–2014 update: a report from the american heart association." *Circulation*, vol. 129, pp. e28–e292, 2014. doi:10.1161/01.cir.0000441139.02102.80

[7] D. G. Wyse, I. C. Van Gelder, P. T. Ellinor, et al., "Lone atrial fibrillation: does it exist?" *Journal of the American College of Cardiology*, vol. 63, pp. 1715–23, 2014. doi:10.1016/j.jacc.2014.01.023

[8] M. Haissaguerre, P. Jaïs, D. C. Shah, and others., "Spontaneous initiation of atrial fibrillation by ectopic beats originating in the pulmonary veins," *New England Journal of Medicine*, vol. 339, pp. 659–666, 1998. doi:10.1056/NEJM199809033391003

[9] P. Taghji, M. El Haddad, T. Phlips, et al., "Evaluation of a strategy aiming to enclose the pulmonary veins with contiguous and optimized radiofrequency lesions in paroxysmal atrial fibrillation: A pilot study." *JACC. Clinical Electrophysiology*, vol. 4, pp. 99–108, 2018. doi:10.1016/j.jacep.2017.06.023

[10] T. Phlips, P. Taghji, M. El Haddad, et al., "Improving procedural and one-year outcome after contact force-guided pulmonary vein isolation: the role of interlesion distance, ablation index, and contact force variability in the 'CLOSE'-protocol." *EP Europace*, vol. 20, pp. f419–f427, 2018. doi:10.1093/europace/eux376

[11] R. R. Tilz, A. Rillig, A.-M. Thum, et al., "Catheter ablation of long-standing persistent atrial fibrillation: 5-year outcomes of the hamburg sequential ablation strategy," *Journal of the American College of Cardiology*, vol. 60, pp. 1921–1929, 2012. doi:10.1016/j.jacc.2012.04.060

[12] A. Verma, C.-y. Jiang, T. R. Betts, et al., “Approaches to catheter ablation for persistent atrial fibrillation.” *The New England Journal of Medicine*, vol. 372, pp. 1812–22, 2015. doi:10.1056/NEJMoa1408288

[13] A. Goette, J. M. Kalman, L. Aguinaga, et al., “EHRA/HRS/APHRS/SOLAECE expert consensus on atrial cardiomyopathies: Definition, characterization, and clinical implication.” *Heart Rhythm*, vol. 14, pp. e3–e40, 2017. doi:10.1016/j.hrthm.2016.05.028

[14] K. Nademanee, J. McKenzie, E. Kosar, et al., “A new approach for catheter ablation of atrial fibrillation: mapping of the electrophysiologic substrate,” *Journal of the American College of Cardiology*, vol. 43, pp. 2044–2053, 2004. doi:10.1016/j.jacc.2003.12.054

[15] M. Hocini, I. Nault, M. Wright, et al., “Disparate evolution of right and left atrial rate during ablation of long-lasting persistent atrial fibrillation.” *Journal of the American College of Cardiology*, vol. 55, pp. 1007–16, 2010. doi:10.1016/j.jacc.2009.09.060

[16] Y.-k. Iwasaki, K. Nishida, T. Kato, et al., “Atrial fibrillation pathophysiology,” *Circulation*, vol. 124, pp. 2264–2274, 2011. doi:10.15252/emmm.201910865

[17] S. Rolf, S. Kircher, A. Arya, et al., “Tailored atrial substrate modification based on low-voltage areas in catheter ablation of atrial fibrillation.” *Circulation. Arrhythmia and Electrophysiology*, vol. 7, pp. 825–33, 2014. doi:10.1161/CIRCEP.113.001251

[18] A. S. Jadidi, H. Lehrmann, C. Keyl, et al., “Ablation of persistent atrial fibrillation targeting low-voltage areas with selective activation characteristics,” *Circulation. Arrhythmia and Electrophysiology*, vol. 9, 2016. doi:10.1161/CIRCEP.115.002962

[19] J. Seitz, C. Bars, G. Théodore, et al., “AF ablation guided by spatiotemporal electrogram dispersion without pulmonary vein isolation: A wholly patient-tailored approach.” *Journal of the American College of Cardiology*, vol. 69, pp. 303–321, 2017. doi:10.1016/j.jacc.2016.10.065

[20] G. Yang, B. Yang, Y. Wei, et al., “Catheter ablation of nonparoxysmal atrial fibrillation using electrophysiologically guided substrate modification during sinus rhythm after pulmonary vein isolation.” *Circulation. Arrhythmia and Electrophysiology*, vol. 9, p. e003382, 2016. doi:10.1161/CIRCEP.115.003382

[21] A. Jadidi, M. Nothstein, J. Chen, et al., “Specific electrogram characteristics identify the extra-pulmonary vein arrhythmogenic sources of persistent atrial fibrillation – characterization of the arrhythmogenic electrogram patterns during atrial fibrillation and sinus rhythm,” *Scientific Reports*, vol. 10, p. 9147, 2020. doi:10.1038/s41598-020-65564-2

[22] A. Schade, L. Costello-Boerrigter, F. Steinborn, et al., “Voltage-guided ablation in persistent atrial fibrillation-favorable 1-year outcome and predictors.” *Journal of Interventional Cardiac Electrophysiology*, 2020. doi:10.1007/s10840-020-00882-z

[23] S. Schuler, M. W. Keller, T. Oesterlein, et al., “Influence of catheter orientation, tissue thickness and conduction velocity on the intracardiac electrogram,” in *Biomedical Engineering/Biomedizinische Technik*, vol. 58, no. s1, 1 2013. doi:10.1515/bmt-2013-4334

[24] E. Anter, C. M. Tschabrunn, and M. E. Josephson, “High-resolution mapping of scar-related atrial arrhythmias using smaller electrodes with closer interelectrode spacing,” *Circulation. Arrhythmia and Electrophysiology*, vol. 8, pp. 537–545, 2015. doi:10.1161/CIRCEP.114.002737

[25] M. Beheshti, K. Magtibay, S. Massé, et al., “Determinants of atrial bipolar voltage: Inter electrode distance and wavefront angle.” *Computers in Biology and Medicine*, vol. 102, pp. 449–457, 2018. doi:10.1016/j.compbiomed.2018.07.011

[26] M. Rodríguez-Mañero, M. Valderrábano, A. Baluja, et al., “Validating left atrial low voltage areas during atrial fibrillation and atrial flutter using multielectrode automated electroanatomic mapping,” *JACC: Clinical Electrophysiology*, vol. 4, pp. 1541–1552, 2018. doi:10.1016/j.jacep.2018.08.015

[27] H. Halperin and A. Kolandaivelu, “MRI-guided electrophysiology intervention,” *Rambam Maimonides Medical Journal*, vol. 1, p. e0015, 2010. doi:10.5041/RMMJ.10015

[28] E. J. Schmidt and H. R. Halperin, “MRI use for atrial tissue characterization in arrhythmias and for EP procedure guidance,” *The International Journal of Cardiovascular Imaging*, vol. 34, pp. 81–95, 2017. doi:10.1007/s10554-017-1179-y

[29] J. Chen, T. Arentz, H. Cochet, et al., “Extent and spatial distribution of left atrial arrhythmogenic sites, late gadolinium enhancement at magnetic resonance imaging, and low-voltage areas in patients with persistent atrial fibrillation: comparison of imaging vs. electrical parameters of fibrosis and arrhythmogenesis,” *EP Europace*, vol. 21, pp. 1484–1493, 2019. doi:10.1093/europace/euz159

[30] S. Kucukseymen, H. Yavin, M. Barkagan, et al., “Discordance in scar detection between electroanatomical mapping and cardiac MRI in an infarct swine model.” *JACC. Clinical Electrophysiology*, vol. 6, pp. 1452–1464, 2020. doi:10.1016/j.jacep.2020.08.033

[31] E. M. Benito, A. Carlosena-Remirez, E. Guasch, et al., “Left atrial fibrosis quantification by late gadolinium-enhanced magnetic resonance: a new method to standardize the thresholds for reproducibility.” *EP Europace*, vol. 19, pp. 1272–1279, 2017. doi:10.1093/europace/euw219

[32] G. Caixal, F. Alarcón, T. F. Althoff, et al., “Accuracy of left atrial fibrosis detection with cardiac magnetic resonance: correlation of late gadolinium enhancement with endocardial voltage and conduction velocity.” *EP Europace*, 2020. doi:10.1093/europace/euaa313

[33] R. Morgan, M. A. Colman, H. Chubb, et al., “Slow conduction in the border zones of patchy fibrosis stabilizes the drivers for atrial fibrillation: Insights from multi-scale human atrial modeling.” *Frontiers in Physiology*, vol. 7, p. 474, 2016. doi:10.3389/fphys.2016.00474

[34] J. G. Betts, P. DeSaix, E. Johnson, et al., *Anatomy and physiology*. OpenStak, 2013. https://books.google.de/books?id=yNp9BwAAQBAJ

[35] S. Y. Ho, J. A. Cabrera, and D. Sanchez-Quintana, “Left atrial anatomy revisited,” *Circulation: Arrhythmia and Electrophysiology*, vol. 5, pp. 220–228, 2012. doi:10.1161/CIRCEP.111.962720

[36] H. Fritsch and W. Kühnel, *Color atlas of human anatomy: Internal organs. volume 2*, Basic sciences. Thieme, 2008. https://books.google.de/books?id=SlubDooAJNoC

[37] J. Kingma, N. van Hemel, and K. Lie, *Atrial fibrillation, a treatable disease?*, Developments in Cardiovascular Medicine. Springer Netherlands, 2012. https://books.google.de/books?id=yNp9BwAAQBAJ

[38] R. J. Hunter, Y. Liu, Y. Lu, et al., “Left atrial wall stress distribution and its relationship to electrophysiologic remodeling in persistent atrial fibrillation,” *Circulation. Arrhythmia and Electrophysiology*, vol. 5, pp. 351–360, 2012. doi:10.1161/CIRCEP.111.965541

[39] C. T. January, L. S. Wann, J. S. Alpert, et al., “2014 AHA/ACC/HRS guideline for the management of patients with atrial fibrillation: A report of the american college of cardiology/american heart association task force on practice guidelines and the heart rhythm society,” *Circulation*, 2014. doi:10.1161/CIR.0000000000000041

[40] J. Pellman and F. Sheikh, “Atrial fibrillation: Mechanisms, therapeutics, and future directions,” *Comprehensive Physiology*, pp. 649–665, 2015. doi:10.1002/cphy.c140047

[41] H. Calkins, G. Hindricks, R. Cappato, et al., “2017 HRS/EHRA/ECAS/APHRS/SOLAECE expert consensus statement on catheter and surgical ablation of atrial fibrillation.” *Heart Rhythm*, vol. 14, pp. e275–e444, 2017. doi:10.1016/j.hrthm.2017.05.012

[42] N. F. Marrouche, D. Wilber, G. Hindricks, et al., “Association of atrial tissue fibrosis identified by delayed enhancement MRI and atrial fibrillation catheter ablation: the DECAAF study,” *The Journal of the American Medical Association*, vol. 311, pp. 498–506, 2014. doi:10.1001/jama.2014.3

[43] B. J. Hansen, J. Zhao, and V. V. Fedorov, “Fibrosis and atrial fibrillation: Computerized and optical mapping,” *JACC: Clinical Electrophysiology*, vol. 3, pp. 531–546, 2017. doi:10.1016/j.jacep.2017.05.002

[44] B. J. Hansen, J. Zhao, T. A. Csepe, et al., “Atrial fibrillation driven by micro-anatomic intramural re-entry revealed by simultaneous sub-epicardial and sub-endocardial optical mapping in explanted human hearts.” *European Heart Journal*, vol. 36, pp. 2390–401, 2015. doi:10.1093/eurheartj/ehv233

[45] J. Sánchez, M. Nothstein, L. Unger, et al., “Influence of fibrotic tissue arrangement on intracardiac electrograms during persistent atrial fibrillation,” *Computing in Cardiology (CinC)*, 2019. doi:10.22489/CinC.2019.342

[46] M. Kraft, A. Büscher, F. Wiedmann, et al., “Current drug treatment strategies for atrial fibrillation and TASK-1 inhibition as an emerging novel therapy option,” *Frontiers in Pharmacology*, vol. 12, 2021. doi:10.3389/fphar.2021.638445

[47] A. Brandes, H. J. G. M. Crijns, M. Rienstra, et al., “Cardioversion of atrial fibrillation and atrial flutter revisited: current evidence and practical guidance for a common procedure,” *EP Europace*, vol. 22, pp. 1149–1161, 2020. doi:10.1093/europace/euaa057

[48] J. Salinet, R. Molero, F. S. Schlindwein, et al., “Electrocardiographic imaging for atrial fibrillation: A perspective from computer models and animal experiments to clinical value,” *Frontiers in Physiology*, vol. 12, 2021. doi:10.3389/fphys.2021.653013

[49] J. Lacalzada-Almeida and J. García-Niebla, “How to detect atrial fibrosis,” *Journal of Geriatric Cardiology*, 2017. doi:10.11909/j.issn.1671-5411.2017.03.008

[50] G. Ndrepepa, *Three-dimensional electroanatomic mapping systems*. Darmstadt: Steinkopff, 2006, pp. 55–76. doi:10.1007/3-7985-1576-X_3

[51] C. Eitel, G. Hindricks, N. Dagres, et al., “Ensite velocity cardiac mapping system: a new platform for 3d mapping of cardiac arrhythmias,” *Expert Review of Medical Devices*, vol. 7, pp. 185–192, 2010. doi:10.1586/erd.10.1

[52] L. M. Ptaszek, F. Chalhoub, F. Perna, et al., “Rapid acquisition of high-resolution electroanatomical maps using a novel multielectrode mapping system,” *Journal of Interventional Cardiac Electrophysiology*, vol. 36, pp. 233–242, 2013. doi:10.1007/s10840-012-9733-y

[53] Y. Kim, S. Chen, S. Ernst, et al., “2019 APHRS expert consensus statement on three-dimensional mapping systems for tachycardia developed in collaboration with HRS, EHRA, and LAHRS,” *Journal of Arrhythmia*, vol. 36, pp. 215–270, 2020. doi:10.1002/joa3.12308

[54] K.-H. Kuck, V. Y. Reddy, B. Schmidt, et al., “A novel radiofrequency ablation catheter using contact force sensing: Toccata study,” *Heart Rhythm*, vol. 9, pp. 18–23, 2012. doi:10.1016/j.hrthm.2011.08.021

[55] J. M. Bakker, “Electrogram recording and analyzing techniques to optimize selection of target sites for ablation of cardiac arrhythmias,” *Pacing and Clinical Electrophysiology*, vol. 42, pp. 1503–1516, 2019. doi:10.1111/pace.13817

[56] U. B. Tedrow and W. G. Stevenson, “Recording and interpreting unipolar electrograms to guide catheter ablation,” *Heart Rhythm*, vol. 8, pp. 791–796, 2011. doi:10.1016/j.hrthm.2010.12.038

[57] C. D. Cantwell, C. H. Roney, F. S. Ng, et al., “Techniques for automated local activation time annotation and conduction velocity estimation in cardiac mapping,” *Computers in Biology and Medicine*, vol. 65, pp. 229–42, 2015. doi:10.1016/j.compbiomed.2015.04.027

[58] Z. F. Issa, J. M. Miller, and D. P. Zipes, “Chapter 4 - electrophysiological testing,” in *Clinical Arrhythmology and Electrophysiology: A Companion to Braunwald’s Heart Disease (Second Edition)*, second edition ed., Z. F. Issa, J. M. Miller, and D. P. Zipes, Eds. Philadelphia: W.B. Saunders, 2012, pp. 62–91. doi:10.1016/B978-1-4557-1274-8.00004-X

[59] A. Berger, “How does it work?: Magnetic resonance imaging,” *BMJ*, vol. 324, pp. 35–35, 2002. doi:10.1136/bmj.324.7328.35

[60] M. Wood, S. Goldberg, M. Lau, et al., “Direct measurement of the lethal isotherm for radiofrequency ablation of myocardial tissue,” *Circulation Arrhythmia and Electrophysiology*, 2011. doi:10.1161/CIRCEP.110.961169

[61] S. Nath, J. P. DiMarco, and D. E. Haines, “Basic aspects of radiofrequency catheter ablation,” *Journal of Cardiovascular Electrophysiology*, vol. 5, pp. 863–876, 1994. doi: 10.1111/j.1540-8167.1994.tb01125.x

[62] A. L. Hodgkin and A. F. Huxley, “A quantitative description of membrane current and its application to conduction and excitation in nerve,” *Journal of Physiology*, vol. 117, pp. 500–544, 1952. doi:10.1113/jphysiol.1952.sp004764

[63] M. Courtemanche, R. J. Ramirez, and S. Nattel, “Ionic mechanisms underlying human atrial action potential properties: insights from a mathematical model,” *American Journal of Physiology-Heart and Circulatory Physiology*, vol. 275, pp. H301–H321, 1998. doi:10.1152/ajpheart.1998.275.1.H301

[64] L. Tung, “A bidomain model for describing ischemic myocardial d-c potentials,” PhD thesis, Massachusetts Institute of Technology, 1978.

[65] Y. Coudière, Y. Bourgault, and M. Rioux, “Optimal monodomain approximations of the bidomain equations used in cardiac electrophysiology,” *Mathematical Models and Methods in Applied Sciences*, vol. 24, pp. 1115–1140, 2014. doi:10.1142/S0218202513500784

[66] M. Wallman, N. P. Smith, and B. Rodriguez, “A comparative study of graph-based, eikonal, and monodomain simulations for the estimation of cardiac activation times,” *IEEE Transactions on Biomedical Engineering*, vol. 59, pp. 1739–1748, 2012. doi:10.1109/TBME.2012.2193398

[67] J. A. Sethian and A. Vladimirsky, “Fast methods for the eikonal and related hamilton- jacobi equations on unstructured meshes,” *Proceedings of the National Academy of Sciences of the United States of America*, vol. 97, pp. 5699–5703, 2000. doi:10.1073/pnas.090060097

[68] P. Álvarez Guirado, “Classification of atrial ectopic beats into spatial segments based on the 12-lead ECG,” Master’s thesis, Karlsruhe Institute of Technology (KIT), 2018.

[69] I. T. Jolliffe and J. Cadima, “Principal component analysis: a review and recent developments,” *Philosophical Transactions of the Royal Society A: Mathematical*, vol. 374, p. 20150202, 2016. doi:10.1098/rsta.2015.0202

[70] C. Schilling, M. P. Nguyen, A. Luik, et al., “Non-linear energy operator for the analysis of intracardial electrograms,” in *IFMBE Proceedings World Congress on Medical Physics and Biomedical Engineering*, vol. 25/4, 1 2009, pp. 872–875. doi:10.1007/978-3-642-03882-2_233

[71] C. Nagel, “Robust conduction velocity estimation for a clinical setting,” Master’s thesis, Karlsruhe Institute of Technology (KIT), Karlsruhe, 2019.

[72] M. Lüthi, T. Gerig, C. Jud, et al., “Gaussian process morphable models.” *IEEE Transactions on Pattern Analysis and Machine Intelligence*, vol. 40, pp. 1860–1873, 2018. doi:10.1109/TPAMI.2017.2739743

[73] P. Singh, N. Singh, K. K. Singh, et al., “Chapter 5 - diagnosing of disease using machine learning,” in *Machine Learning and the Internet of Medical Things in Healthcare*, K. K. Singh, M. Elhoseny, A. Singh, and A. A. Elngar, Eds. Academic Press, 2021, pp. 89–111. doi:https://doi.org/10.1016/B978-0-12-821229-5.00003-3

[74] L. M. Sullivan, J. Weinberg, and J. F. Keaney, “Common statistical pitfalls in basic science research,” *Journal of the American Heart Association*, vol. 5, 2016. doi:10.1161/JAHA.116.004142

[75] A. P. King and R. J. Eckersley, “Chapter 5 - inferential statistics ii: Parametric hypothesis testing,” in *Statistics for Biomedical Engineers and Scientists*, A. P. King and R. J. Eckersley, Eds. Academic Press, 2019, pp. 91–117. doi:10.1016/B978-0-08-102939-8.00014-1

[76] S. Boslaugh and P. A. Watters, *Statistics in a nutshell - a desktop quick reference*. O’Reilly Media, Inc, 2008.

[77] S. Gaeta, T. D. Bahnson, and C. Henriquez, “Mechanism and magnitude of bipolar electrogram directional sensitivity: characterizing underlying determinants of bipolar amplitude,” *Heart Rhythm*, 2019. doi:10.1016/j.hrthm.2019.12.010

[78] C.-Y. Lin, A. L. D. Te, Y.-J. Lin, et al., “High-resolution mapping of pulmonary vein potentials improved the successful pulmonary vein isolation using small electrodes and inter-electrode spacing catheter.” *International Journal of Cardiology*, vol. 272, pp. 90–96, 2018. doi:10.1016/j.ijcard.2018.06.062

[79] D. Frisch, T. G. Oesterlein, L. A. Unger, et al., “Mapping and removing the ventricular far field component in unipolar atrial electrograms.” *IEEE Transactions on Biomedical Engineering*, vol. 67, pp. 2905–2915, 2020. doi:10.1109/TBME.2020.2973471

[80] D. Nairn, H. Lehrmann, B. Müller-Edenborn, et al., “Comparison of Unipolar and Bipolar Voltage Mapping for Localization of Left Atrial Arrhythmogenic Substrate in Patients With Atrial Fibrillation,” *Frontiers in Physiology*, vol. 11, 2020. doi:10.3389/fphys.2020.575846

[81] D. Nairn, D. Hunyar, J. Sánchez, et al., “Impact of electrode size on electrogram voltage in healthy and diseased tissue,” *Computing in Cardiology (CinC)*, vol. 47, 2020. doi:10.22489/CinC.2020.146

[82] M. Yu, “Study of the intra-cardiac electrogram signals using in-silico experiments to asses the impact of the atrial geometry,” Master’s thesis, 2022.

[83] C. H. Roney, A. Pashaei, M. Meo, et al., “Universal atrial coordinates applied to visualisation, registration and construction of patient specific meshes.” *Medical Image Analysis*, vol. 55, pp. 65–75, 2019. doi:10.1016/j.media.2019.04.004

[84] G. Plank, A. Loewe, A. Neic, et al., “The openCARP simulation environment for cardiac electrophysiology.” *Computer methods and Programs in Biomedicine*, vol. 208, p. 106223, 2021. doi:10.1016/j.cmpb.2021.106223

[85] J. Sánchez, M. Nothstein, A. Neic, et al., “openCARP: An open sustainable framework for in-silico cardiac electrophysiology research,” Computing in Cardiology, vol. 47, 1 2020. doi:10.22489/CinC.2020.111

[86] L. Clerc, “Directional differences of impulse spread in trabecular muscle from mammalian heart.” *The Journal of Physiology*, vol. 255, pp. 335–346, 1976. doi:10.1113/jphysiol.1976.sp011283

[87] S. Zahid, H. Cochet, P. M. Boyle, et al., “Patient-derived models link re-entrant driver localization in atrial fibrillation to fibrosis spatial pattern.” *Cardiovascular Research*, vol. 110, pp. 443–54, 2016. doi:10.1093/cvr/cvw073

[88] A. Yagishita, S. DE Oliveira, I. Cakulev, et al., “Correlation of left atrial voltage distribution between sinus rhythm and atrial fibrillation: Identifying structural remodeling by 3-d electroanatomic mapping irrespective of the rhythm,” *Journal of Cardiovascular Electrophysiology*, 2016. doi:10.1111/jce.13002

[89] D. Nairn, M. Eichenlaub, H. Lehrmann, et al., “Spatial correlation of left atrial low voltage substrate in sinus rhythm versus atrial fibrillation: Identifying the pathological substrate irrespective of the rhythm,” *medRxiv preprint*, 2022. doi:10.1101/2022.02.18.22271172

[90] T. Shen, “Comparison of intra-cardiac mapping modalities by analysing the amplitude of electrogram signals,” Master’s thesis, Karlsruhe Institute of Technology (KIT), 2021.

[91] M. P. Nguyen, C. Schilling, and O. Dössel, “A new approach for automated location of active segments in intracardiac electrograms,” in *IFMBE Proceedings World Congress on Medical Physics and Biomedical Engineering*, vol. 25/4, 1 2009, pp. 763–766.

[92] J. S. Richman, D. E. Lake, and J. Moorman, *Sample entropy*, Methods in Enzymology, vol. 384. Academic Press, 2004. doi:10.1016/S0076-6879(04)84011-4

[93] V. Jacquemet, N. Virag, Z. Ihara, et al., “Study of unipolar electrogram morphology in a computer model of atrial fibrillation,” *Journal of Cardiovascular Electrophysiology*, vol. 14, pp. S172–S179, 2003. doi:10.1046/j.1540.8167.90308.x

[94] L. Schicketanz, L. A. Unger, J. Sánchez, et al., “Separating atrial near fields and atrial far fields in simulated intra-atrial electrograms,” in *Current Directions in Biomedical Engineering*, vol. 7, no. 2, 1 2021, pp. 175–178. doi:10.1515/cdbme-2021-2045

[95] R. S. Oakes, T. J. Badger, E. G. Kholmovski, et al., “Detection and quantification of left atrial structural remodeling with delayed-enhancement magnetic resonance imaging in patients with atrial fibrillation,” *Circulation*, 2009. doi:10.1161/CIRCULATIONAHA.108.811877

[96] J. Whitaker, R. Rajani, H. Chubb, and others., “The role of myocardial wall thickness in atrial arrhythmogenesis,” *EP Europace*, vol. 18, pp. 1758–1772, 2016. doi:10.1093/europace/euw014

[97] R. Beinart, S. Abbara, A. Blum, et al., “Left atrial wall thickness variability measured by CT scans in patients undergoing pulmonary vein isolation,” *Journal of Cardiovascular Electrophysiology*, vol. 22, pp. 1232–1236, 2011. doi:10.1111/j.1540-8167.2011.02100.x

[98] K. Higuchi, J. Cates, G. Gardner, et al., “The Spatial Distribution of Late Gadolinium Enhancement of Left Atrial Magnetic Resonance Imaging in Patients With Atrial Fibrillation,” *JACC: Clinical Electrophysiology*, vol. 4, pp. 49–58, 2018. doi:10.1016/J.JACEP.2017.07.016

[99] B. Müller-Edenborn, J. Chen, J. Allgeier, et al., “Amplified sinus-P-wave reveals localization and extent of left atrial low-voltage substrate: implications for arrhythmia freedom following pulmonary vein isolation.” *EP Europace*, 2019. doi:10.1093/europace/euz297

[100] D. Nairn, M. Eichenlaub, B. Müller-Edenborn, et al., “LGE-MRI for diagnosis of left atrial cardiomyopathy as identified in high-definition endocardial voltage and conduction velocity mapping,” *medRxiv preprint*, 2022. doi:10.1101/2022.02.02.22269817

List of Publications and Supervised Theses

Journal Articles

- **D. Nairn**, H. Lehrmann, B. Müller-Edenborn, S. Schuler, T. Arentz, O. Dössel, A. Jadidi, A. Loewe *Comparison of Unipolar and Bipolar Voltage Mapping for Localization of Left Atrial Arrhythmogenic Substrate in Patients With Atrial Fibrillation*, Frontiers in Physiology, 2020, 11:575846, doi: 10.3389/fphys.2020.575846
- **D. Nairn**, M. Eichenlaub, B. Müller-Edenborn, H. Lehrmann, C. Nagel, L. Azzolin, G. Luongo, R. Figueras Ventura, B. Rubio Forcada, A. Vallès Colomer, T. Arentz, O. Dössel, A. Loewe, A. Jadidi *LGE-MRI for diagnosis of left atrial cardiomyopathy as identified in high-definition endocardial voltage and conduction velocity mapping*, under review, 2022, medRxiv preprint, doi: 10.1101/2022.02.02.22269817
- **D. Nairn**, M. Eichenlaub, H. Lehrmann, B. Müller-Edenborn, J. Chen, T. Huang, C. Nagel, J. Sänchez, G. Luongo, T. Arentz, O. Dössel, A. Jadidi, A. Loewe *Spatial Correlation of Left Atrial Low Voltage Substrate in Sinus Rhythm versus Atrial Fibrillation: Identifying the Pathological Substrate Irrespective of the Rhythm*, under review, 2022, medRxiv preprint, doi: 10.1101/2022.02.18.22271172
- M. Eichenlaub, B. Mueller-Edenborn, H. Lehrmann, J. Minners, **D. Nairn**, A. Loewe, J. Allgeier, N. Jander, M. Allgeier, P. Ruile, M. Hein, F. Rees, D. Trenk, R. Weber, F.-J. Neumann, T. Arentz, and A. Jadidi. *Non-invasive body surface electrocardiographic imaging for diagnosis of atrial cardiomyopathy*, In EP Europace, 2021, 23:2010-2019, doi: 10.1093/europace/euab140
- G. Luongo, G. Vacanti, V. Nitzke, **D. Nairn**, C. Nagel, D. Kabiri, T.P. Almeida, D.C. Soriano, M.W. Rivolta, G.A. Ng, O. Dössel, L. Armin, R. Sassi, and A. Loewe *Hybrid Machine Learning to Localize Atrial Flutter Substrates Using the Surface 12-lead ECG*, Europace, 2021, doi: 10.1093/europace/euab322
- G. Luongo, F. Rees, **D. Nairn**, M.W. Rivolta, O. Dössel, R. Sassi, C. Ahlgrim, L. Mayer, F.J. Neumann, T. Arentz, A. Jadidi, A. Loewe, and B. Müller-Edenborn *Machine Learning Using a Single-lead ECG to Identify Patients with Atrial Fibrillation-Induced Heart Failure*, Frontiers in Cardiovascular Medicine, 2022

- A. Loewe, Y. Lutz, **D. Nairn**, A. Fabbri, N. Nagy, N. Toth, X. Ye, D. H. Fuertinger, S. Genovesi, P. Kotanko, J. G. Raimann, S. Severi, *Hypocalcemia-Induced Slowing of Human Sinus Node Pacemaking*, Biophysical Journal, 2019, 117(12):2244-2254, doi: 10.1016/j.bpj.2019.07.037.
- L. Azzolin, M. Eichenlaub, C. Nagel, **D. Nairn**, J. Sánchez, L. Unger, O. Dössel, A. Jadidi, and A. Loewe *Personalized ablation vs. conventional ablation strategies to terminate atrial fibrillation and prevent recurrence: a systematic in silico study*, under review, 2021
- L. Azzolin, M. Eichenlaub, C. Nagel, **D. Nairn**, J. Sánchez, L. Unger, O. Dössel, A. Jadidi, and A. Loewe *AugmentA: Patient-specific Augmented Atrial model Generation Tool*, under review, 2021, medRxiv preprint, doi: 10.1101/2022.02.13.22270835

Refereed Conference Articles

- **D. Nairn**, H. Lehrmann, A. Jadidi, O. Dössel, A. Loewe, *Comparison of Voltage Map Calculation Methods using Non-Fractionated EGM Signals in a Persistent AF Patient*, Computing in Cardiology (CinC), 2019
- **D. Nairn**, D. Hunyar, J. Sánchez, O. Dössel, A. Loewe *Impact of Electrode Size on Electrogram Voltage in Healthy and Diseased Tissue*, Computing in Cardiology Conference (CinC), 2020
- **D. Nairn**, C. Nagel, B. Müller-Edenborn, H. Lehrmann, T. Arentz, O. Dössel, A. Jadidi, A. Loewe *Optimal Regional Voltage Thresholds for Identifying Ablation Targets in Patients with Atrial Fibrillation*, Computing in Cardiology Conference (CinC), 2021
- L. Azzolin, C. Nagel, **D. Nairn**, J. Sanchez, T. Zheng, M. Eichenlaub, A. Jadidi, O. Doessel, and A. Loewe. *Automated Framework for the Augmentation of Missing Anatomical Structures and Generation of Personalized Atrial Models from Clinical Data.* Computing in Cardiology Conference (CinC), 2021

Refereed Conference Abstracts

- **D. Nairn**, C. Nagel, B. Müller-Edenborn, H. Lehrmann, A. Jadidi, A. Loewe *Spatial and quantitative assessment of the correlation between sinus rhythm and atrial fibrillation voltage mapping to identify low voltage substrate in persistent atrial fibrillation*, EHRA, 2021
- **D. Nairn**, D. Hunyar, J. Sánchez, O. Dössel, A. Loewe *Inverse Relationship Between Electrode Size and Voltage During Intracardiac Mapping*, BMT 2020 (2020)
- **D. Nairn**, X. Ye, D. H. Fuertinger, P. Kotanko, A. Loewe, J. G. Raimann, *Low Serum Calcium is Correlated with Lower Heart Rate in Elderly Dialysis Patients*, Nephrology Dialysis Transplantation, 2019

- **D. Nairn**, X. Ye, D. H. Fuertinger, P. Kotanko, A. Loewe, J. G. Raimann, *Hypocalcemia-Induced Bradycardia Is More Pronounced in Male Hemodialysis Patients*, J Am Soc Nephrol, 2019
- Axel Loewe, Yannick Lutz, **Deborah Nairn**, Alan Fabbri, Norbert Nagy, Noemi Toth, Xiaoling Ye, Doris H. Fuertinger, Simonetta Genovesi, Peter Kotanko, Jochen G. Raimann, Stefano Severi, *Can Hypocalcaemia Cause Severe Sinus Bradycardia and Asystole in Dialysis Patients?*, Clin Res Cardiol, 2020

Invited Talks

Deborah Nairn, *Low Voltage Revisited*, Atrial Signals, 2021

Reports and Theses

Supervised Student Theses

- Daniel Hunyar, *Identification of how voltage is affected due to changes in electrode size and the use of a Lasso catheter using a computational model*, Bachelor Thesis, Institute of Biomedical Engineering, Karlsruhe Institute of Technology (KIT), 2020
- Ting Shen, *Comparison of intracardiac mapping modalities by analysing electrogram signals*, Master Thesis, Institute of Biomedical Engineering, Karlsruhe Institute of Technology (KIT), 2021
- Miao Yu, *Study of the intra-cardiac electrogram signals using in-silico experiments to asses the impact of the atrial geometry*, Master Thesis, Institute of Biomedical Engineering, Karlsruhe Institute of Technology (KIT), 2021
- Johannes Deininger, *Investigating the high correlation between unipolar and bipolar voltage maps*, Student Project, Institute of Biomedical Engineering, Karlsruhe Institute of Technology (KIT), 2021

Awards & Grants

Joint WG e-Cardiology European Society of Cardiology (ESC) CinC Clinical Needs Translational Award (CTA) *Optimal Regional Voltage Thresholds for Identifying Ablation Targets in Patients with Atrial Fibrillation*, Computing in Cardiology, 2021

Patent Application

L.Azzolin, A. Loewe, O. Dössel, **D. Nairn**, C. Nagel, J. Sánchez, L. Unger and T. Zheng, *Automated pipeline to generate augmented anatomical and functional atrial digital twins*, 2021